A UNIFIED APPROACH TO UXO DISCRIMINATION USING THE METHOD OF AUXILIARY SOURCES

UX1446 - FINAL REPORT

Lead Principal Investigator: Leonard R. Pasion

Co-performers: Lin-Ping Song, Nicolas Lhomme, Fridon Shubitidze, and Douglas W. Oldenburg

Sky Research Inc.
University of British Columbia - Geophysical Inversion Facility

October 12, 2006

Distribution Statement A: Approved for Public Release, Distribution is Unlimited

This report was prepared under contract to the Department of Defense Strategic Environmental Research and Development Program (SERDP). The publication of this report does not indicate endorsement by the Department of Defense, nor should the contents be construed as reflecting the official policy or position of the Department of Defense. Reference herein to any specific commercial product, process, or service by trade name, trademark, manufacturer, or otherwise, does not necessarily constitute or imply its endorsement, recommendation, or favoring by the Department of Defense.

Executive Summary

The research described in this report was conducted in support of Strategic Environmental Research and Development Program (SERDP) SEED Broad Agency Announcement (BAA), Statement of Need UXSEED-05-02, "Innovative Approaches to Unexploded Ordnance (UXO) Cleanup." A SERDP SEED research and development project UX-1446 entitled "A Unified Approach to UXO Discrimination Using the Method of Auxiliary Sources" was proposed in response to the above BAA.

The main emphasis of this research was to explore the fundamental characteristics of the Surface Magnetic Charge (SMC) and Standard Excitation Approach (SEA) methods when applied to UXO discrimination problems. Both methods were derived from the Method of Auxiliary Sources (MAS), and thus represent the secondary magnetic fields from a compact metallic target with a surface of magnetic charge. The SEA and SMC are relatively new modeling techniques for UXO discrimination. Therefore, we investigated some fundamental, as well as practical, characteristics of the forward model. These include the accuracy with which the methods can model sensor data, the speed to carry out the forward modeling, and the type of discrimination algorithms amenable to each of the forward modeling methods. For the SEA, we wanted to determine the ease with which the sources can be derived for a particular target. For the SMC, we wanted to determine if the surface magnetic charge distribution is a good discriminant, and, if so, what algorithm is required to obtain a stable estimate of the magnetic charge.

Several data sets were analyzed as part of this investigation. Geonics EM63 data were collected on the Engineer Research and Development Center (ERDC) test stand in Vicksburg, MS by Sky Research Inc., University of British Columbia personnel, and Cliff Morgan and Morgan Field of the U.S. Army Corps of Engineers (USACE)-ERDC from March 16-April 11, 2006. Geophex GEM3 data were collected on the ERDC test stand in Vicksburg MS by Sky Research Inc., and Cliff Morgan and Morgan Field of the USACE-ERDC from February 2-10, 2006. Geophex GEM3 data and Geonics EM63 data collected during the month of July, 2005 on the Sky Research Inc. UXO testplot in Ashland, OR were also processed for this project. In this report, we do not estimate location and orientation from the data. Instead, we assume that the location and orientation estimates can be provided by alternative means.

Contents

1 Introduction **3**

2 Investigation of EMI Sensing for Metallic Objects: a Unified and Versatile Standardized Excitation Approach in Frequency- and Time- domain **6**

2.1 Abstract . . . 6
2.2 Introduction . . . 6
2.3 The Standardized Excitation Approach Method . . . 7
2.3.1 Decomposing a Primary Field . . . 7
2.3.2 Synthesizing the Secondary Fields . . . 9
2.3.3 Solving for the Modal Response Coefficients: Reduced Set of Sources . . . 10
2.4 Determination of Effective Spheroidal Modes . . . 10
2.4.1 Uniform Primary Field . . . 11
2.4.2 Non-uniform Primary Field . . . 13
2.5 An Example of SEA Modeling . . . 14
2.5.1 Frequency-domain Response . . . 14
2.5.2 Transient EM Responses . . . 15
2.6 Development of a Reduced Source Library . . . 15
2.7 UXO Identification Tests . . . 22
2.7.1 A simple discrimination example using a single sounding . . . 22
2.7.2 A discrimination example using GEM3 data collected on the ERDC Test Stand . . . 27
2.8 Inversion for Optimal Orientation and Location of an Object . . . 32
2.9 Conclusions . . . 32

3 Regularization of the Surface Charge Model for the Inversion of Electromagnetic Data **36**

3.1 Abstract . . . 36
3.2 Introduction . . . 36
3.3 Model description and implementation . . . 37
3.3.1 The Surface Magnetic Charge Model . . . 37
3.3.2 Numerical Implementation of the SMC Model . . . 38
3.3.3 Discretization of the charge surface . . . 39
3.4 Inverting for a Surface Charge Distribution . . . 39
3.5 Properties of the Normalized Surface Magnetic Charge . . . 42
3.5.1 Field on a surface with charges . . . 42
3.5.2 The normalized surface magnetic charge on a spherical surface for a dipole field . . . 43
3.5.3 Investigating the normalized magnetic charge using the Method of Moments . . . 45
3.5.4 Comparison to SEA modeled secondary fields . . . 58
3.5.5 Conclusion . . . 62
3.6 Regularized Inversion for a Surface Charge Distribution . . . 64
3.6.1 Formulation of the regularized inverse problem . . . 64
3.6.2 Total magnetic charge and regularization . . . 66
3.6.3 Regularizing for a stable total magnetic charge . . . 68
3.6.4 Stability of the regularization method . . . 71

3.6.5 Detailed analysis of four standard ordnance . . . 74
3.7 Application of the regularized NSMC . . . 77
3.7.1 Time domain analysis of standard items . . . 77
3.7.2 Frequency domain analysis of standard items . . . 77
3.7.3 Application to field data . . . 79
3.8 Conclusion . . . 84

4 Discussion and Conclusions **86**
4.1 Objectives . . . 86
4.2 The Standardized Excitation Approach . . . 86
4.3 The Surface Magnetic Charge Model . . . 87
4.4 Outlook . . . 88

List of Figures

1.1 Results from inverting Geonics EM63 data collected over an 105 mm projectile. 4
1.2 Modeling magnetostatic data with the Method of Auxiliary Sources method. A spheroid is modelled using the Earth's magnetic field at Yuma, Arizona. The analytical solution for a spheroid is used. The Method of Auxiliary Sources solution was obtained by assuming a frequency of 10^{-6} Hz. 5

2.1 The prolate spheroidal coordinate system (η, ξ, ϕ) with major and minor semi-axes of a and b, the interfocal distance of $d = 2\sqrt{a^2 - b^2}$, and $\xi = \xi_0 = 2a/d$. 8
2.2 MAS/TSA-based SEA. Reduced set of sources q_i^{pmn} distributed along rings on the spheroid surface and the auxiliary sources Q_k^{pmn} distributed on an internal auxiliary surface of a cylinder-like object. Both induced sources are the response to fundamental excitation fields ψ_{pmn}^{pr} and produce the same scattered field ψ_{pmn}^{sc} outside of the object. 9
2.3 Sensing of a BOR-like object. 11
2.4 Spheroidal expansion of a uniform field $\mathbf{H} = \hat{z}$ on the spheroid with semi-major and minor axes $a = 11$ cm and $b = 5$ cm. The orientation of the spheroid is $\theta = 0^0$ for (a) and (b); $\theta = 45^0$ (c) and (d); $\theta = 90^0$ (e) and (f). 12
2.5 Spheroidal expansion of a non-uniform field from GEM-3 transmitter on the spheroid with semi-major and minor axes $a = 11$ cm and $b = 5$ cm. The vertical distance between the transmitter and the center of the spheroid is 29.2 cm. The orientation of the spheroid is (a) $\theta = 0^0$, (b) $\theta = 45^0$, and (c) $\theta = 90^0$. 13
2.6 Spheroidal expansion of a non-uniform field from GEM-3 transmitter on the spheroid with semi-major and minor axes $a = 11$ cm and $b = 5$ cm. The vertical distance between the transmitter and the center of the spheroid is 17 cm. The orientation of the spheroid is (a) $\theta = 0^0$, (b) $\theta = 45^0$, and (c) $\theta = 90^0$. 14
2.7 Frequency-domain response from GEM-3. h is the distance between the center of the cylinder ($L = 30.48$ cm, $d = 7.5$ cm) and the center of the GEM-3 receiver. 15
2.8 Transient response for the same solid steel cylinder in Fig. 2.7. For each measurement the cylinder is 60 cm from the measurement loop. 16
2.9 Items for which RSS were computed. 17
2.10 Apparatus for acquiring data for determining the RSS. 18
2.11 The distribution of RSS for C3 along a spheroidal coordinate η. 19
2.12 The distribution of RSS for C5 along a spheroidal coordinate η. 19
2.13 Modeled and measured GEM3 response for a horizontal ATC 40 mm (C3). 20
2.14 Modeled and measured GEM3 response for a horizontally ATC 81mm (C8). 21
2.15 Misfit values for a trial identification test. 23
2.16 Pattern matching tests. (a)-(i): C1-C9. UXO C4 identified 24
2.17 Misfit values for another trial identification test. 25
2.18 Pattern matching tests. UXO C8 identified 26
2.19 Examples of finding the optimal location by translating a template generated by the RSS. 28
2.20 Modeled and measured GEM3 response for a vertically oriented ATC 40 mm (C3). 29
2.21 Template example for C3. 30
2.22 Modeled and measured GEM3 response for a horizontally oriented ATC 81 mm (C8). 31
2.23 Template example for C8. 32

2.24 Inversion test I. Recovered model parameters versus iteration number. 33
2.25 Inversion test II. Recovered model parameters versus iteration number. 34

3.1 Representation of the response of a target using (a) a dipole and (b) a surface magnetic charge. . . 37
3.2 An example of discretizing a spheroid. 39
3.3 Discretization of a sphere derived from an icosahedron 40
3.4 40 mm projectile (45 degrees inclination, 60 cm below sensor). Both solutions of charge distribution produce large oscillations. 41
3.5 Geometries for determining the field on a charge surface. 42
3.6 Sphere surface. 43
3.7 Geometry of example. We match boundary conditions on a surface and compare the data predicted by the charge distribution on the surface with the data predicted by a dipole model. 48
3.8 Method of Moments solution for the surface magnetic charge distributions on a sphere with a vertical primary field excitation. The surface was discretized with 900 patches. 50
3.9 Method of Moments solution for the surface magnetic charge distributions on a sphere with a horizontal primary field excitation. The surface was discretized with 900 patches. 51
3.10 Method of Moments solution for the surface magnetic charge distributions on a sphere with a vertical primary field excitation. The surface was discretized with 400 patches. 52
3.11 Method of Moments solution for the surface magnetic charge distributions on a sphere with a primary field excitation at a 45 degree angle ($\mathbf{H}^P = (\hat{\mathbf{y}} + \hat{\mathbf{z}})/\sqrt{2}$). The surface was discretized with 400 patches. 53
3.12 Method of Moments solution for the surface magnetic charge distributions on a sphere with a horizontal primary field excitation. The surface was discretized with 400 patches. 54
3.13 Method of Moments solution for the surface magnetic charge distributions on a spheroid with a vertical primary field excitation. 55
3.14 Method of Moments solution for the surface magnetic charge distributions on a spheroid with a primary field at a 45 degree angle ($\mathbf{H}^P = (\hat{\mathbf{y}} + \hat{\mathbf{z}})/\sqrt{2}$).. 56
3.15 Method of Moments solution for the surface magnetic charge distributions on a spheroid with a horizontal primary field excitation. 57
3.16 Distribution of the normal component of the scattered and primary fields and their ratio at the surface of a spheroid enclosing a vertical cylinder. Reference case. 59
3.17 Distribution of the normal component of the scattered and primary fields and their ratio at the surface of a spheroid enclosing a horizontal cylinder. 59
3.18 Distribution of the normal component of the scattered and primary fields and their ratio at the surface of a spheroid enclosing a cylinder at 45°. 60
3.19 Distribution of the normal component of the scattered and primary fields and their ratio at the surface of a spheroid enclosing a vertical cylinder located 30 cm off the center of the transmitter. . 60
3.20 Distribution of the normal component of the scattered and primary fields and their ratio at the surface of a spheroid enclosing a horizontal cylinder located 30 cm off the center of the transmitter. 61
3.21 Distribution of the normal component of the scattered and primary fields and their ratio at the surface of a spheroid enclosing an oblique cylinder located 30 cm off the center of the transmitter. 61
3.22 Distribution of the normal component of the scattered and primary fields and their ratio at the surface of a spheroid enclosing a vertical cylinder using lower resolution. 62
3.23 Distribution of the normal component of the scattered and primary fields and their ratio at the surface of a large elongated spheroid enclosing a vertical cylinder. 63
3.24 Distribution of the normal component of the scattered and primary fields and their ratio at the surface of a sphere enclosing a vertical cylinder. 63
3.25 Regularized ring solution for 40 mm projectile (45 degrees, 60 cm below sensor). In top central panel, crosses show the 10-ring solution, the solid red line the 40-ring solution using the exact same automated regularization procedure (described in section 3.6.3). Misfit, expectancy, correlation and total magnetic charge exactly coincide for 10-40 rings. 66

3.26 Charge distribution on 40 rings along modeling spheroid for same 40 mm item (Latitude +90 for the pole closest to the surface, 0 equator, -90 bottom). Top panel: all regularized models, least regularized with largest amplitude, λ in log scale from $10^{-}10$ to 10^{5}. Lower panel: sampled models for lambda = 4, 24, 123, 641, 3350, 17500 and above. The thick dashed line corresponds to the regularization applied for Figure 3.25. 67
3.27 Example of L-curves (i.e. Φ_{d} vs. Φ_{m} curves) for a 40 mm projectile. Left panel: object at 45 degrees, 60 cm below sensor. Stars indicate maximum curvature, large dots alternative pick for regularization. Right panel: black, red and green curves correspond to shallow depth (20-25 cm), the remaining ones to deeper position (60 cm); black solid line and blue line-dot at 45 degrees, red dashed and cyan dash-dot vertical, green crosses and magenta plus markers horizontal. 67
3.28 Total magnetic charge vs. regularization parameter, same legend and setting as previous figure. Left panel shows large variations of total magnetic charge Q_{smc} during the regularization. The dashed horizontal line shows $Q_{\mathrm{smc}}(\mathbf{m}_o)$ (also called Q_{uni}). Right panel shows Q_{smc} and Q_{uni} for different orientations and depths. Q_{uni} is similar for all cases. 68
3.29 Regularization of field data over a 40 mm UXO. L-curve, Observation and model for different levels of regularization. Corner of L-curve indicated with a star, our chosen regularization with a red dot. 70
3.30 Variation of Total magnetic charge Q_{smc} during regularized inversion of first time channel for 60 mm, 90 mm and M42 projectiles. For all panels, each curve shows Q_{smc} for a different position/orientation of target relative to test stand. Horizontal dashed lines show Q_{uni} for each case and define the region of stability of the total charge. Large dots indicate Q_{smc} for the proposed regularization choice whereas stars highlight failure to obtain stable charge with corner of L-curve. Positions/orientations are given in Table 3.5. Black, red and green curves correspond to shallow depths, blue, magenta and cyan to deeper positions; black solid line and blue line-dot at 45 degrees, red dashed and cyan dash-dot vertical, green crosses and magenta pluses horizontal, as in Figure 3.27. 73
3.31 Total magnetic charge Q_{smc} during regularization for 40 mm, 60 mm, 90 mm and M42. Each panel shows all six positions given in Table 3 using the 12th time channel with the same plotting conventions as previous figure. 73
3.32 Total magnetic charge as a function of time for 40 mm, 60 mm, 90 mm and M42 projectiles, using EM-63 data from test stand at positions summarized in Table 3. Time series are shorter for smaller objects because SNR is too low at later time channels. 74
3.33 Correlation coefficient between observed data and model prediction for all time channels, 2 depths and 3 inclinations (0 for horizontal). 75
3.34 Percentage of solutions for which $|\Phi_{\mathrm{d}}(regu)/\Phi_{\mathrm{d}}(corner) - 1|$ smaller than misfit ratio ($D\Phi$) as a function of time channel. The lowest row shows that in 55$\%$ of cases the misfit ratio is below 5$\%$, which means that the misfit for the chosen parameter is within 5% of that of the corner of the L-curve (assumed best guess for noise estimation). The next lines show that 73$\%$ of cases are below 10$\%$ misfit ratio, 97$\%$ below 25$\%$, 99.5$\%$ below 50$\%$ and 100$\%$ below 100$\%$. 76
3.35 Square root of signal to noise ratio. For each item, the first three columns correspond to shallow positions, the next three to deeper positions, where SNR is lower. SNR=0 at later time channels if too few data for inversion (22$\%$ of cases), SNR$\geq$2 otherwise. Inversion was successful even for SNR as low as 2. 76
3.36 Total magnetic charge of 15 standard ordnance as a function of time. Data acquired over test stand with EM-63 sensor at 26 channels. Only median is shown for clarity, standard deviations similar to those of Figure 3.32. Note: there are 2 types of 81 mm items, the ATC and Montana. 78
3.37 Canonical analysis of the 15 standard UXOs shown in Figure 3.36. Left panel: eigenvalues. Right panel: representation of features from total magnetic charges taken at different depths and orientations in plane of the two first eigenvectors. 79
3.38 Total magnetic charge of six types of cylinders as a function of time using EM-63 data taken over a test stand. SSL: solid steel long, SSS: solid steel short, HSL: hollow steel long, HSS: hollow steel short, SAL: solid aluminum long, SAS: solid aluminum short. 80

3.39 Total magnetic charge of 13 standard UXO items as a function of time, for data acquired with an GEM-3 sensor over Vicksburg test stand. Only median is shown for clarity, variance is illustrated in canonical analysis of Figure 3.40. 81
3.40 Canonical analysis on GEM-3 data for 13 classes of items. Left panel: total magnetic charge obtained for all positions measured on test stand. Central panel: eigenvalues. Right panel: representation of features from total magnetic charges taken at different depths and orientations in plane of the two first eigenvectors. 82
3.41 Field test of NSMC. Total magnetic charge for three buried items, shown in thick lines, overlaid on top of the total magnetic charge derived for the same ordnance on test stand. 82
3.42 Effect of depth on the total magnetic charge. Upper panel: charge vs. time; lower panel: correlation between observation and prediction. 83
3.43 Percent change of the total magnetic charge when the model depth is offset from the true depth. . . 84

List of Tables

2.1 RSS-library targets 16

3.1 Magnetic charge results for the sphere tests. 49
3.2 Magnetic charge results for the spheroid tests. 49
3.3 40 mm object in horizontal position, 25 cm below sensor, 1st time channel. Φ_{d} is model misfit; $\|1/\mathbf{W}_d\|$ is the assigned error (from automated estimate of standard deviation of data and instrument error); $\|\Delta E\|$ is noise added to noise-free data; $E(\Phi_{\mathrm{d}})$ is the expected noise as in $\mathbf{W}_d$, departure from 1 means that automated guess on noise level was inaccurate. The method is deemed successful if Φ_{d} is close to $\|\Delta E\|$ and Q to Q_{uni}. 71
3.4 40 mm object, 45° inclination, 25 cm below sensor, 1st time channel. 72
3.5 Depth and inclination of measurements over test stand. 72
3.6 Mean and standard deviation of Q_{uni}, the total magnetic charge for uniform distribution of normalized surface charge density, at 1st (T_1) and 12th (T_{12}) time channels. 73

Acronyms

3D Three-dimensional

ATC Aberdeen Test Center

APT Armor Piercing with Tracer

BOR Body of Revolution

BAA Broad Area Announcement

EM Electromagnetic

EMI Electromagnetic Induction

ERDC Engineer Research and Development Center

FDM Finite Difference Method

FEM Finite Element Method (frequency domain)

GLRT Generalized Likelihood Ratio Test

HEAT High Explosive Anti Tank

Hz Hertz

MAS Method of Auxiliary Sources

MoM Methods of Moments

MTANG Montana Army National Guard

NSMC Normalized Surface Magnetic Charge

RSS Reduced Set of Sources

SEA Standard Excitation Approach

SERDP Strategic Environmental Research and Development Program

SIBC Surface Impedance Boundary Condition

SMC Surface Magnetic Charge

SNR Signal-to-Noise Ratio

TEM Transient Electromagnetic Method (time domain)

TMC Total Magnetic Charge

TNMC Total Normalized Magnetic Charge

TSA Thin Skin Approximation

TPT Target Practice with Tracer

TSA Thin Skin Approximation

USACE U.S. Army Corps of Engineers

UXO Unexploded Ordnance

Chapter 1

Introduction

The research described in this report was conducted in support of SERDP SEED Broad Agency Announcement, Statement of Need UXSEED-05-02, "Innovative Approaches to UXO Cleanup." A SERDP SEED research and development project UX-1446 entitled "A Unified Approach to UXO Discrimination Using the Method of Auxiliary Sources" was proposed in response to the above BAA.

Several data processing techniques for geophysical survey data have been developed for discriminating between UXO and non-UXO items. Current Electromagnetic Induction (EMI) data processing practices involve inverting sensor data for dipole parameters, and then applying statistical classification techniques to the recovered parameters. The dipole model is an attractive modeling technique for UXO discrimination because: (1) it is very fast, (2) sensor data collected over UXO are nearly dipolar if we are not measuring the field at a close distance to the target (relative to target size), and (3) the parameters of the dipole model have a good physical basis and we have an understanding of how material properties, size, and shape affect the dipole model parameters. However, the secondary field for complex, heterogeneous targets will often appear non-dipolar, particularly if we are close to the target. Figure 1.1 compares the time domain electromagnetic response for a horizontal 105 mm projectile that is aligned parallel to the y-axis. The data were measured 1 m above the target, using a Geonics EM63 time domain electromagnetic sensor. Even though the data are collected 1 m from the target, there are still non-dipolar components in the signal. If the response was truly dipolar, we would expect a dipole whose axial excitation was horizontal and the response would have symmetry with respect to both x and y axes.

Typical EMI data processing steps are to invert sensor data for dipole parameters, and then to apply statistical classification techniques to the recovered parameters. A dipole parameter inversion method minimizes a data misfit function, and therefore attempts to fit both the dipolar and non-dipolar components of the signal. In the context of a dipole inversion, the non-dipolar components of the secondary field are essentially data noise. As a result this data noise is propagated through the inversion to produce inaccuracies in the recovered parameters. The model parameters (i.e., the position, orientation and polarization tensor components) will adjust to fit the non-dipolar components of the data. For example, the dipole inversion applied to Figure 1.1 predicts a target with a 5.7 degree dip in order to compensate for the non-symmetry in the data.

The initial objective of this research project was to apply the MAS as a modeling technique for inversion of UXO sensor data. The inputs, or model vector, for the MAS would be the target size, shape, and electromagnetic material properties. The MAS can model the non-dipolar components of the secondary field. This suggests that the spread of feature parameters for a MAS model would be relatively smaller than for dipole parameters. The overall objective of the project was to develop a general inversion methodology based on the MAS that could be used to invert any combination and configuration of magnetic, Transient Electromagnetic Method (time domain) (TEM) and Finite Element Method (frequency domain) (FEM) induction data. Specific objectives included (1) determine the feasibility of using the MAS forward model as the basis for the inversion of total-field magnetics, TEM and FEM induction data; (2) investigate the feasibility of using the MAS forward model as the basis for joint and/or cooperative inversion of any combination of magnetic, TEM and FEM induction data; and (3) determine the discrimination capability of the physical parameters recovered by our inversion for different combinations and configurations of sensors.

Through numerous comparisons between measured data, analytical solutions, and data modeled by the MAS, we found that the MAS is able to accurately model compact metallic objects, such as UXO. The MAS accurately

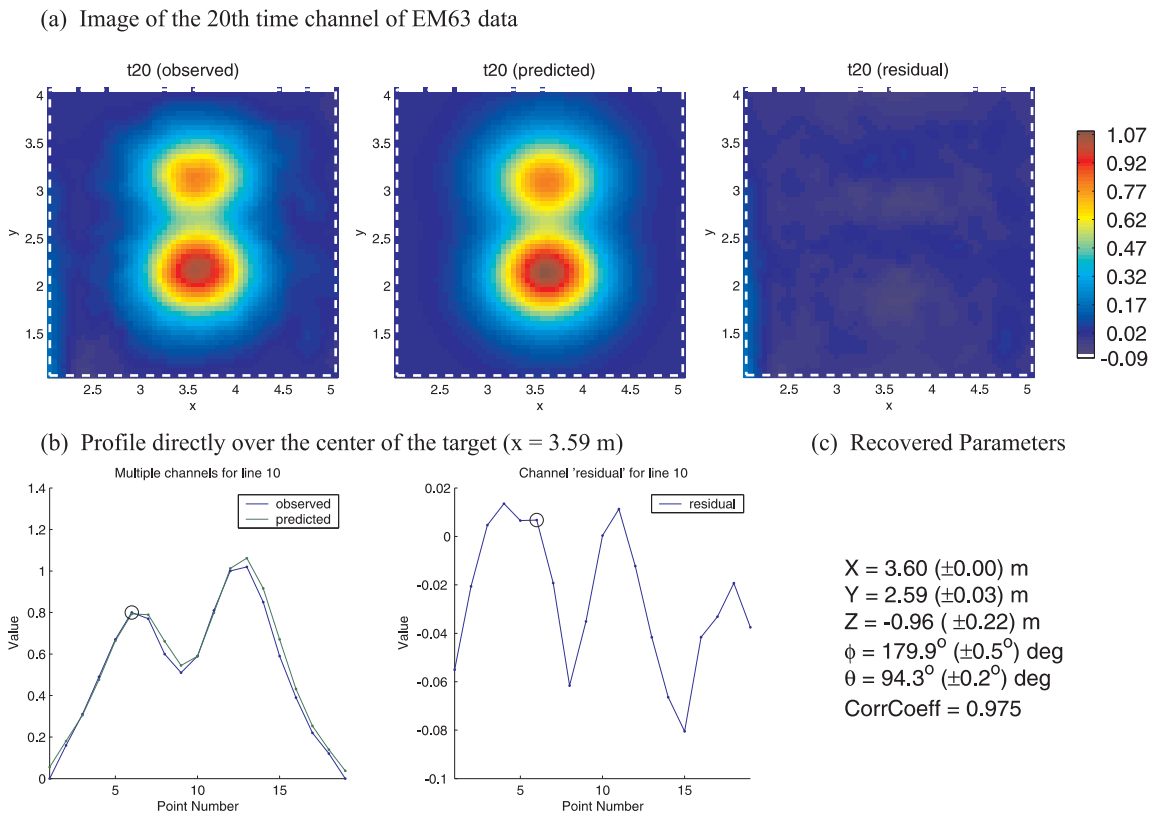

Figure 1.1: Results from inverting Geonics EM63 data collected over an 105 mm projectile.

modeled the EMI response over a large frequency range that extended to the static case (Figure 1.2, from Beran, 2005, Chapter 2). The ability to model over such a large range made the MAS an attractive modeling technique for joint inversion of multiple data sets. However, the computational time required by the MAS to calculate sensor data prevented us from applying the MAS for inversion purposes. Considering the accuracy of the MAS method, we revised the objective of this study to evaluate the potential of two modeling techniques derived from the MAS approach: the Standardized Excitation Approach and the Surface Magnetic Charge approach. Although the SEA and SMC are both surface magnetic charge distribution techniques, they represent two fundamentally different approaches to UXO discrimination. The SEA is used as part of a library or hypothesis testing technique, and the SMC is part of a parameter estimation/statistical classification technique.

The SEA approach involves determining a set of sources that are a function of target properties (i.e., shape, size, conductivity, and magnetic permeability) only. These sources are determined numerically through the application of MAS combined with a Thin Skin Approximation (TSA). The sources can then be forward modeled to generate either frequency or time domain sensor data. The SMC models the field with a magnetic charge distribution on a fictitious surface that encloses the target. The forward modeling is fast and, therefore, sensor data can quickly be inverted for the charge distribution. For a given location and orientation, the determination of the charge distribution is a linear inverse problem. The sum of the charge distribution, i.e., the total surface magnetic charge, can be used for discrimination.

This report is organized in the following manner. Chapter Two outlines our research and development of the SEA approach. The SEA approach involves determining a set of sources that represent target parameters that can be forward modeled to generate sensor data. These sources can be calculated for a number of targets in order to generate a source library. Discrimination is achieved by determining which target within the library has the greatest likelihood of producing the anomaly. Chapter Three outlines our research into the SMC modeling technique. The SMC approach models sensor data with the field from a magnetic charge distribution on a fictitious surface that encloses the target. The forward modeling is very fast and, therefore, sensor data can be inverted for the charge distribution. The sum of the charge distribution, i.e., the total surface magnetic charge, can be used

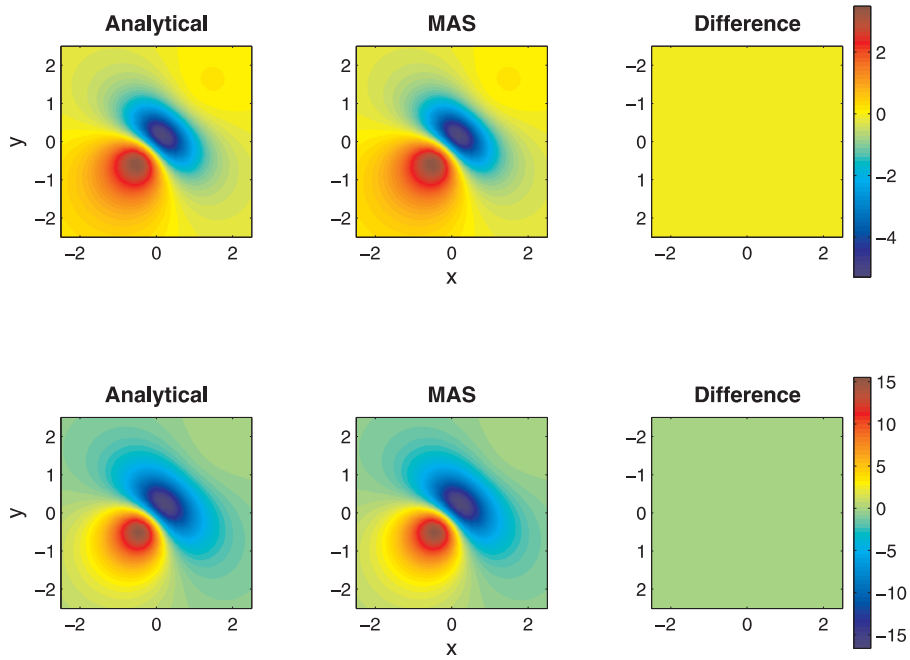

Figure 1.2: Modeling magnetostatic data with the Method of Auxiliary Sources method. A spheroid is modelled using the Earth's magnetic field at Yuma, Arizona. The analytical solution for a spheroid is used. The Method of Auxiliary Sources solution was obtained by assuming a frequency of 10^{-6} Hz.

for discrimination. Additional work studying the iso-sphere surfaces and a single horizontal charge layer is not presented here, as we chose to focus on the properties of the total magnetic charge applied to spheroidal surfaces. Chapter Four summarizes this report and suggests future research directions.

Chapter 2

Investigation of EMI Sensing for Metallic Objects: a Unified and Versatile Standardized Excitation Approach in Frequency- and Time- domain

2.1 Abstract

This chapter investigates the SEA combined with the MAS/TSA. This approach is a numerical technique for computing the EMI response from a three-dimensional, electromagnetically heterogeneous object in both near and far fields. The objective of the SEA is to determine a set of characteristic sources, called the Reduced Set of Sources (RSS), associated for each UXO. These sources can then be used for fast modeling of the EMI response. The full EMI solution is obtained by the superposition of responses to the spheroidal excitation modes. In this investigation, we determine the effective spheroidal modes by decomposing the primary field simulated for a loop transmitter. It is shown that the spheroidal series can be safely truncated at the maximum mode numbers $(M, N) = (3, 8)$ for the sensor target geometries encountered in the UXO problem. For this study, the frequency domain RSS has been determined for a collection of UXO items. This library of sources has been extended to time domain data through a convolution algorithm that can use an arbitrary current waveform in a TEM system. The experiment-based results, which are in both real frequency-domain (GEM-3) and time-domain (EM63) system, confirm its applicability to real-world sensors. As another illustration of using a RSS-library, we have conducted an identification test of UXO based on test stand data. In this test, we demonstrate that identifying a candidate UXO can be achieved through a straightforward pattern matching procedure by identifying a best misfit value below a threshold. We have also begun formulating the inverse problem of determining an object location and orientation by deriving the analytical expressions of the sensitivity coefficients of the fields with respect to these parameters. A simple example of location and orientation inversion is presented here.

2.2 Introduction

Improved cleanup of UXO requires data processing algorithms for discriminating objects of interest from clutter and metallic scrap. Reliable discrimination minimizes excavations and, therefore, reduces the cost and any associated danger. Accurate modeling of EMI responses from buried targets is an important component of a discrimination algorithm. Several forward modeling techniques have been proposed. The most common approach is to approximate a target's EMI response with a point dipole forward model. The dipole approximation is appropriate for modeling fields in the far-field regime, and has been successfully employed in UXO discrimination (Geng et al., 1999; Gao et al., 2000; Carin et al., 2001; Miller et al., 2001; Zhang et al., 2003; Pasion and Oldenburg, 2001). However, the near field EMI response often contains non-dipolar components. In particular, the EMI response near a heterogeneous UXO (consisting of multiple, different sections such as head, body, tail and fins,

and rotation copper band) depend strongly on which parts of the object are closer to the sensor and on the degree of coupling between different parts. In such a case the target would be poorly modeled with a point dipole. The importance of interaction effects when simulating target responses was investigated in Shubitidze et al. (2003); Shubitidze, O'Neill, Shamatava, Sun and Paulsen (2004); Shubitidze, O'Neill, Sun and Shamatava (2004). One technique that explicitly models a target's shape, volume, EM properties in modeling procedures of representative techniques is the MAS (Shubitidze et al., 2002; Shubitidze, O'Neill, Sun and Paulsen, 2004), later improved with the incorporation of the TSA (Sun et al., 2002, 2004). The hybrid MAS/TSA technique (Shubitidze, O'Neill, Sun, Shamatava and Paulsen, 2004) does not need fine mesh discretization within a target or on its surface, as stressed in the other numerical schemes like the Surface Impedance Boundary Condition (SIBC)-based three dimensional Methods of Moments (MoM) (Sebak et al., 1991) and the finite difference and finite element methods (FDM/FEM) when dealing with the situation of very small skin depth. These mesh-dependent techniques can be slow and even inaccurate, thus making them impractical in this context. In contrast, the MAS/TSA technique has demonstrated an ability to accurately solve the Three-dimensional (3D) full EMI response for a highly conducting and/or ferrous object in a relatively short time.

A class of SEA (Braunisch et al., 2001; Ao et al., 2002; Barrows et al., 2004; Chen et al., 2004; Sun et al., 2005; Shubitidze et al., 2005b) has been recently proposed to synthesize the full EMI solutions by the superposition of responses to the fundamental excitation modes. Importantly, these responses are unique for each UXO and can be stored as a library that is used to rapidly produce the complete EMI solutions for any location and orientation of the target. Chen et al. (2004) and Sun et al. (2005) applied the SEA to UXO discrimination by a pattern matching scheme using the library for some UXO. In their approach, an inverse problem was solved in which a source library is determined from high quality sensor data collected over each candidate UXO at different distances and orientations. The accuracy, reliability, and frequency band of the established library is limited by the measurement noise and numerical errors arising from the inherent ill-conditioning of the problem. Shubitidze et al. (2005b) presented an alternative way to implement the SEA based on the hybrid MAS/TSA technique. In this scheme, the modal response coefficients (or RSS) are distributed on a fictitious spheroid enclosing an object. The RSS is determined by employing a physically complete numerical simulation of an object's response to each fundamental mode. Determining the RSS using simulations allows us to avoid the non-uniqueness and ill-posed nature of fitting noisy sensor data. In principle, the RSS can be obtained very accurately for any excitation mode.

Our study of the SEA involves three major issues. First, it is known that the spheroidal approach theoretically involves an infinite series of fundamental spheroid modes for synthesizing fields. However it has to be truncated in practice. The determination of the effective spheroid modes in fact is fundamental for achieving computational efficiency while maintaining accuracy. We study this issue using simulated primary fields from loop transmitters with geometries typical for UXO surveys. Second, we illustrate that the modal response coefficients of a target can be used to accurately model both frequency and time domain sensor data by presenting the tests against the measurements collected by a GEM-3, a wideband frequency-domain sensor developed by Geophex Ltd., and EM63, a time-domain instrument developed by Geonics Ltd. These tests are used to demonstrate the capability of the MAS/TSA-based spheroidal approach as a unified EMI modeling tool in both frequency and time domain. A convolution algorithm is used to model the time domain response from an arbitrary transmitter waveform. Third, we have started to build a RSS-library for several UXO utilizing the MAS/TSA-based SEA. To demonstrate the use of a RSS-library at this stage, we apply a straightforward pattern matching procedure to carry out the identification tests of UXO by inspecting a minimum misfit value between the measured and calculated patterns of secondary fields.

2.3 The Standardized Excitation Approach Method

This section briefly describes the standardized (spheroidal) excitation approach detailed in Shubitidze et al. (2005b).

2.3.1 Decomposing a Primary Field

Under the quasi-magnetostatic approximation, a magnetic field outside of an object is irrotational. It follows that the corresponding scalar magnetic potential satisfies the Laplace equation and can be expanded in a Fourier-Legendre series (Arfken, 1995) in a prolate spheroidal coordinates. The prolate spheroid is chosen since it can

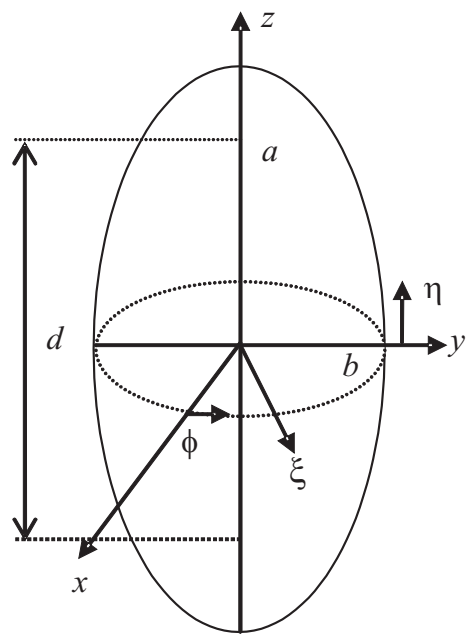

Figure 2.1: The prolate spheroidal coordinate system (η, ξ, ϕ) with major and minor semi-axes of a and b, the interfocal distance of $d = 2\sqrt{a^2 - b^2}$, and $\xi = \xi_0 = 2a/d$.

conform to an elongated body of revolution, a typical geometry of UXO. Let us denote (η, ξ, ϕ) as the standard prolate spheroidal coordinates with $-1 \leq \eta \leq 1$, $1 \leq \xi \leq \infty$, $0 \leq \phi \leq 2\pi$ and the inter-focal distance of d, as shown in Figure 2.1. On a fictitious spheroid $\xi = \xi_0$ surrounding an object, a primary potential field ψ^{pr} can be expressed as:

$$\psi^{\mathrm{pr}}(\eta, \xi_0, \phi) = \frac{H_0 d}{2} \sum_{m=0}^{M} \sum_{n=m}^{N} \sum_{p=0}^{1} b_{pmn} P_n^m(\eta) P_n^m(\xi) T_{pm}(\phi), \tag{2.1}$$

where P_n^m are associated Legendre functions of the first kind with degree n and order m (Arfken, 1995), and $T_{pm}(\phi)$ is $cos(m\phi)$ for $p = 0$ and is $sin(m\phi)$ for $p = 1$, b_{pmn} the spheroidal expansion coefficients. Eq. (2.1) is a decomposition of a primary magnetic potential into a number of fundamental excitations $P_n^m(\eta) P_n^m(\xi) T_{pm}(\phi) = \psi_{pmn}^{\mathrm{pr}}(\eta, \xi_0, \phi)$ with the maximum numbers of M and N, being infinity in theory. Taking a gradient operation of Eq. (2.1), one namely obtains the decomposition of the primary magnetic field $\mathbf{H}^{\mathrm{pr}}$. Its normal component $H_\xi^{\mathrm{pr}}(\eta, \xi, \phi)$ on the spheroid can be written as

$$H_\xi^{\mathrm{pr}}(\eta, \xi, \phi) = -\frac{H_0 d}{2} \frac{1}{h_\xi} \sum_{m=0}^{M} \sum_{n=m}^{N} \sum_{p=0}^{1} b_{pmn} P_n^m(\eta) P_n'^m(\xi) T_{pm}(\phi) \tag{2.2}$$

where $P_n'^m$ is the first-order derivative of the associated Legendre function with respect to ξ, h_ξ is the metrical coefficient. By the orthogonality of the associated Legendre functions, the spheroidal expansion coefficients b_{pmn} can be derived as

$$b_{pmn} = -\frac{2n+1}{\gamma \pi H_0 d P_n'^m(\xi_0)} \frac{(n-m)!}{(n+m)!} \int_{-1}^{1} P_n^m(\eta) h_\xi \int_0^{2\pi} H_\xi^{\mathrm{pr}}(\eta, \xi_0, \phi) T_{pm}(\phi) d\phi d\eta, \tag{2.3}$$

where $\gamma = 2$ for $m = p = 0$ and $\gamma = 1$ otherwise. The integration in (2.3) is evaluated by a numerical integration. This completes the decomposition of a primary field quantity under quasi-static approximation.

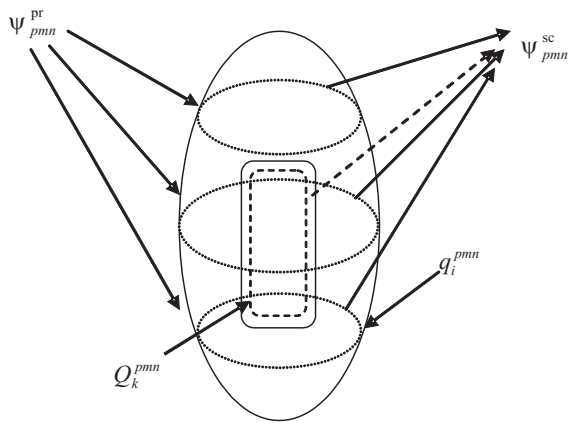

Figure 2.2: MAS/TSA-based SEA. Reduced set of sources q_i^{pmn} distributed along rings on the spheroid surface and the auxiliary sources Q_k^{pmn} distributed on an internal auxiliary surface of a cylinder-like object. Both induced sources are the response to fundamental excitation fields ψ^{pr}_{pmn} and produce the same scattered field ψ^{sc}_{pmn} outside of the object.

2.3.2 Synthesizing the Secondary Fields

We are interested in dealing with a Body of Revolution (BOR) that has rotational symmetry about the z-axis of a Cartesian coordinate in Figure 2.1. The symmetry property implies that the primary fields behave in a azimuthal dependence of $T_{pm}(\phi)$ as a Fourier series (as seen in Eqs. (2.1) and (2.2), and each primary azimuthal mode in the series is orthogonal. As a result, the secondary fields also preserve this angular dependence and can be expressed similarly in a Fourier series (Andreasen, 1965). Let us consider the object's response to each unit excitation $\mathbf{H}^{\mathrm{pr}}_{pmn}$ or ψ^{pr}_{pmn}. We can introduce the equivalent induced magnetic charges distributed along the ith ring on the fictitious (or inside) spheroidal surface in light of the rotational symmetry in Fig. 2.2. The secondary field $\mathbf{H}_{sc}(\mathbf{r})$ due to an object can be written as a linear superposition of the object's response for each pmn excitation mode (Chen et al., 2004; Sun et al., 2005), i.e.,

$$\mathbf{H}_{sc}(\mathbf{r}) = \sum_{m=0}^{M}\sum_{n=m}^{N}\sum_{p=0}^{1} b_{pmn}\sum_{i=1}^{N_q} q_i^{pmn}\mathbf{G}(\mathbf{r},\mathbf{r}_i'), \tag{2.4}$$

where $\mathbf{r}$ is the position vector of an observation point outside of the object (the spheroid), the $\mathbf{r}_i'$ is the position vector of the q_i^{pmn} along the ith ring, and $\mathbf{G}(\mathbf{r},\mathbf{r}_i')$ is the modal Green's function for the magnetic field and is given by

$$\mathbf{G}(\mathbf{r},\mathbf{r}_i')\frac{1}{4\pi\mu_0}\int_0^{2\pi}\frac{\mathbf{r}-\mathbf{r}_i'}{|\mathbf{r}-\mathbf{r}_i'|^3}\rho_i T_{pm}(\phi')d\phi', \tag{2.5}$$

where ρ_i is the radius of the ith ring. The modal Green's function can be understood physically as the vectorial field radiated by a unit scalar ring source harmonically varying in strength along the ring. By decomposing the primary fields in spheroidal coordinates, we solve the scattering problem on a mode-by-mode basis and then synthesize the scattered field by applying the superposition principle, as indicated in Eq. (2.4).

The pattern of the scattered field depends on intrinsic attributes of the scattering object (i.e., an object's geometry and physics), as well as extrinsic attributes of the object, such as object location, orientation and an excitation field. One way to look at UXO discrimination is as a procedure in which we try to separate the intrinsic and extrinsic attributes. From Eqs. (2.3) and (2.4), extrinsic attributes are characterized by the spheroidal expansion coefficients b_{pmn} and intrinsic attributes are characterized by the modal response amplitudes q_i^{pmn}. This is the essence of the SEA. Therefore once such response amplitudes are found for an object, they can be stored in a library for subsequent rapid computation of the response required in a prospective survey.

2.3.3 Solving for the Modal Response Coefficients: Reduced Set of Sources

Equation (2.4) suggests that a straightforward way to determine the RSS is to form an inverse problem and solve q_i^{pmn} for each mode corresponding to each ring, from the measured data. The success of this procedure would require numerous independent measurements of an object to physically reduce the degree of ill-posedness which can degrade the solution. Recently, Sun et al. (2005) applied such a data-derived approach to extracting the modal response coefficients for each candidate by carefully designing the measurements at different distances and orientations. However, the accuracy and reliability of the model parameters determined in this way is dependent on the measurement noise and numerical errors arising from the inherent ill-conditioning of the problem. In addition, a library generated using this approach is limited to the bandwidth of the sensor.

Shubitidze et al. (2005b) proposed a procedure in which the RSS are determined by employing a numerical simulation of an object's response to each fundamental excitation mode. For a unit excitation ψ_{pmn}^{pr} (Fig. 2.2), the scattered potential field outside the target is irrotational and can be written as

$$\psi_{pmn}^{\mathrm{sc}}(\mathbf{r}) = \sum_{i=1}^{N_q} q_i^{pmn} g(\mathbf{r}, \mathbf{r}_i'), \tag{2.6}$$

where

$$g(\mathbf{r}, \mathbf{r}_i') = \frac{1}{4\pi} \frac{1}{|\mathbf{r} - \mathbf{r}_i'|}, \tag{2.7}$$

is the potential at the $\mathbf{r}$ observation point produced by the ith ring source at $\mathbf{r}_i'$ on the spheroid surface where the q_i^{pmn} are located. Eq. (2.6) assumes that the field $\psi_{pmn}^{\mathrm{sc}}(\mathbf{r})$ can be quite accurately expressed for observation points outside an enclosing fictitious spheroid using q_i^{pmn}. For a given candidate target, the MAS can be used to compute the scattered fields. As an example, let us consider a cylindrical object enclosed by a spheroid (Figure 2.2). The MAS distributes a set of auxiliary charge with amplitudes of Q_k^{pmn}, $k = 1, \cdots, N_Q$, corresponding to unit excitation mode, on an auxiliary surface inside the scattering object. These auxiliary sources are obtained by enforcing the EM boundary conditions on the physical surface and these sources are responsible for the external fields (Shubitidze et al., 2002; Shubitidze, O'Neill, Sun and Paulsen, 2004). Thus with the known auxiliary charges Q_k^{pmn}, the scattered potential field for the pmn mode can be written as

$$\psi_{pmn}^{\mathrm{sc}}(\mathbf{r}) = \sum_{i=1}^{N_Q} Q_k^{pmn} g(\mathbf{r}, \mathbf{r}_k'), \tag{2.8}$$

where $\mathbf{r}_k'$ is the position vector of the kth auxiliary magnetic charge Q_k^{pmn}, located inside the object. The MAS (Shubitidze et al., 2002; Shubitidze, O'Neill, Sun and Paulsen, 2004) is used to produce the synthetic observed scattered potentials on the right-hand-side of Eq. (2.6). The modal response coefficients for each mode pmn can be solved via a linear system of equations $A\mathbf{q} = \psi$, where A is $J \times N_q$ a matrix whose jith elements given by Eq. (2.7), and $\mathbf{q} = [q_1^{pmn}, q_2^{pmn}, \cdots, q_{N_q}^{pmn}]^T$, a N_q-dimensional column model vector and $\psi = [\psi_{pmn}^{\mathrm{sc}}(\mathbf{r}_1), \psi_{pmn}^{\mathrm{sc}}(\mathbf{r}_2), \cdots, \psi_{pmn}^{\mathrm{sc}}(\mathbf{r}_J),]^T$, a J-dimensional column data vector. Note that the modal response coefficients are collectively called a *reduced* set of sources because its number is substantially less than the number of the auxiliary sources Q_k^{pmn} required in the MAS (Shubitidze et al., 2005b).

This model-based approach has the advantage over data-based approaches, because the corresponding inverse problem is more well-posed and the RSS can be more accurately obtained for any excitation mode and in an ultra-wide band with noise-free synthetic observed data.

2.4 Determination of Effective Spheroidal Modes

As described in section 2.3, the expressions (2.1) and (2.2) for the primary and secondary fields involve infinitely many terms in theory. In practice, it has to be truncated for computational efficiency. Therefore, to implement the SEA it is important to find the suitable maximum mode number M and N that can be used to accurately represent fields. This can be done sufficiently by examining the decomposition of primary fields; modes that have a negligible contribution to the primary field will have a negligible effect on the secondary fields. Mode

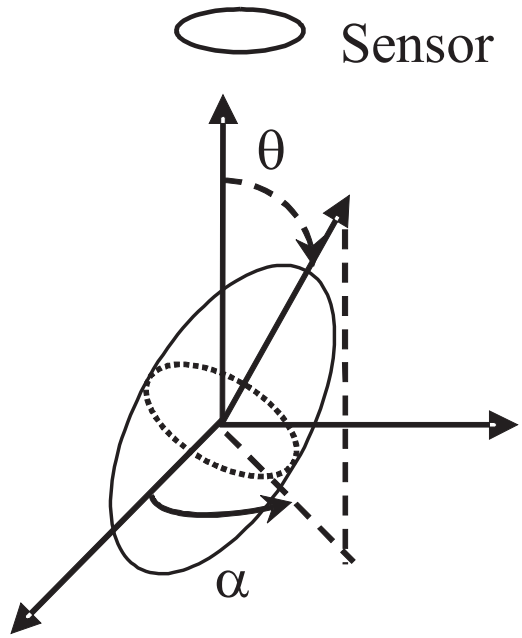

Figure 2.3: Sensing of a BOR-like object.

truncation requires correct determination of the corresponding spheroidal expansion coefficients b_{pmn} for each possible mode. In this investigation, we chose to decompose uniform and non-uniform fields from a simulated GEM-3.

2.4.1 Uniform Primary Field

Let us consider a uniform illuminating field $\mathbf{H} = \hat{z}$ and decompose the field on a spheroid with semi-major and -minor axes of $a = 11$ cm and $b = 5$ cm. The orientation of the spheroid is described by the azimuthal and polar angles (α, θ), as shown in Fig. 2.3. Due to rotational symmetry, we can illustrate the mode expansion to represent H_ξ^{pr} along a generating arc defined by an arbitrarily chosen spheroidal azimuthal coordinate of $\phi = \pi/4$.

Fig. 2.4 shows the comparison between the exact values and mode expansions. When $(\alpha, \theta) = (0^0, 0^0)$, i.e., the rotational axis of the spheroid is parallel to the direction of the uniform primary field, only one mode $(0, 0, 1)$ is necessary to exactly represent the field as shown in Fig. 2.4(a) and the use of extra terms $(p, 1, 1)$ in Fig. 2.4(b) or even higher (not shown here) has no contribution to this decomposition where the values of b_{pmn} are all identically zero. When the spheroid is oriented in $(\alpha, \theta) = (0^0, 45^0)$, the two modes $(0, 0, 1)$ and $(0, 1, 1)$ are needed to exactly synthesize the field H_ξ^{pr}. In this case, the primary field equivalently is decomposed into the axial and transverse excitations in the body coordinate-system. The field behaves like a two-dipole model. For the spheroid oriented horizontally along x-axis, i.e, $(\alpha, \theta) = (0^0, 90^0)$, this is a configuration of transverse excitation. Correspondingly, we see that in Figs. 2.4(c) and (d) the contribution is exactly zero from the mode $(0, 0, 1)$ and only the mode $(0, 1, 1)$ plays a role in the decomposition. The primary field modes $(0, 0, 1)$ and $(0, 1, 1)$ correspond to axial and x-transverse excitations, respectively. Similarly, the mode $(1, 1, 1)$ corresponds to y-transverse excitation.

With a uniform field, we examine its decomposition on the spheroid oriented in different angles, The examples are simple but provide some physical insight into the mode expansion and serve to check the stability and correctness of the algorithm to determine the b_{pmn}.

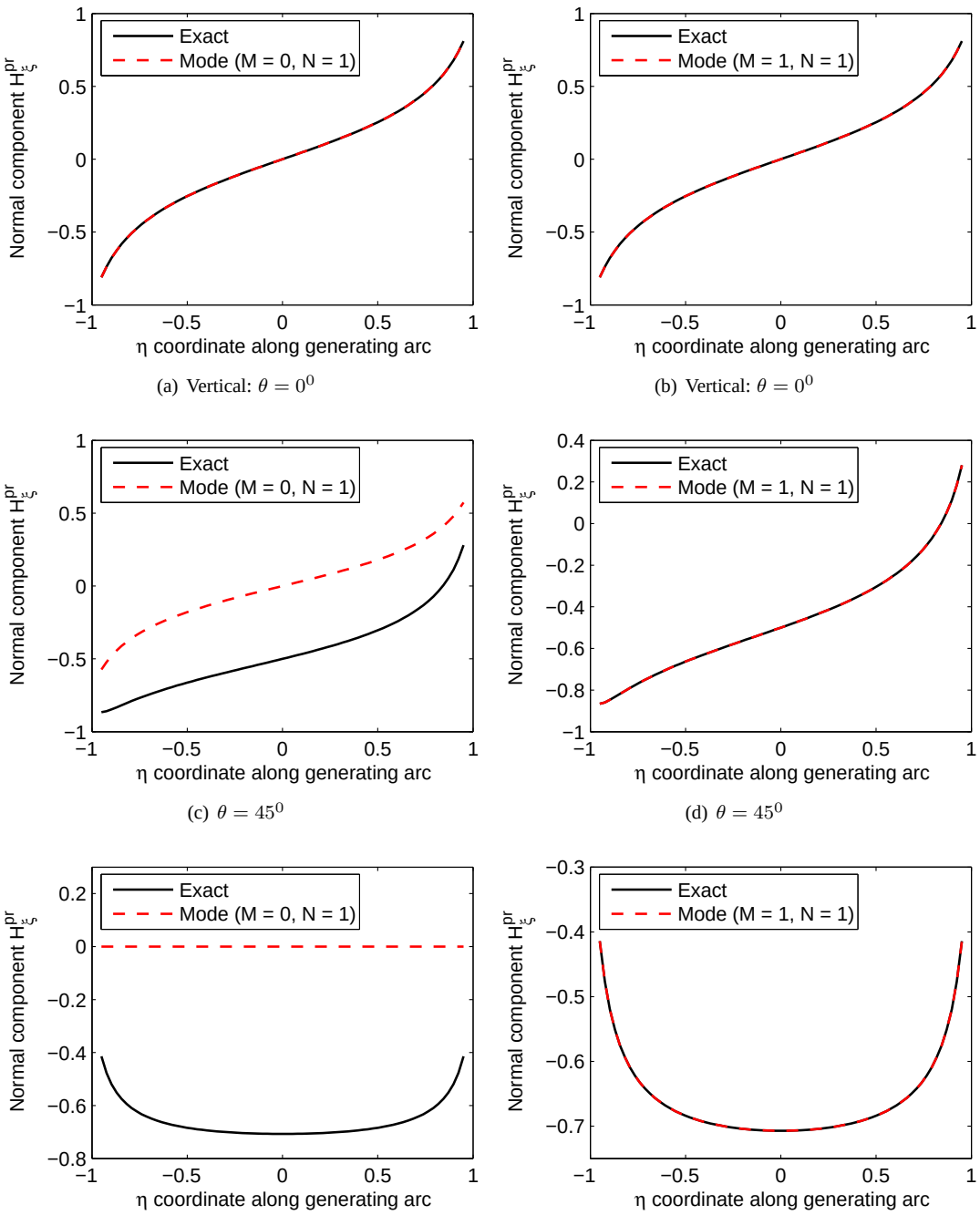

(a) Vertical: $\theta = 0^0$

(b) Vertical: $\theta = 0^0$

(c) $\theta = 45^0$

(d) $\theta = 45^0$

(e) Horizontal $\theta = 90^0$

(f) Horizontal $\theta = 90^0$

Figure 2.4: Spheroidal expansion of a uniform field $\mathbf{H} = \hat{z}$ on the spheroid with semi-major and minor axes $a = 11$ cm and $b = 5$ cm. The orientation of the spheroid is $\theta = 0^0$ for (a) and (b); $\theta = 45^0$ (c) and (d); $\theta = 90^0$ (e) and (f).

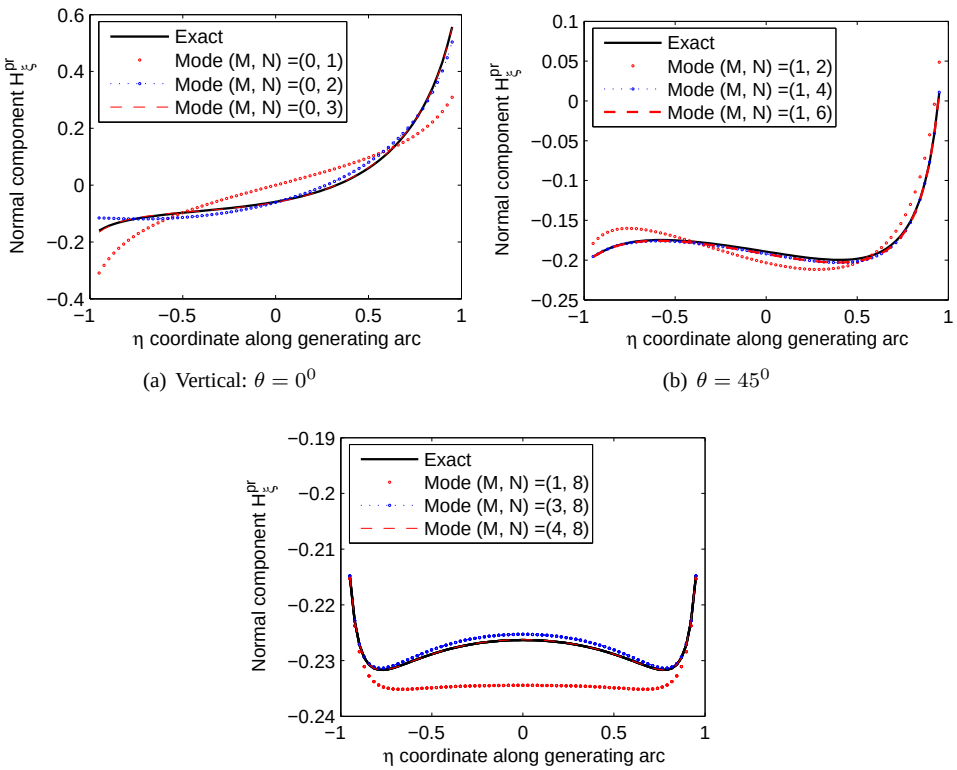

(a) Vertical: $\theta = 0^0$

(b) $\theta = 45^0$

(c) Horizontal $\theta = 90^0$

Figure 2.5: Spheroidal expansion of a non-uniform field from GEM-3 transmitter on the spheroid with semi-major and minor axes $a = 11$ cm and $b = 5$ cm. The vertical distance between the transmitter and the center of the spheroid is 29.2 cm. The orientation of the spheroid is (a) $\theta = 0^0$, (b) $\theta = 45^0$, and (c) $\theta = 90^0$.

2.4.2 Non-uniform Primary Field

We now consider the expansion of a spatially non-uniform field produced by a simulated GEM-3 instrument. The GEM-3 consists of two concentric circular transmitter coils connected in series but with opposite current-flow direction. By properly choosing the radius of the two coils and the number of turns of the coils the primary magnetic flux vanishes in the receiver loop. Therefore, the small receiving coil placed within this magnetic cavity senses only the secondary signal returned from the earth and nearby metallic objects.

In the first case, we consider an example where the vertical distance between the transmitter loops and the center of the spheroid is 29.2 cm. Their centers are aligned in the same vertical line. Fig. 2.5 presents the mode decomposition for the spheroid oriented in the three different polar angles. More terms for the non-uniform field are necessary to accurately express the field than the case for the uniform field. For the vertically oriented spheroid ($\theta = 0^0$), the accurate expansion requires $(M, N) = (0, 3)$. For the spheroid oriented in other two directions ($\theta = 45^0$),($\theta = 90^0$), we need the maximum number $(M, N) = (1, 6)$ and $(M, N) = (4, 8)$ to almost identically represent the field, respectively. For the transverse case, the relative error is around 0.33% when $(M, N) = (3, 8)$.

When the vertical distance between the loop and the center of the spheroid is reduced to 17 cm (thereby being the same scale as the outer loop), the degree of non-uniformity is increased. We see in Fig. 2.6 that more modes in this near field case are required to properly represent the non-uniformity of the near field pattern produced by the GEM-3 transmitter. For a transverse excitation, the synthesized fields with $(M, N) = (5, 8)$ are identical with the modeled transmit field and the relative error is around 0.40% when $(M, N) = (3, 8)$. The results show that more N modes are necessary to represent a non-uniform field, especially for a transverse-like excitation. In the following application, we truncated the series in the above equations at $(M, N) = (3, 8)$.

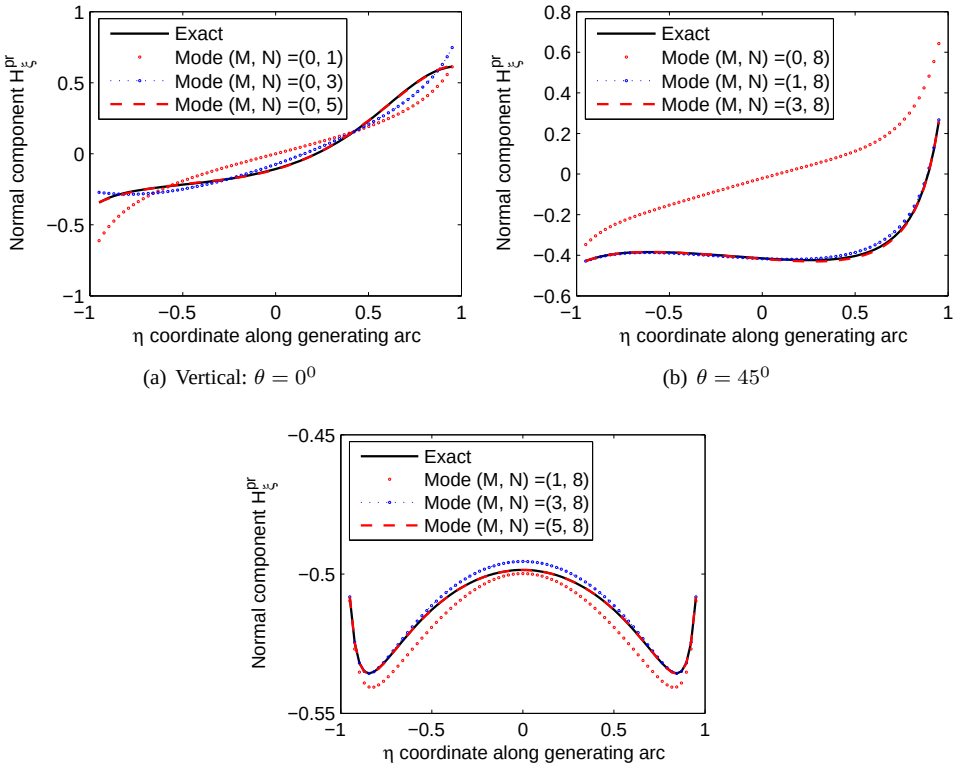

(a) Vertical: $\theta = 0^0$

(b) $\theta = 45^0$

(c) Horizontal $\theta = 90^0$

Figure 2.6: Spheroidal expansion of a non-uniform field from GEM-3 transmitter on the spheroid with semi-major and minor axes $a = 11$ cm and $b = 5$ cm. The vertical distance between the transmitter and the center of the spheroid is 17 cm. The orientation of the spheroid is (a) $\theta = 0^0$, (b) $\theta = 45^0$, and (c) $\theta = 90^0$.

2.5 An Example of SEA Modeling

Once the surface sources are available for an interested target, the SEA modeling of the EMI response involves determining the spheroidal modal expansion coefficients b_{pmn} for the excitation due to a target-sensor configuration. We demonstrate this by modeling the RSS for a solid steel cylinder with length of $L = 30.48$ cm and the diameter of $d = 7.5$ cm. The aspect ratio is $L/d \approx 4.06$.

We consider data from a GEM3 frequency-domain sensor manufactured by Geophex Ltd., and time-domain data collected using the Geonics Ltd. EM63. The GEM3 data were collected at the Sky Research Test Plot and the EM63 data were collected on the ERDC test stand.

2.5.1 Frequency-domain Response

In the frequency-domain measurements, the cylinder was excited transversely and axially. For both transverse and axial excitations, the vertical distance between the sensor and the center of the cylinder is $h = 42.75$ cm and $h = 45.24$ cm, respectively. Figs. 2.7(a) and (b) show the comparison between the measured and modeled data with frequency range of 90 Hz to 45 kHz for both excitations. The SEA modeling was very successful in modeling the measured EMI responses. The features of these responses conform to the previous studies (Shubitidze et al., 2002; Shubitidze, O'Neill, Sun and Paulsen, 2004). The crossover frequencies remain essentially fixed in Figs. 2.7(a) and (b). But the quadrature peak in the transverse excitation shifts to higher frequency, as compared to that in the axial excitation. In addition, by observing the quadrature peak frequencies f_t and f_a in transverse and axial excitation, we can estimate the aspect ratio as $\sqrt{f_t/f_a} = \sqrt{1470/90} \approx 4.04$, being quite close to the actual value of 4.06.

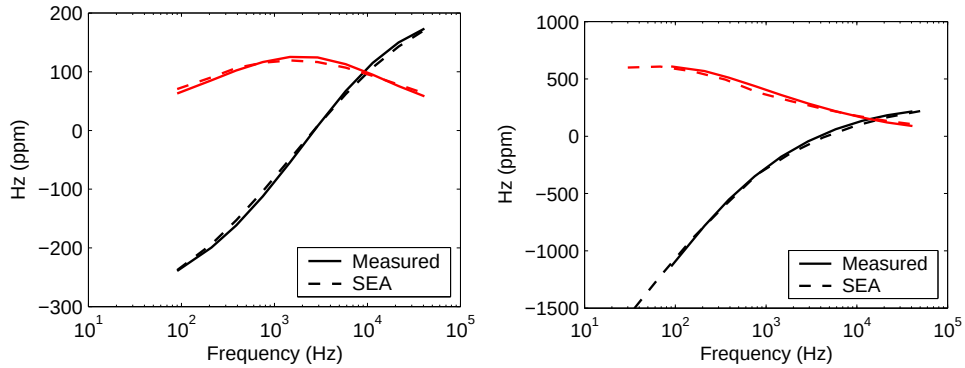

(a) Transverse excitation, $h = 42.75$ cm

(b) Axial excitation, h = 45.24 cm.

Figure 2.7: Frequency-domain response from GEM-3. h is the distance between the center of the cylinder ($L = 30.48$ cm, $d = 7.5$ cm) and the center of the GEM-3 receiver.

2.5.2 Transient EM Responses

We used a three step approach to modeling the TEM response: (1) calculate the response in the frequency domain, (2) use a Fourier transform to convert the frequency domain response to a time domain response and, (3) convolve the impulse response with the transmitter waveform.

The step-off and impulse responses in the time domain can be evaluated by applying the digital filter technique (Anderson, 1982) to the inverse cosine and sine transform (Newman et al., 1986) as follows

$$A(t) = -\frac{2}{\pi}\int_0^\infty \mathrm{Im}B(\omega)\frac{1}{\omega}\cos\omega t d\omega, \tag{2.9}$$

where $A(t)$ represents a step-off response corresponding to a magnetic flux $B(\omega)$ in frequency domain and

$$A'(t) = \frac{2}{\pi}\int_0^\infty \mathrm{Im}B(\omega)\sin\omega t d\omega, \tag{2.10}$$

where $\mathrm{Im}B(\omega)$ represents an imaginary part of the magnetic flux and the prime indicates a derivative with respect to time t.

By using the convolution theorem (Arfken, 1995), the voltage in the time-domain is

$$\frac{dB(t)}{dt} = -\int_0^t A'(t-\tau)I'(\tau)d\tau - A(0)I'(t) - A'(t)I(0). \tag{2.11}$$

This equation represents the response of a system to a general input function $I(t)$ in terms of the response to a unit step function or delta function. The integration in Eq. (2.11) is numerically evaluated.

The transmitter waveform of the EM63 consists of an exponential current increase followed by a linear ramp off. The cylinder was oriented at polar angles of $\theta = 0^0, 45^0, 90^0$. For each of the three excitations, the vertical distances between the sensor and the center of the cylinder are $h = 60.00$ cm. Because we obtained the RSS in a wide frequency range, the transient responses were produced by an inverse Fourier transform of the associated frequency-domain signal using the above formulas. The comparison in Figs. 2.8(a) - (c) shows that the measured and modeled TEM responses agree well for these measured data.

2.6 Development of a Reduced Source Library

Once we determined that the SEA would be successful in modeling the sensor response, we established an RSS-library for 9 candidate UXO, as listed in Table 2.1 and Fig.2.9. These items include UXO from the Aberdeen Test Center (ATC) UXO test set and items provided to us by the Montana Army National Guard (MTANG). The targets represent a mix of different sized ordnance with different material compositions (steel, aluminum, copper), and

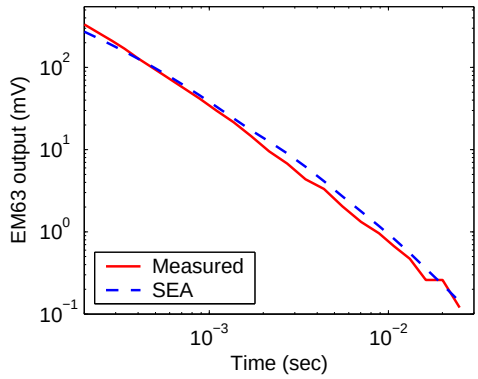

(a) Transverse excitation

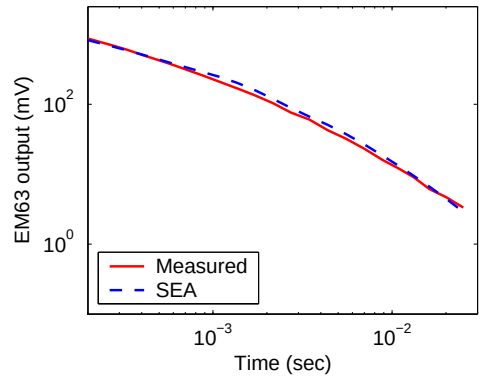

(b) Axial excitation

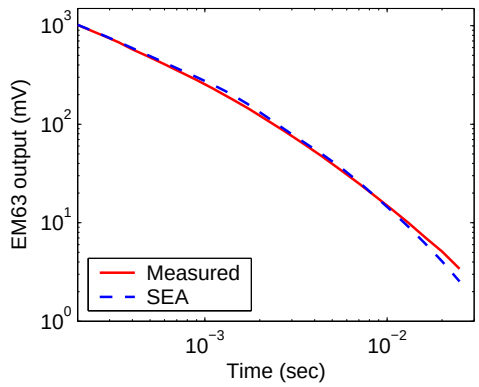

(c) Cylinder with a dip of 45 degrees

Figure 2.8: Transient response for the same solid steel cylinder in Fig. 2.7. For each measurement the cylinder is 60 cm from the measurement loop.

include projectiles, submunitions and mortars. Within this target set, UXO (i.e. a 2.75 inch rocket (labeled C7) and an 81 mm mortar (C8)) consisting of steel and aluminum sections would be challenging to model accurately in the near field with a single dipole model.

Candidate No.	Reference	Material	Total length (mm)
C1	M55	20 mm steel with thin cooper band	75
C2	M42	40 mm hollow steel	62
C3	M385	40 mm aluminium	75
C4	M86	57 mm projectile, thin cooper band near base	170
C5	M49A3	60 mm steel	130
C6	Montana	76 mm steel, Armor Piercing with Tracer (APT)	220
C7	M230	2.75” rocket, aluminium nose, steel body	400
C8	M374	81 mm steel body, aluminium nose and tail	460
C9	Montana	90 mm projectile, Target Practice with Tracer (TPT)	250

Table 2.1: RSS-library targets

Each target was photographed and digitized, such that each ordnance could be modeled as a body of revolution using the MAS. Each section of the target was represented by a cylinder. Target C7 and C8 were represented with 4 and 5 cylindrical sections, respectively. The conductivity and magnetic permeability of each section were determined by fitting data from a GEM-3 sensor collected at the Sky Research Test plot in Ashland, July 2005 (Figure 2.10). Each target was place horizontally beneath the GEM-3 sensor, and the frequency domain response

(a) C1: 20 mm M55

(b) C2: M42 Submunition

(c) C3: 40 mm M385

(d) C4: 57mm M86

(e) C5: 60 mm M49A3

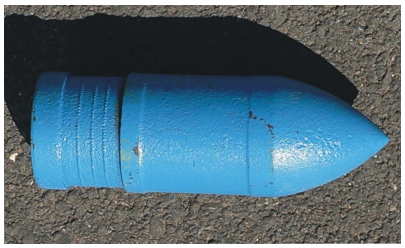

(f) C6: 76 mm from Montana Army National Guard

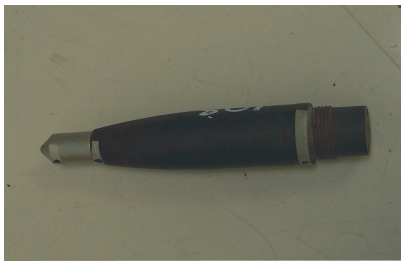

(g) C7: 2.75 inch Rocket, M230

(h) C8: 81 mm M374

(i) C9: 90 mm from Montana Army National Guard

Figure 2.9: Items for which RSS were computed.

Figure 2.10: Apparatus for acquiring data for determining the RSS.

was measured at operating frequencies of 90, 450, 930, 2010, 5970, 10050, 15450, 23010, 32010, and 44010 Hz. Although data were collected along a line over the target, only the frequency spectra measured directly over the center of the target was used for the fitting. Fitting these data was achieved through "trial and error". The off-center data were used as a check to determine the suitability of the selected permeability and susceptibility for modeling. Clearly, this procedure needs to be refined to ensure greater accuracy and repeatability.

The RSS library was built using three different sizes of spheroids with $a = 11.0$ cm, $b = 5.0$ cm for small objects, $a = 22.0$ cm, $b = 7.5$ cm for medium ones, and $a = 30.0$ cm, $b = 7.5$ cm for the largest items. On the surface of these spheroids, 12 rings of charge were used. Sun et al. (2005) used 6 rings in their analysis. Figures 2.11 and 2.12 contain the RSS models as a function of length along the spheroidal coordinate η, for targets C3 (40 mm aluminum submution) and C5 (60 mm steel mortar body) respectively.

Figure 2.13 compares the response of an 40 mm (C3) predicted using the RSS as depicted in Figure 2.11 assuming a GEM3 sensor, with data collected on the ERDC test stand. The target depth was 30 cm from the plane on which the GEM3 head moves. This target represents the most straightforward object from our library to model. It does not contain a number of different sections and is non-magnetic. The plan view images of Figure 2.13(a) and (b) show the real and imaginary parts for 3 of the 10 frequencies. The line plot at the bottom of each panel plots the frequency response measured and modeled directly above the center of the target (i.e. $(X, Y) = (0, 0)$. This target response was very accurately modeled using the RSS from our library.

Figure 2.14 compares the response of an 81 mm (C8) modeled with the RSS and GEM3 sensor data. The target depth was 50 cm from the plane on which the GEM3 moves. This target represents a much more challenging item to model. The ATC 81 mm contained several different sections; both ferrous and non-ferrous.

The crossover of the real and imaginary parts is slightly different between measured response and modeled response. However, as is seen in the plan data, at the higher and lower frequencies the plan view images, and therefore the data, match closely. The slight inaccuracy of the crossover suggests more care should be made when calculating the RSS for the larger, more complex targets. Regardless, the comparison between predicted and measured data is quite good, and we proceed with testing discrimination using our RSS library.

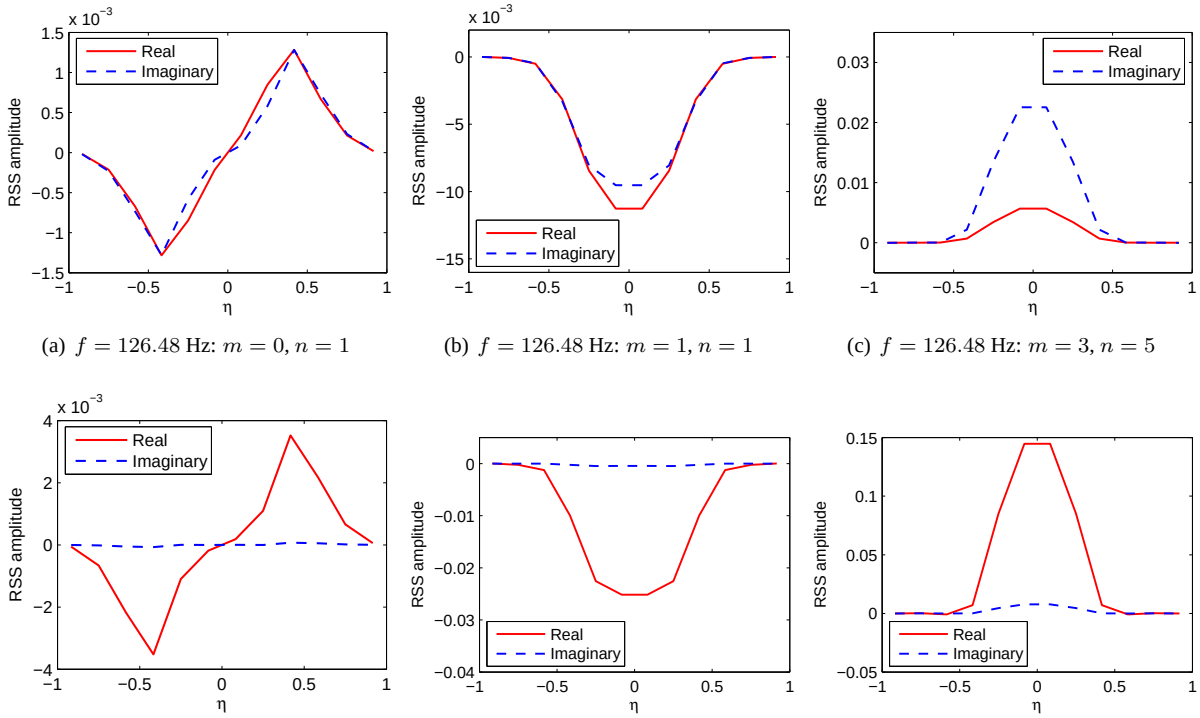

(a) $f = 126.48$ Hz: $m = 0, n = 1$ (b) $f = 126.48$ Hz: $m = 1, n = 1$ (c) $f = 126.48$ Hz: $m = 3, n = 5$

(d) $f = 10481.13$ Hz: $m = 0, n = 1$ (e) $f = 10481.13$ Hz: $m = 1, n = 1$ (f) $f = 10481.13$ Hz: $m = 3, n = 4$

Figure 2.11: The distribution of RSS for C3 along a spheroidal coordinate η.

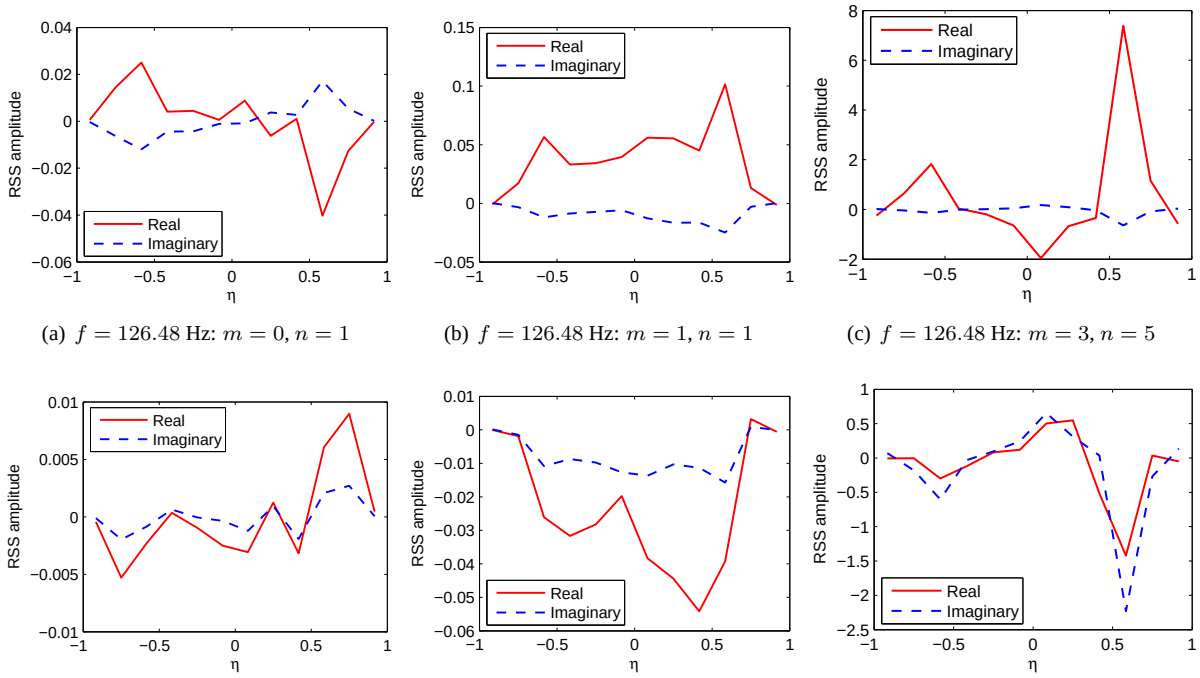

(a) $f = 126.48$ Hz: $m = 0, n = 1$ (b) $f = 126.48$ Hz: $m = 1, n = 1$ (c) $f = 126.48$ Hz: $m = 3, n = 5$

(d) $f = 10481.13$ Hz: $m = 0, n = 1$ (e) $f = 10481.13$ Hz: $m = 1, n = 1$ (f) $f = 10481.13$ Hz: $m = 3, n = 4$

Figure 2.12: The distribution of RSS for C5 along a spheroidal coordinate η.

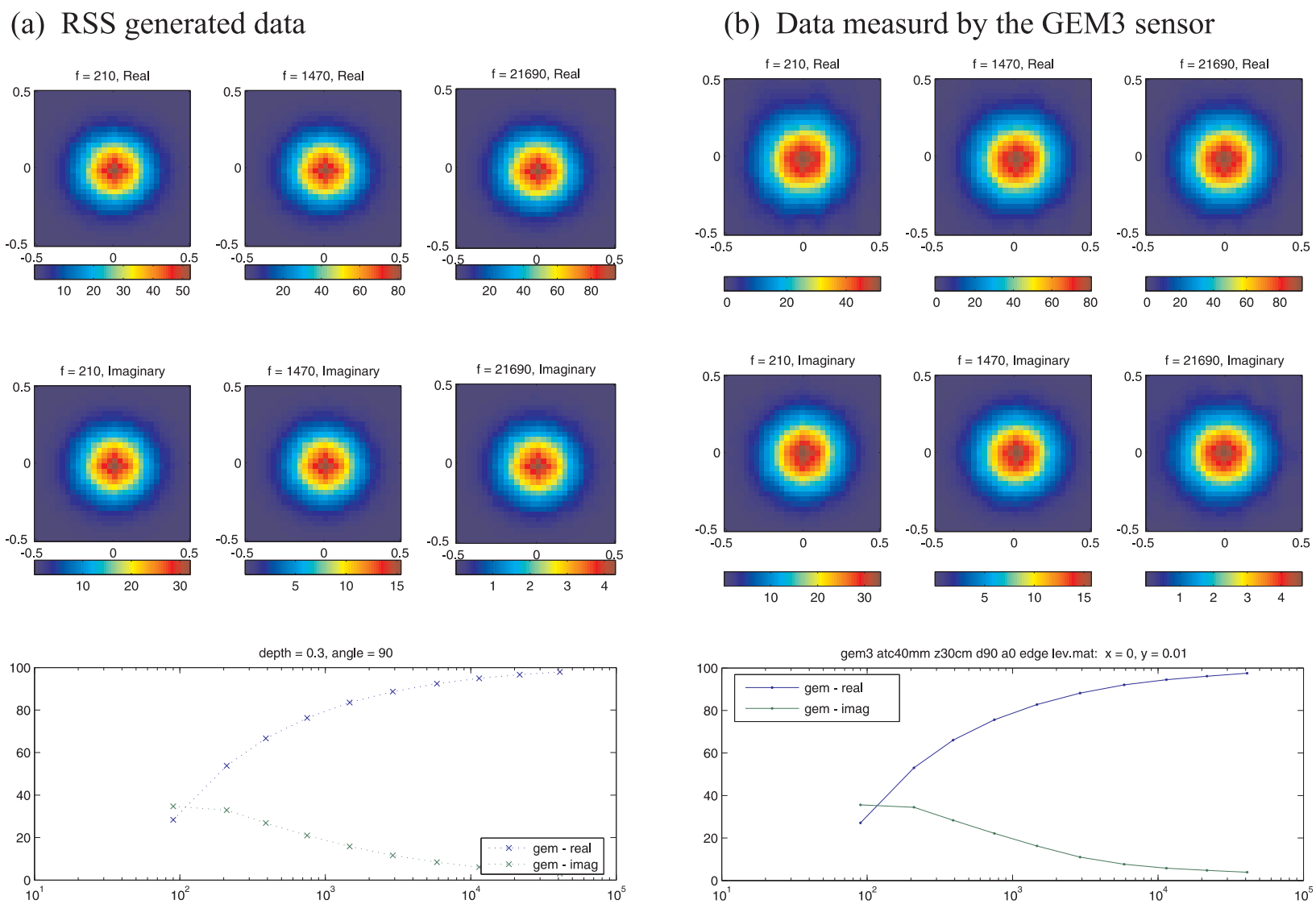

Figure 2.13: Modeled and measured GEM3 response for a horizontal ATC 40 mm (C3).

(a) RSS generated data

(b) Data measurd by the GEM3 sensor

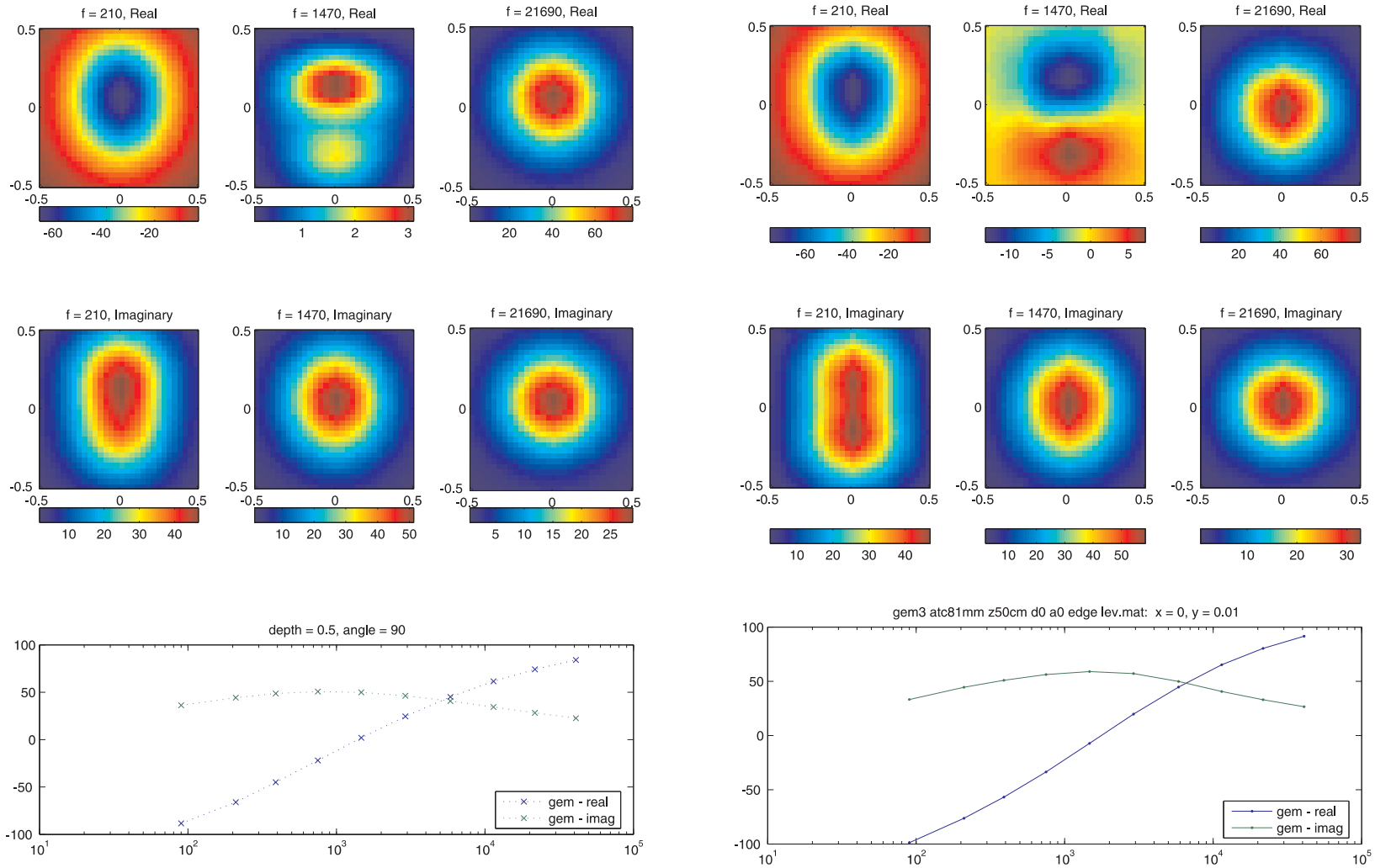

Figure 2.14: Modeled and measured GEM3 response for a horizontally ATC 81mm (C8).

2.7 UXO Identification Tests

The above examples illustrate the applicability of the MAS/TSA-based SEA for the fast and accurate EMI modeling. This modeling technique is readily inserted into "fingerprinting" or template matching type discrimination/classification algorithms. The objective of our template matching analysis is to determine, from a list of M targets, the target that is most likely to have generated the observed data $\mathbf{d^{obs}}$. Each target in our list is characterized by its RSS, which is represented by the vector $\mathbf{p}_i$. For each RSS in our library, we determine the location $\mathbf{r}_i$ and orientation angles θ_i and ϕ_i, at which we can best fit the observed data $\mathbf{d^{obs}}$ by obtaining the maximum likelihood solution. The data predicted by this recovered model, $\mathbf{d}_i^{\mathbf{pred}} = F[\mathbf{r}_i, \theta_i, \phi_i, \mathbf{p}_i] = F[\mathbf{m}_i]$, is referred to as the template for target i. The target template $\mathbf{d}_i^{\mathbf{pred}}$ most similar to the observed data $\mathbf{d^{obs}}$ is selected as the most likely target.

There are a number of measures that compare the target templates with the observed data. Intuitively, these include measures of maximum correlation or minimum error. There are also several ways with which to define the minimum error. Riggs et al. (2001) outline the derivation of the minimum least squares from a generalized likelihood ratio test (GLRT) with Gaussian data statistics. The likelihood ratio test for two targets

$$\frac{p\left(\mathbf{d}_{obs}|\mathbf{p}_1\right)}{p\left(\mathbf{d}_{obs}|\mathbf{p}_2\right)} \underset{target2}{\overset{target1}{\lessgtr}} \frac{p\left(\mathbf{p}_2\right)\left(C_{01}-C_{11}\right)}{p\left(\mathbf{p}_1\right)\left(C_{12}-C_{22}\right)} \equiv \eta \tag{2.12}$$

where C_{ij} is the cost of classifying the target as $\mathbf{p}_i$ when the target is $\mathbf{p}_j$, and $p\left(\mathbf{p}_i\right)$ is the prior probability for the ith class. The GLRT is obtained by substituting the maximum likelihood estimate into equation 2.12. If we consider two targets with equal prior probability of producing the anomaly, and assuming that an incorrect classification produces the same cost, then $\eta = 1$. By taking the logarithm of the resulting expression, our decision criterion is to simply select the target that has the smallest least squares error:

$$\|V_d^{-1/2}\left(\mathbf{d^{obs}} - F[\mathbf{r}_1, \theta_1, \phi_1, \mathbf{p}_1]\right)\|^2 \underset{target2}{\overset{target1}{\lessgtr}} \|V_d^{-1/2}\left(\mathbf{d^{obs}} - F[\mathbf{r}_2, \theta_2, \phi_2, \mathbf{p}_2)]\right)\|^2 \tag{2.13}$$

where $\mathbf{r}_i$ is the position, and θ_i, and ϕ_i are the orientation angles that produces the best fit to the observed data for the model $\mathbf{p}_i$. For multiple candidate targets we simply choose the target with smallest least squares misfit.

Application of the above algorithm to survey data requires establishing two thresholds. First, a minimum level of data quality must be established, since our confidence in identifying the correct target decreases as the data quality degrades. For data sets acquired with the same survey parameters (such as station density) for the entire data set, the critical measure of data quality is the signal to noise ratio (SNR). A second threshold is a maximum misfit at which an anomaly can be labeled as a target within our library. Since the ability to distinguish differences between the observed data and the template data will depend on the quality of data, the minimum correlation threshold will also be dependent on the Signal-to-Noise Ratio (SNR) ratio of the target. These thresholds can be established with training data or, if the survey noise can be accurately modeled, through simulations.

2.7.1 A simple discrimination example using a single sounding

For a first test, we consider a very simplified example. For this test we use the 9 candidate patterns of the scattered fields measured at different levels ranging from 15 cm to 30 cm above the objects, being positioned at (0, 0, 0) cm and oriented at $(\alpha, \theta) = (0^0, 90^0)$. This example does not represent a realistic discrimination test, but rather serves as a simple test of the variations in soundings that are generated by the different members of the library and illustrates the basic idea of the pattern matching. To be consistent with Sun et al. (2005), we characterize the difference between the trial and candidate patterns with the following misfit function

$$F(C_i, C_j) = \frac{\sum_f |H_{\text{obs}}(f, C_i) - H_{\text{trial}}(f, C_i)|}{\sum_f |H_{\text{obs}}(f, C_i)|} \tag{2.14}$$

where $H_{\text{obs}}(f, C_i)$ are the measured candidate pattern of the scattered fields for unknown candidate C_i to be identified, and $H_{\text{trial}}(f, C_j)$ are the trial pattern of the secondary fields for UXO C_j on the basis of the RSS-library.

Given a candidate pattern, for instance, we can quickly scan the trial patterns with it and produce the misfit values as shown in Fig. 2.15. It can be observed that the minimum misfit value occurs for candidate C4. In fact

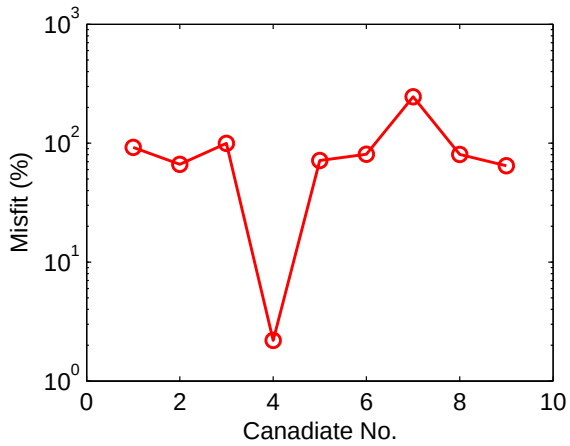

Figure 2.15: Misfit values for a trial identification test.

the value of $F(C_i, C_4)$ is only 2.2%; this is far smaller than other misfit values of $F(C_i, C_j), j \neq 4$. Assuming an error threshold of 10%, we are able to identify this unknown object as UXO C4 corresponding to the given candidate pattern. This identification result is confirmed by visually inspecting the patterns of the secondary fields between the calculated and the candidate in Fig. 2.16.

In another trial test, we sweep the other candidate pattern using the same RSS-library. The misfit values are presented in Fig. 2.17. Again, one can readily locate a minimum value of $F(C_i, C_8)$, being 3.4% below the error threshold value. The other values of $F(C_i, C_j), j \neq 8$ are much larger. Based on this, we can make a decision to identify this unknown object as UXO C8. Fig. 2.18 illustrates that UXO C8 is the only item with a good match between the trial and the measured data.

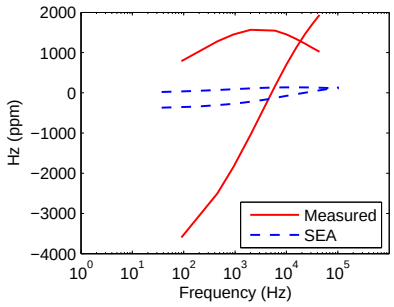

(a) C1: 20 mm M55

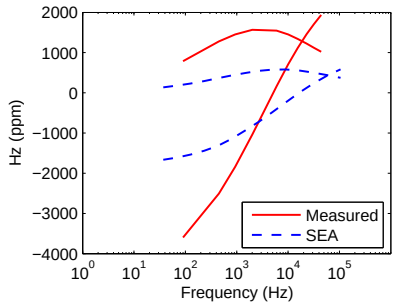

(b) C2: M42 Submunition

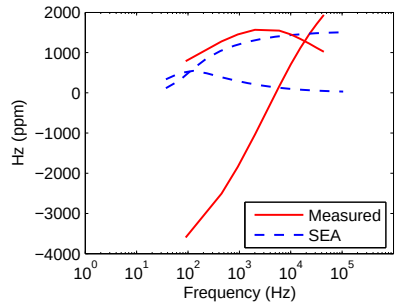

(c) C3: 40 mm M385

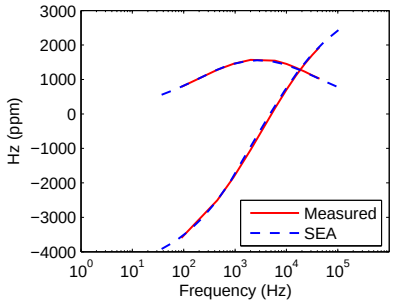

(d) C4: 57mm M86

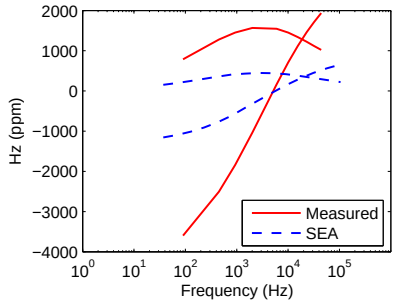

(e) C5: 60 mm M49A3

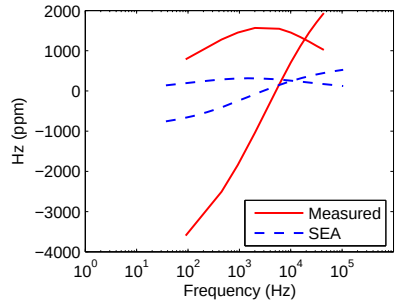

(f) C6: 76 mm from Montana Army National Guard

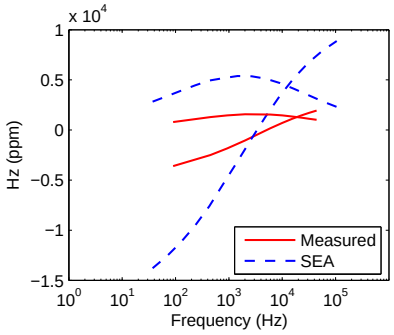

(g) C7: 2.75 inch Rocket, M230

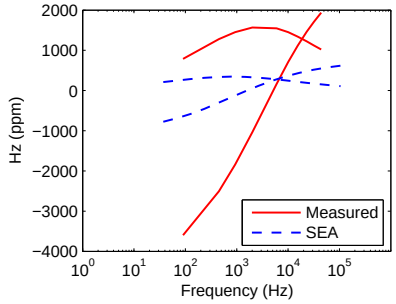

(h) C8: 81 mm M374

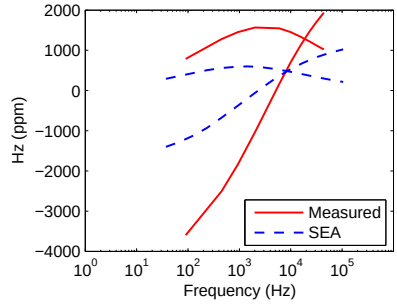

(i) C9: 90 mm from Montana Army National Guard

Figure 2.16: Pattern matching tests. (a)-(i): C1-C9. UXO C4 identified

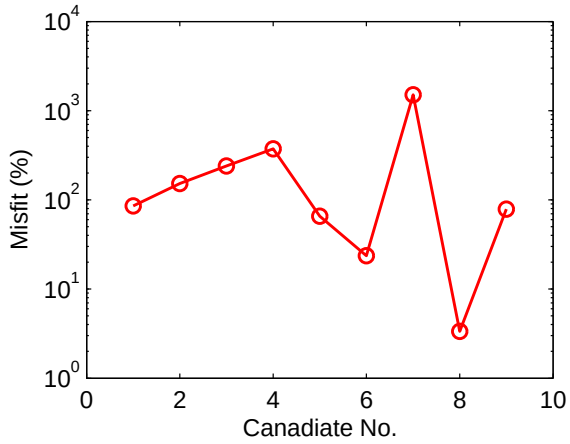

Figure 2.17: Misfit values for another trial identification test.

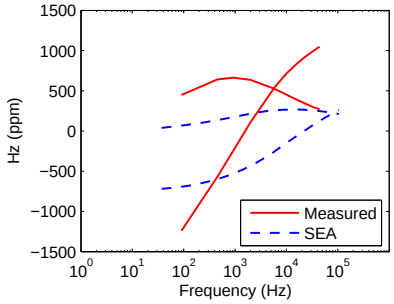

(a) C1: 20 mm M55

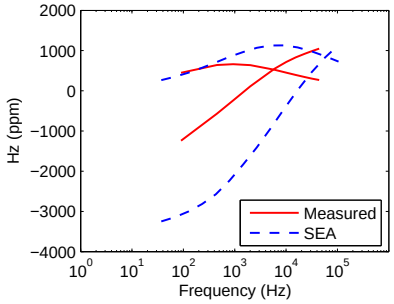

(b) C2: M42 Submunition

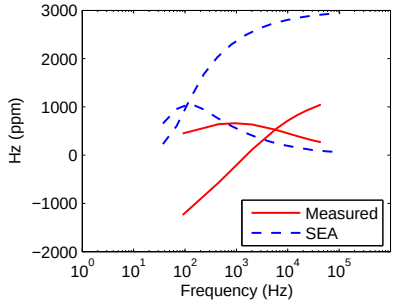

(c) C3: 40 mm M385

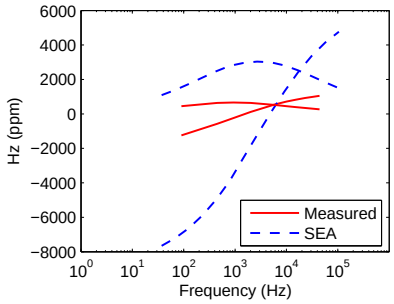

(d) C4: 57mm M86

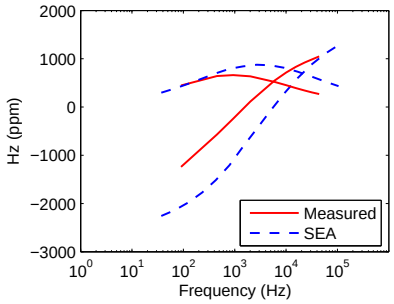

(e) C5: 60 mm M49A3

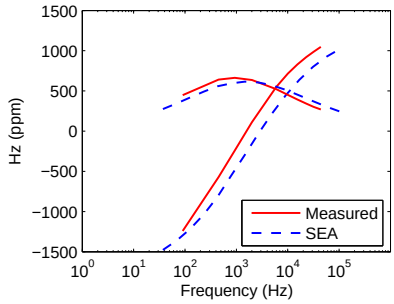

(f) C6: 76 mm from Montana Army National Guard

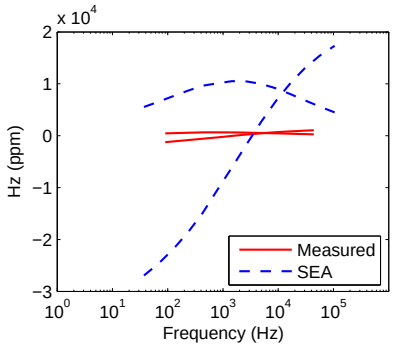

(g) C7: 2.75 inch Rocket, M230

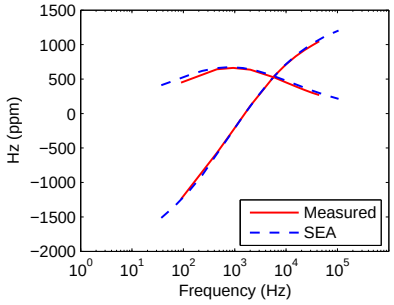

(h) C8: 81 mm M374

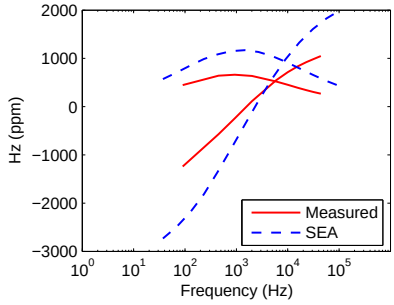

(i) C9: 90 mm from Montana Army National Guard

Figure 2.18: Pattern matching tests. UXO C8 identified

2.7.2 A discrimination example using GEM3 data collected on the ERDC Test Stand

The example presented in the previous section is not realistic, since location and orientation are not generally known prior to processing data. Although *a priori* information on position and orientation can sometimes be obtained from prior surveys, often the information is inaccurate. The initial plan was to implement the same library based identification techniques as in Pasion et al. (2006). In that approach, a library of polarization tensors was created from time domain electromagnetic data collected on a test stand. For each target in our library a non-linear inverse problem was solved for the position and orientation that minimized the least-squares difference between the observed data anomaly and the data predicted from each target. Our code for inverting for location and orientation is being developed and is not mature enough to implement the non-linear inversion approach. On the other hand, our initially optimized RSS forward modeling code is able to rapidly yield the response with around 2.86 seconds per sounding of 13 frequencies. Therefore, we developed a template matching technique to determine depth and orientation by searching a library of data pre-modeled at several depths and dip angles and used image registration to find the location and azimuth angle of the target. The main objective of implementing this style of template matching is to determine if it is possible to identify targets using an RSS library without *a priori* information. We emphasize that we do not claim the algorithm presented here is the best choice for target identification, and we plan to implement the non-linear inverse problem approach in Pasion et al. (2006) at a later date.

The first step of the algorithm is to generate a library of UXO responses. The generation of a library of UXO responses meant that all the forward modeling using the RSS only needed to be performed once, thereby increasing the speed of the analysis. Target responses for items C1 to C9 were calculated for target distances from the GEM3 sensor head varying, at 10 cm intervals, from 20 cm to 80 cm. At each depth the target was measured at dip angles from 0 degrees (horizontal) to 90 degrees (vertical), at 15 degree intervals. Data were modeled on 1 m square area and on a uniform grid with 10 cm spacing.

UXO identification is achieved by determining the data template from our library that best matches the sensor data by cycling through each of the data templates. However, the target location and azimuthal orientation is unknown. Determining the target location and azimuthal orientation is equivalent to determining the translation and rotation of the data templates. This operation represents a simple problem in image registration, since we do not have to consider scaling the template. Figure 2.19 shows an example of determining the correct translation, and therefore an estimate of location. The upper left panel shows sensor data collected on a test stand. The upper right panel shows the 1 m square area of the template. Both the data and the template are gridded to 2.5 cm pixels. The lower left panel plots the correlation coefficient as a function of position. Not surprisingly, the optimal location is directly over the center. In the examples that follow, we do not implement an image registration technique and we assume that we know the azimuthal orientation and location. We note that while implementing an image registration algorithm is straightforward, we would like to focus on our ability to correctly determine depth and dip.

To demonstrate the above procedure, we used GEM3 data collected on the USACE-ERDC Test Stand. The data were collected from January 31, 2006 to February 10, 2006. For a first example we compare data from a vertical 40 mm projectile located 30 cm from the GEM3 sensor head. Figure 2.20 compares images of measured sensor data with the best fit template for 3 of the 10 GEM3 frequencies. Figure 2.21(a) compares the sounding directly over the center of the target. Figure 2.21(b) compares the misfit values for the different items in the RSS library. It is clear that C3 is the most likely target. The ease with which the algorithm picked C3 is, in part, due to C3 being the only non-ferrous (aluminum) item in the library.

Figures 2.22 and 2.23 plots the results when the data from an 81 mm (M374) is fit. Although the correct target (C8) has the minimum misfit, several other targets have relatively similar misfit values, indicating that several targets appear quite similar when viewed by a GEM3 sensor 50 cm from the target.

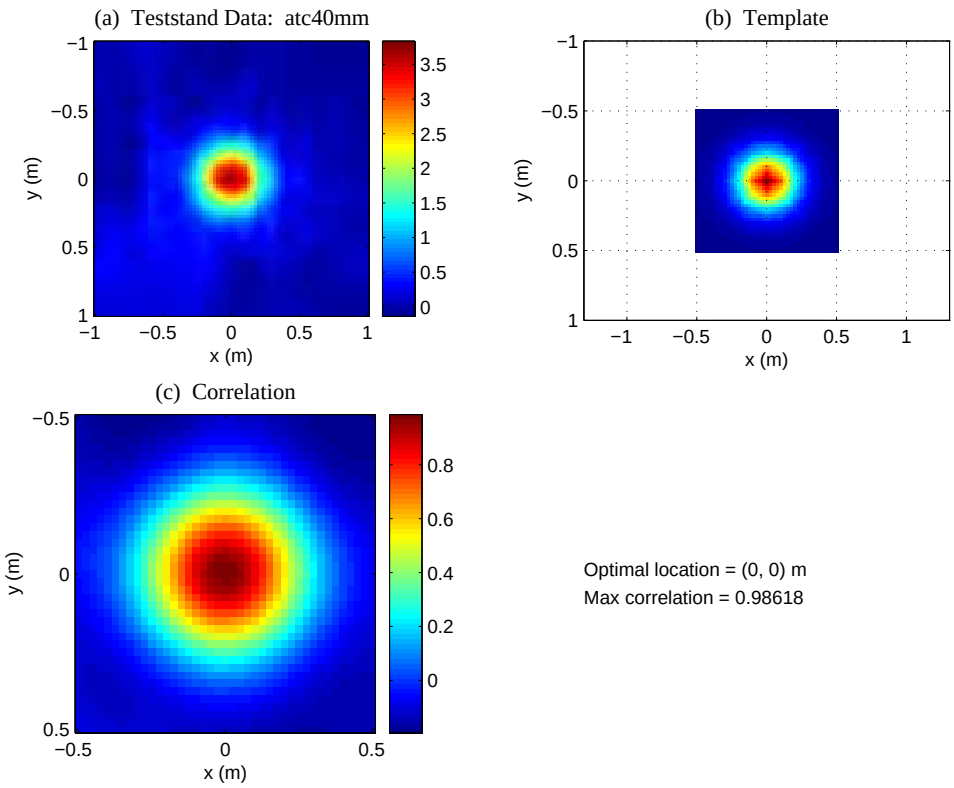

Figure 2.19: Examples of finding the optimal location by translating a template generated by the RSS.

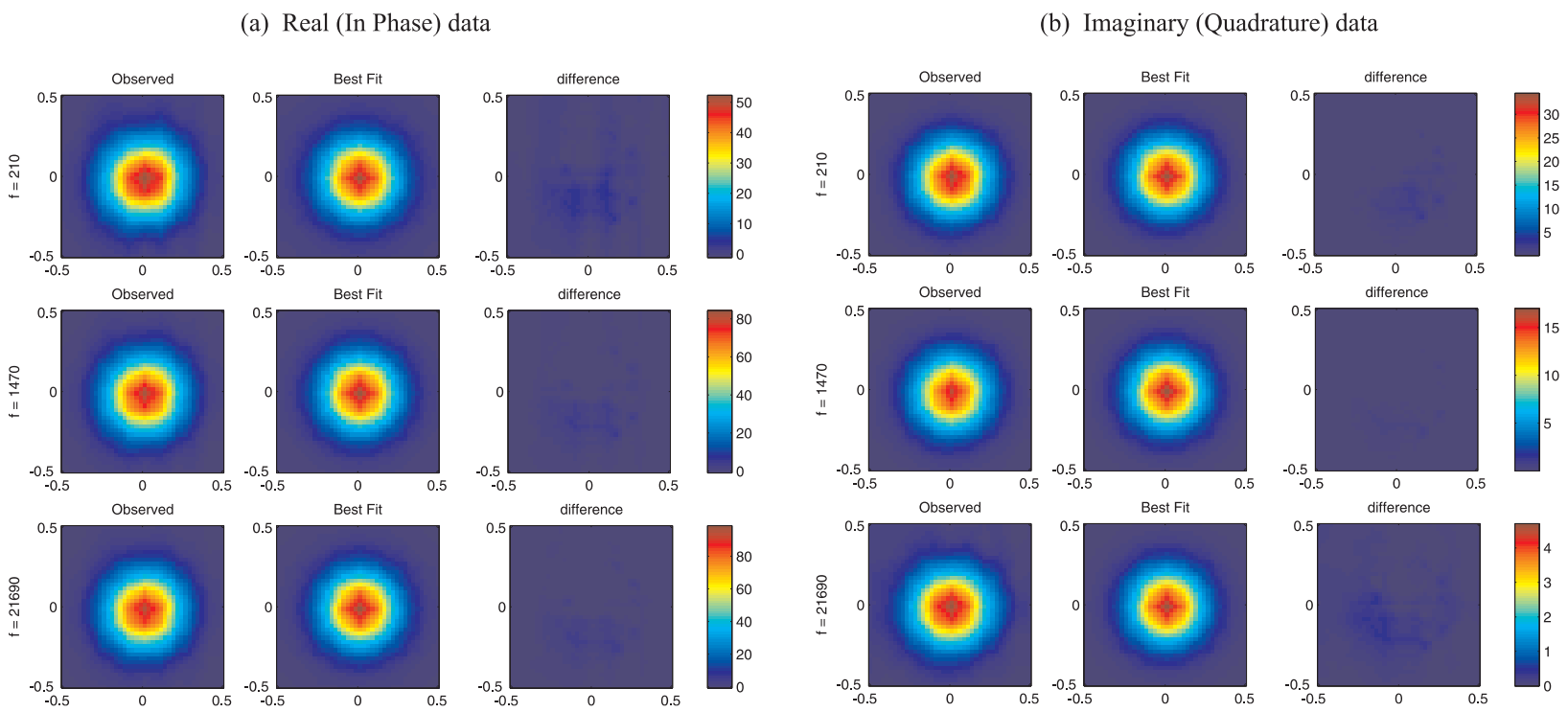

Figure 2.20: Modeled and measured GEM3 response for a vertically oriented ATC 40 mm (C3).

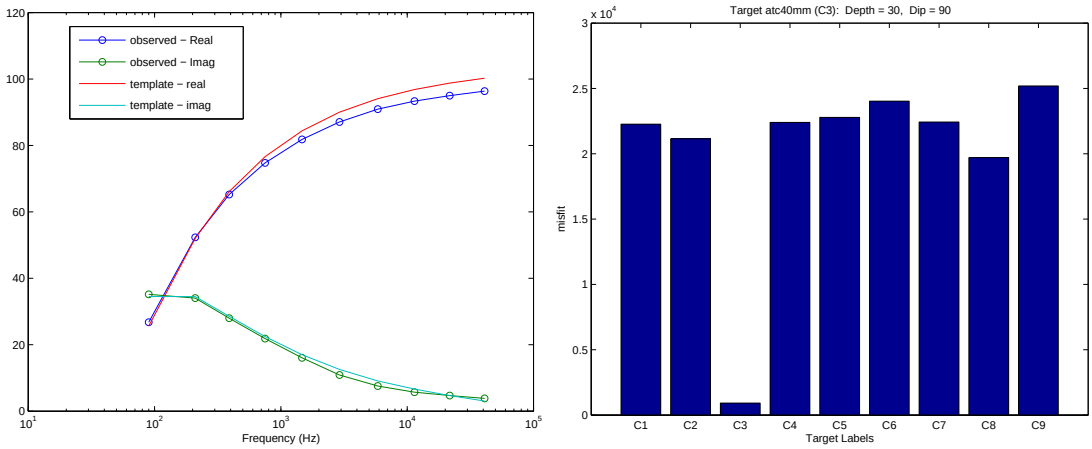

(a) Sounding

(b) Misfit for all the targets

Figure 2.21: Template example for C3.

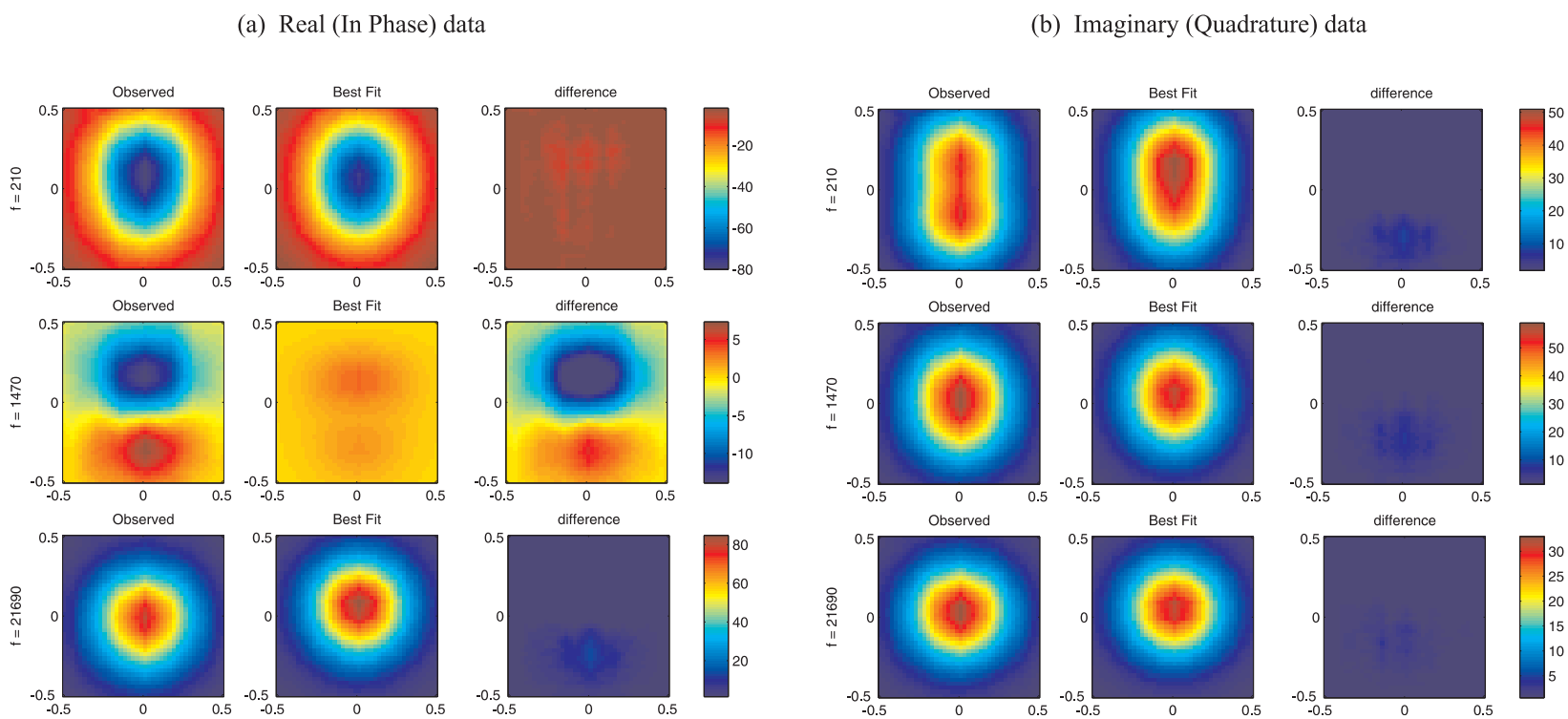

Figure 2.22: Modeled and measured GEM3 response for a horizontally oriented ATC 81 mm (C8).

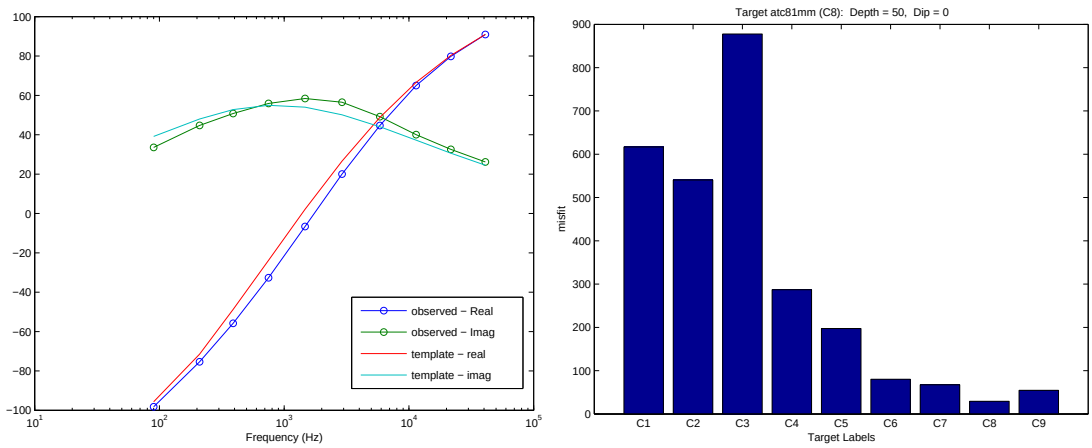

(a) Sounding

(b) Misfit for all the targets

Figure 2.23: Template example for C8.

2.8 Inversion for Optimal Orientation and Location of an Object

The above identification tests were conducted assuming an object location and orientation as *a priori* information. When such information is unavailable such as in a usual discrimination scenario, we need to estimate them from sensor measurements. This section reports such a preliminary test to invert the optimal location and orientation of a known object by using a gradient-type method.

Denote the parameter vector $\mathbf{m} = (\mathbf{r}_c, \alpha, \theta)$, where $\mathbf{r}_c$ denotes the position vector of an object center, α and θ are the azimuthal and polar angles of the object relative to the user coordinate. Based on the Eq. (2.4) of the secondary magnetic field, we can derive the analytical expression for the sensitivities of $\mathbf{H}_{sc}$ to the 5 parameters. For this nonlinear inverse problem, a optimization approach is implemented iteratively to correct the model parameters via minimizing the objective functional

$$F(\mathbf{r}_c, \alpha, \theta) = ||\mathbf{H}_{\mathrm{sc}}^{\mathrm{pre}}(\mathbf{r}_c, \alpha, \theta) - \mathbf{H}_{\mathrm{sc}}^{\mathrm{obs}}||^2, \tag{2.15}$$

where $\mathbf{H}_{\mathrm{sc}}^{\mathrm{pre}}$ are the predicted fields at a trial model, $\mathbf{H}_{\mathrm{sc}}^{\mathrm{obs}}$ are the observed ones.

The cylinder in section 4 is chosen as an object, being positioned at $(0, 0, -42.5)$ cm and oriented at $\theta = \pi/4$ and $\alpha = \pi/4$. For this inversion, the 7×7 simulated GEM-3 measurement points are distributed on a plane grid with the interval of 20 cm and a single frequency of 41010 Hz is used in the inversion. In the inversion test, we put the lower and upper bound vectors $\mathbf{m}_l = [-30\ \mathrm{cm}\ -30\ \mathrm{cm} - 70\ \mathrm{cm}\ 0\ 0]$ and $\mathbf{m}_u = [30\ \mathrm{cm}\ 30\ \mathrm{cm} - 30\ \mathrm{cm}\ 2\pi\ \pi]$. Fig. 2.24 (a) - (f) illustrates the convergence of the inverted results versus the iteration number. It is observed that the after 10 iterations, the model parameters are recovered very well. The values of data misfit monotonically decrease with the iteration and have no significant variations after 10 iterations, as shown in Fig. 2.24 (f).

In another test, the cylinder takes the same position as before but oriented at $\theta = 0^0$ and $\alpha = 0^0$. Fig. 2.25 shows inverted results that are fairly good. The convergence behavior in Fig. 2.25 (f) is similar to that of the previous test. Note that the recovered value of θ finally approaches to π not 0 because both values have no difference for a homogeneous cylinder. In this case the value of the azimuthal angle α could be arbitrary as the object is oriented vertically.

2.9 Conclusions

We have investigated the MAS/TSA-based implementation of the standardized (spheroidal) excitation approach for a full 3D electromagnetic induction sensing of metallic objects. The approach, by decomposing excitation fields into fundamental spheroidal modes, synthesizes the secondary fields through a linear superposition of each modal response to a target. We quantitatively studied the fundamental issue of determining the effective spheroids in decomposition. It was found that for a non-uniform primary field excited by a GEM3-like loop, the infinite

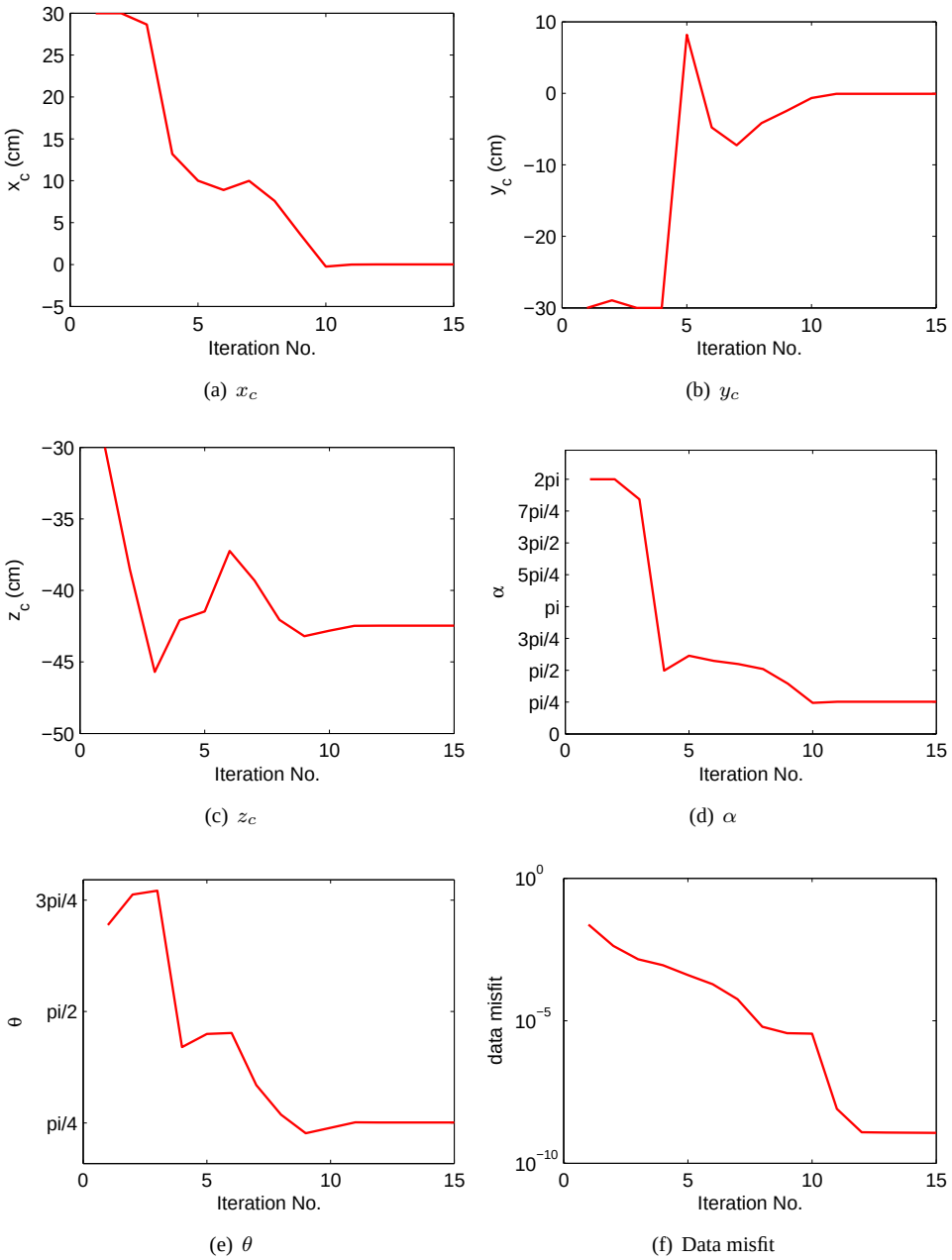

(a) x_c (b) y_c

(c) z_c (d) α

(e) θ (f) Data misfit

Figure 2.24: Inversion test I. Recovered model parameters versus iteration number.

series can be truncated at the maximum mode number $(M, N) = (3, 8)$, which is used to accurately represent the fields for various orientations of small/medium objects in a near field zone.

The key feature in this approach is that the extrinsic and intrinsic attributes characterizing the pattern of secondary fields are automatically separated out in the spheroidal mode expansion coefficients and the modal response amplitudes or the RSS, respectively. Based on the RSS for interested objects, the related full 3D EMI modeling can be carried out rapidly by merely determining primary field expansion coefficients for any excitation-object geometry. These were illustrated by the tests against the experimental data in both frequency-domain (GEM-3) and time-domain (EM63) systems. We extended the existing SEA to simulate a transient EM response by developing a convolution algorithm that applies to an arbitrary current waveform used in a TEM system. These experiment-based results are important not only to confirm the soundness of the approach but also indicate

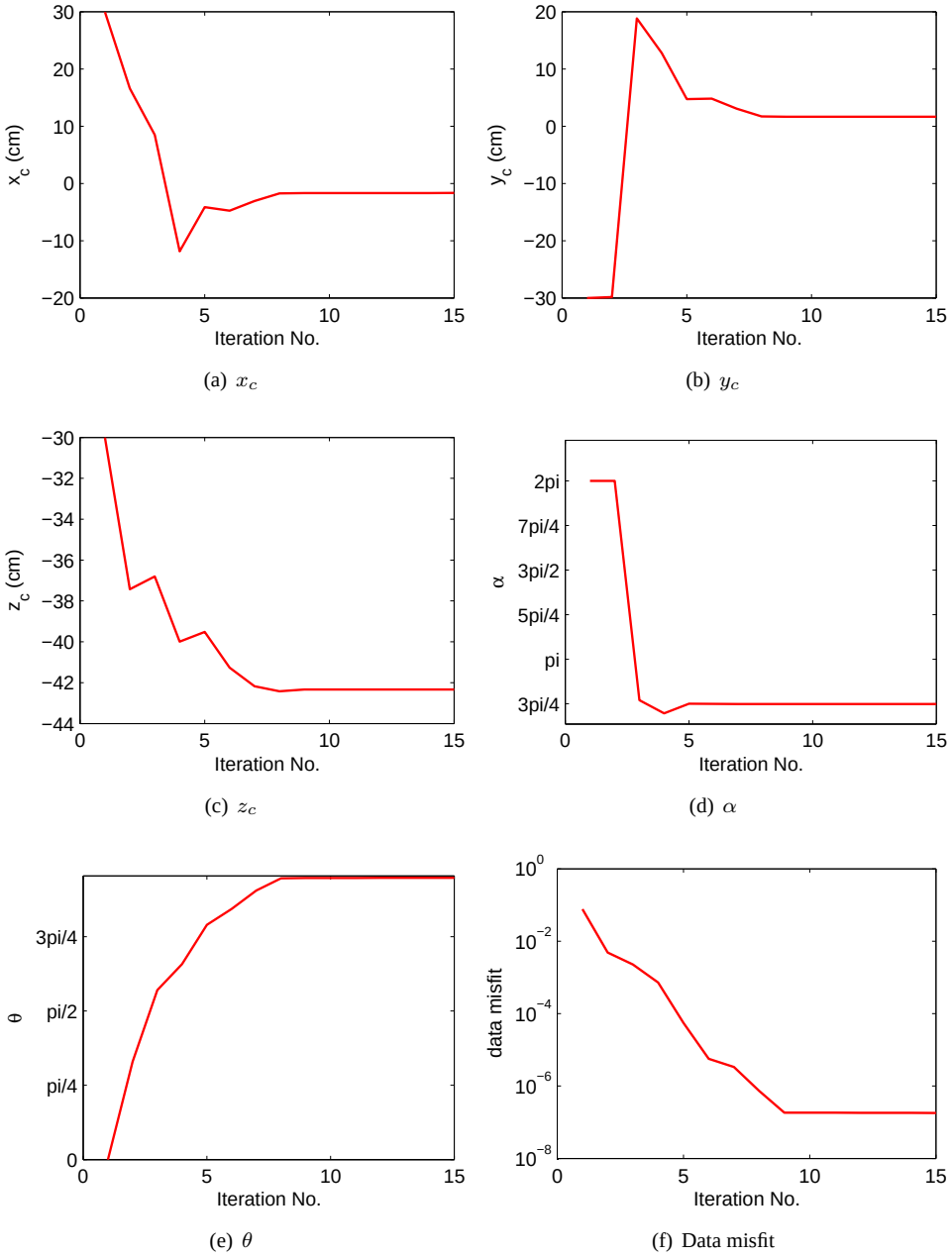

(a) x_c (b) y_c

(c) z_c (d) α

(e) θ (f) Data misfit

Figure 2.25: Inversion test II. Recovered model parameters versus iteration number.

its promise in real-world applications.

Since the MAS/TSA-based SEA is a physically complete numerical technique, as stated previously, it can be used to accurately build up a RSS-library in an ultra wide band - ranging from resistive to inductive limit. With such an ultra wide band RSS-library, it is convenient to compute EMI response in either the time or frequency domain.

As another direct application of a RSS-library, we have conducted identification test of UXO based on the test stand data. In this test, we successfully showed that identifying a candidate UXO can be quickly done through a straightforward pattern matching procedure by inspecting a best misfit values below an error threshold. In our follow-up research we will proceed to do a blind test of the approach combined with the robust inversion algorithm determining an optimal object location and orientation.

To conclude, the MAS/TSA-based SEA is a promising full 3D EMI modeling technique that provides a platform on which to develop discrimination and identification algorithms.

Chapter 3

Regularization of the Surface Charge Model for the Inversion of Electromagnetic Data

3.1 Abstract

Detection of buried unexploded ordnance with electromagnetic sensors requires robust predictive models to correctly interpret data recorded at the surface. Shubitidze et al. (2005a) have recently suggested a physics-based representation of the scattered electromagnetic field using surface magnetic charges. One such representation is the Normalized Surface Magnetic Charge (NSMC) model, which idealizes a compact metallic target with magnetic charges distributed on a spheroidal surface that encloses the target. The Total Normalized Magnetic Charge (TNMC), as a function of frequency or as a function of time, can be used to identify the object. At a theoretical level, however, the inference of the TNMC, is an ill-determined problem. Some form of regularization of the problem is required. In order to help develop the NSMC model into a robust practical tool for UXO discrimination, we conducted a theoretical study on the behavior of these magnetic surface charges and formulated the calculation of the total normalized charge as an inverse problem. Extensive use was made of Geophex GEM3 and Geonics EM63 test stand data collected at the USACE-ERDC test stand in Vicksburg, MS. Results are presented for both test stand data and data collected on the Sky Research UXO Test Site in Ashland, Oregon.

3.2 Introduction

In this chapter we consider the Surface Magnetic Charge (SMC) model of Shubitidze et al. (2005a). The SMC model approximates a target's secondary electromagnetic field at each frequency or time with the field from a magnetic charge distribution on a fictitious surface that encloses the target (Figure 3.1). Shubitidze et al. (2005a) claims that normalizing the charge distribution by the normal component of the primary field produces a surface distribution that is a property of the target, and not the excitation of the target. Furthermore, the surface integral of the normalized charge distribution was suggested as a discriminant for UXO.

Unlike the SEA model of the previous chapter, the nature of SMC and its computational speed make it a candidate for data inversion for the charge distribution. In this work, we study some of the properties of the magnetic charge model and some of the properties of the SMC inverse problem. The objective of this work was to determine if a stable discriminant derived from the surface magnetic charge model could be determined.

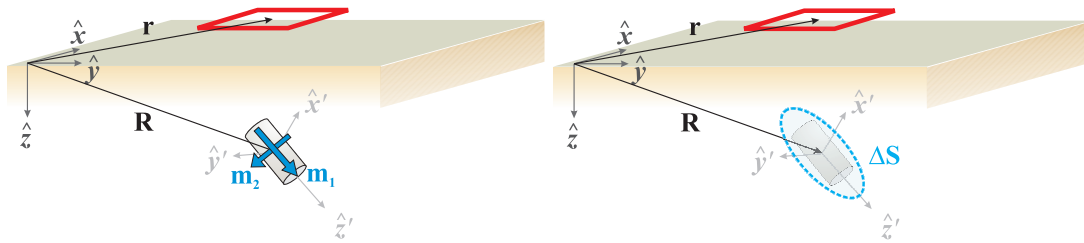

(a) The dipole model, showing axial and transverse polarizations

(b) The Surface Magnetic Charge (SMC) model

Figure 3.1: Representation of the response of a target using (a) a dipole and (b) a surface magnetic charge.

3.3 Model description and implementation

3.3.1 The Surface Magnetic Charge Model

The following description of the SMC model follows Shubitidze et al. (2005a). They assume a highly conducting, magnetically permeable, heterogeneous metallic target buried in soil where conductivity is low enough to be considered as free space. In a quasi-magneto-static regime, displacement currents are negligible, conduction currents are weak outside the target, the magnetic field is irrotational and can be written as the gradient of a scalar potential ψ:

$$\mathbf{H}^{sc}(\mathbf{r},\xi) = -\nabla\Psi^{sc}(\mathbf{r},\xi) \tag{3.1}$$

where the variable ξ can represent either time t or frequency ω. Assuming Gauss' Law for magnetic field yields

$$\nabla \cdot \mu_o \mathbf{H} = \nabla^2 \Psi^{sc} = \rho_m \tag{3.2}$$

where ρ_m represents a fictitious volumetric magnetic charge density that produces a scattered field outside a metallic body. The scalar potential satisfies an equation of the type

$$\Psi^{sc}(\mathbf{r},\xi) = \frac{1}{4\pi\mu_o}\int_V \rho_m(\mathbf{r}',\xi)\frac{1}{|\mathbf{r}-\mathbf{r}'|}dV' \tag{3.3}$$

where r is the observation point, r' the source point, V the volume of the scatterer, μ_0 the magnetic permeability of free space. Assuming surface charges σ_m only, the magnetic field is given by

$$\mathbf{H}^{sc}(\mathbf{r},\xi) = \frac{1}{4\pi\mu_o}\int_S \sigma_m(\mathbf{r}',\xi)\frac{\mathbf{r}-\mathbf{r}'}{|\mathbf{r}-\mathbf{r}'|^3}dS' \tag{3.4}$$

The charge distribution σ_m is a function of the field at the surface S which is, in turn, a function of the target properties and primary field.

The surface charge is assumed to be proportional to the normal component of the incident primary magnetic field:

$$\sigma_m(\mathbf{r}',\xi) = q_m(\mathbf{r}',\xi)\left[\mathbf{H}^{pr}(\mathbf{r}')\cdot\hat{\mathbf{n}}(\mathbf{r}')\right] \tag{3.5}$$

where q_m is the NSMC density that we try to calculate. Considering that UXO are bodies of revolution with symmetry along their main axis, Shubitidze et al. (2005b) assume that (1) the electromagnetic response of a UXO can be equivalently represented by surface charges located on a prolate spheroid enclosing the ordnance with same main axis, and (2) that q_m on this spheroid is uniform on rings perpendicular to the main axis. The TNMC of an object at a given time or frequency is defined as

$$Q(\xi) \equiv \int_S q_m(\mathbf{r}',\xi)\, dS' \tag{3.6}$$

Shubitidze et al. (2005a) suggested that the TNMC is unique for each target so it can be used to discriminate between different targets.

3.3.2 Numerical Implementation of the SMC Model

For this report, we only consider fields measured by induction loop receivers. For a frequency domain system, the voltage induced in a receiver loop is

$$V(\omega) = i\omega n_R \Phi \tag{3.7}$$

where n_R is the number of turns in the receiver, Φ is the flux through the receiver. The corresponding expression in the time domain is

$$V(t) = n_R \frac{\partial \Phi}{\partial t} \tag{3.8}$$

The flux through a receiver loop in air is

$$\Phi(\mathbf{r}, \xi) = \mu_o \int_{S^R} \left(\mathbf{H}^{\mathrm{sc}}(\xi) \cdot \mathbf{n}^R \right) dS^R \tag{3.9}$$

where $\mathbf{n}^R$ is the normal of the loop surface, and we again define ξ as being either t or ω. Assuming a horizontal loop:

$$\begin{aligned} \Phi(\mathbf{r}, \xi) &= \int_{S^R} \left(\int_S \frac{1}{4\pi} \frac{(z - z')}{|\mathbf{r} - \mathbf{r}'|^3} \; q(\mathbf{r}', \xi) \left[\mathbf{H}^P \cdot \hat{\mathbf{n}}(\mathbf{r}') \right] dS' \right) dS^R \\ &= \frac{1}{4\pi} \int_{S'} I(\mathbf{r}, \mathbf{r}') (z - z') \, q(\mathbf{r}', \xi) \left[\mathbf{H}^P \cdot \hat{\mathbf{n}}(\mathbf{r}') \right] dS' \end{aligned} \tag{3.10}$$

where

$$I(\mathbf{r}, \mathbf{r}') = \int_{S^R} \frac{1}{|\mathbf{r} - \mathbf{r}'|^3} \, dS^R \tag{3.11}$$

depends on the shape of the loop. We solve this integral analytically for a horizontal, rectangular loop. For a horizontal circular loop, we solve the integral in polar coordinates, with an analytic integration over the radial coordinate, and a numerical integration over the azimuthal coordinate.

Equation 3.10 shows that, once the charge surface is determined, the flux Φ, and therefore the induced voltage V is a linear function of the charge distribution q. To numerically solve the SMC integral, we discretize the surface S into N sub-surfaces, with area ΔS_i, and assume that the amplitude of the surface magnetic charge q_i is constant in Δs_i. Substitution in Equation 3.10 yields

$$\Phi(\mathbf{r}, \xi) = \frac{1}{4\pi} \sum_k^N I(\mathbf{r}, \mathbf{r}_k) (z - z_k) \, q(\mathbf{r}_k, \xi) \left[\mathbf{H}^P(\mathbf{r}_k) \cdot \hat{\mathbf{n}}(\mathbf{r}_k) \right] \Delta S_k \tag{3.12}$$

The forward model data collected at N stations at a frequency ω_i can be written as

$$\mathbf{Z} \;\; \mathbf{m} = \mathbf{d} \tag{3.13}$$

where

$$[\mathbf{Z}]_{mn} = \frac{1}{4\pi} I(\mathbf{r}_m, \mathbf{r}_n) (z_m - z_n) \left[\mathbf{H}^P(\mathbf{r}_n) \cdot \hat{\mathbf{n}}(\mathbf{r}_n) \right] \Delta S_n \tag{3.14}$$

$$\mathbf{m} = \left[q(\mathbf{r}_1, \omega_i) \;,\; q(\mathbf{r}_2, \omega_i) \;,\; \ldots \;,\; q(\mathbf{r}_N, \omega_i) \right]^T \tag{3.15}$$

and an element of the data vector $\mathbf{d}$ is the integrated secondary field flux over the receiver loop.

For time domain data,

$$\mathbf{m} = \left[\frac{\partial q(\mathbf{r}_1, t_i)}{\partial t} \;,\; \frac{\partial q(\mathbf{r}_1, t_i)}{\partial t} \;,\; \ldots \;,\; \frac{\partial q(\mathbf{r}_1, t_i)}{\partial t} \right]^T \tag{3.16}$$

$$\mathbf{d} = \left[V(\mathbf{r}_1, t_i) \;,\; V(\mathbf{r}_2, t_i) \;,\; \ldots \;,\; V(\mathbf{r}_N, t_i) \right]^T . \tag{3.17}$$

The modeling matrix $\mathbf{Z}$ is a function of the shape of the charge surface. For a spheroid that contains the axi-symmetric target, $\mathbf{Z}$ is then a function of the location and orientation. In the case of a sphere $\mathbf{Z}$ is a function of position only.

3.3.3 Discretization of the charge surface

In order to solve for a representative charge distribution, a surface must be defined and discretized. In this study we chose spherical and spheroidal surfaces to enclose axi-symmetric targets. Figure 3.2 illustrates a discretization on a spheroid. Patches are defined by uniformly discretizing in the azimuthal coordinate (longitude) and in the local axial (z) coordinate (or in the latitude angle). Rings are defined by assuming that the surface charge density remains an invariant of the azimuth.

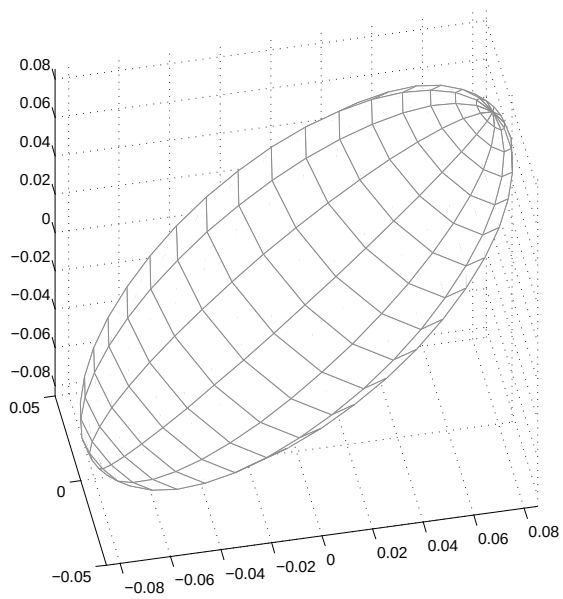

Figure 3.2: An example of discretizing a spheroid.

Discretization along longitudinal and latitudinal directions samples the surface of a spheroid in a non-uniform manner, resulting in high density of surface patches at the poles. To circumvent that potential source of error we tested the SMC method on a sphere by using a geodesic discretization derived from refinements of an icosahedron (polyhedron with 12 vertices, 20 triangular surfaces of equal area, 30 edges), illustrated in Figure 3.3, where red lines show the projection of the original icosahedron onto its surrounding sphere. This configuration is almost isotropic and every patch has the exact same dimensions, thus avoiding any area-induced bias in the charge density.

3.4 Inverting for a Surface Charge Distribution

In order for the SMC formulation to be part of a successful discrimination algorithm, the recovered surface magnetic charge model (or some property of the SMC) must be a function of the target characteristics only, and independent of the survey parameters. We studied the sensitivity of the SMC solution to different modeling parameters such as depth, orientation and noise by using test stand data and synthetic data obtained with a dipole

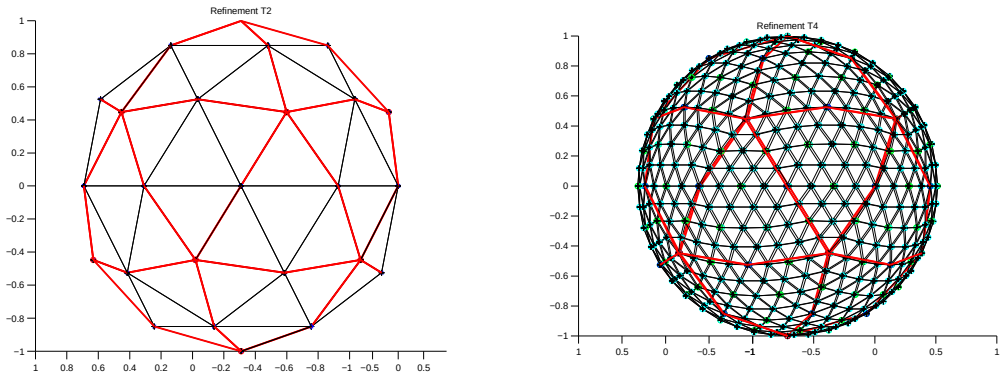

(a) 80 faces

(b) 1280 faces

Figure 3.3: Discretization of a sphere derived from an icosahedron

model. We find that for the type of objects of interest, and for the type of data that are collected, the problem of solving the equation $\mathbf{Zm} = \mathbf{d}$ is often ill-posed, even in over-determined cases where there are more data than parameters, as is the situation with the SMC method of rings. In the more general under-determined case, where patches cover the spheroid, there are more parameters than data and the inverse problem is severely ill-posed. Thus there are infinitely many solutions for the matrix system and some additional information needs to be incorporated to solve the problem. The instability of the inverse problem, and the non-uniqueness of solution, is exemplified by the condition number of $\mathbf{Z}$, $cond\,(\mathbf{Z})$, the ratio of the largest and smallest non-zero singular values of $\mathbf{Z}$. The condition number grows rapidly with the resolution of the model, for instance with 10 rings $cond\,(\mathbf{Z}) = 10^8$, with 40 rings $cond\,(\mathbf{Z}) = 10^{17}$ and with 200 patches $cond\,(\mathbf{Z}) = 10^{13}$.

We obtained a least squares solution to the matrix equation by using the pinv command in Matlab, which computes the Moore-Penrose pseudo-inverse of a matrix, effectively solving $\mathbf{Z}^T\mathbf{Zm} = \mathbf{Z}^T\mathbf{d}$ and performing a truncated singular value decomposition of $\mathbf{Z}^T\mathbf{Z}$. The level of truncation was chosen such that singular values less than the floating point precision of MatLab were omitted. Figure 3.4 contains the results of fitting a single channel of TEM data (Geonics EM-63 sensor) recorded on a test stand over a 40 mm projectile using both the patch model (Figure 3.4(a)) and the ring model (Figure 3.4(b)). The projectile was oriented at a 45 degrees dip and its center located 60 cm below the sensor. Both models produce excellent fit to the data (as is indicated by correlation coefficients close to unity and small misfit). The model with patches fits the data particularly closely; misfits are five orders of magnitude less than the data. This exceptional fit raises the issue of over-fitting the data by fitting the noise. Although noise levels remain low within the well-controlled environment of the test stand, a close look at the low left panel of Figure 3.4(a) suggests the presence of noise. Indeed, the recorded anomaly exhibits more shape features than expected for a simple-geometry 40 mm projectile, a clear effect of noise adding high frequency variability to the observation. In Figure 3.4(b), discretizing the spheroid surface with rings of constant charge density predicts a smooth response (low center panel); this might be considered to be a better solution since it is simpler and does not have extreme structure. The choices of rings over patches and the number of rings are first steps toward a regularization of the surface charge model imposed by discretization. Shubitidze et al. (2005b) restricted the number of rings to 9. We tested the feasibility and effect of using more or less rings.

In Figure 3.4(b) the resulting distribution in rings remains characterized by extreme variations between positive and negative values that are several orders of magnitude greater than the magnitude of charge, especially for bottom rings. This also seems to create additional energy outside of the domain used for the inversion (see higher misfit in the lowest part of the low right panel of Figure 3.4(b)). Additional tests with both test stand and synthetic data show that solutions for charge distribution and total magnetic charge are sensitive to variations in target positioning and orientation, as well as data noise. Higher levels of regularization are therefore warranted for the use of either rings or patches.

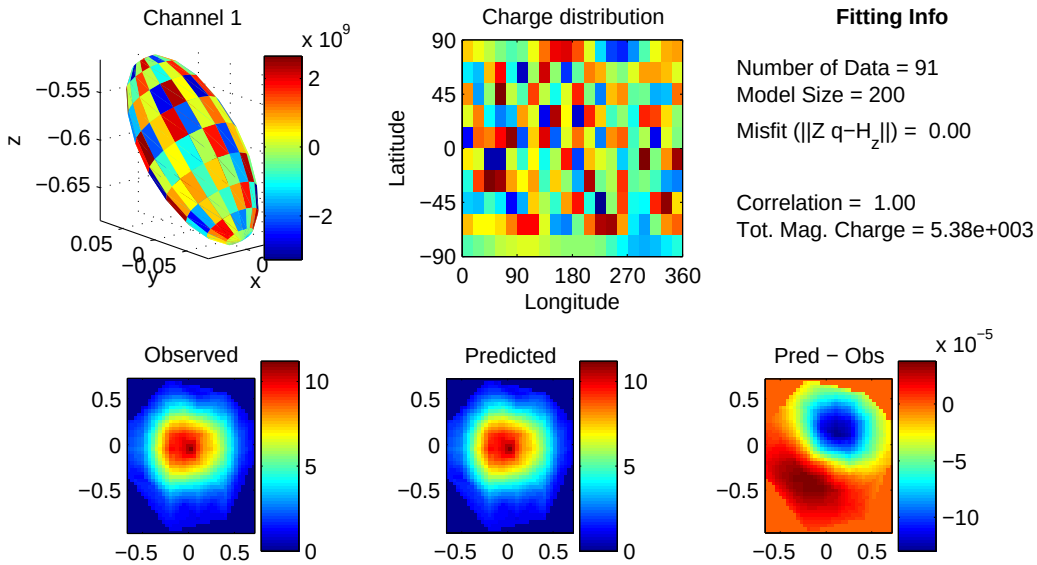

(a) Fitting noisy data with a charge density distribution on the surface of the spheroid.

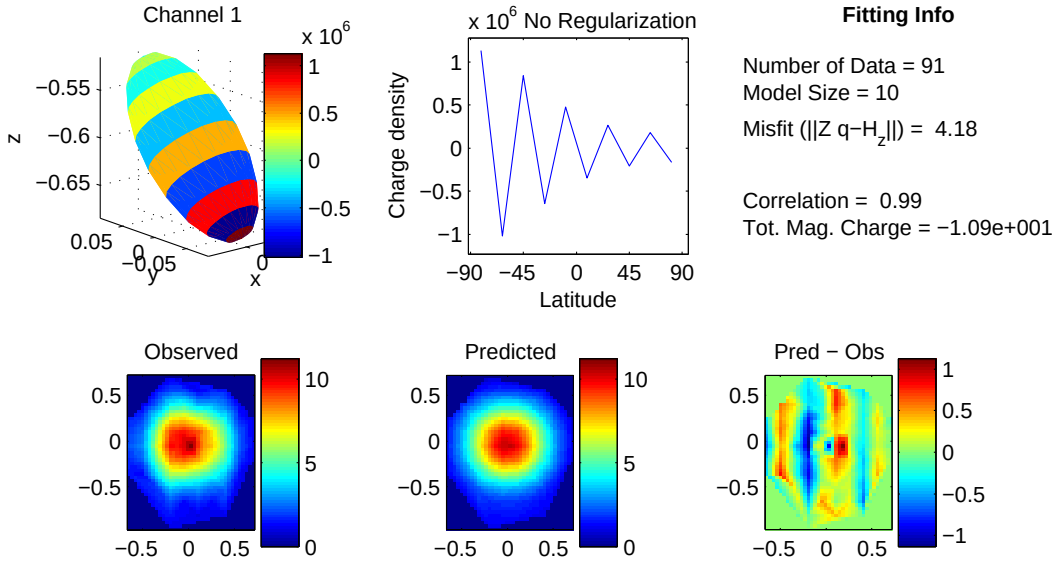

(b) Fitting the same noisy data as in (a) with a ring model. The ring model no longer over fits the data noise, resulting in a higher residual error.

Figure 3.4: 40 mm projectile (45 degrees inclination, 60 cm below sensor). Both solutions of charge distribution produce large oscillations.

Additional characteristics of the problem include:

1. As the number of model parameters (rings, patches, Fourier coefficients) increases, data are better fit but the amplitude variations in the charge density of adjacent patches or rings increases. Also, there is enhanced sensitivity due to the noise.

2. The total magnetic charge, the correlation coefficient and the misfit depend on the size and shape of the spheroid used in the calculation. For instance, large elongated items like a 105 mm High Explosive Anti Tank (HEAT) round would be better represented with a long spheroid. This suggests that a judicious choice of spheroid should be made before carrying on the inversion. Practically, this would imply that a predefined and limited (3-5) set of spheroids be chosen to test possible forward models. The spheroid should not be too small because this has a negative effect on the condition number of Z: physically, a smaller spheroid tries to accommodate all the features of the target, yielding large contrast among surface charges.

3.5 Properties of the Normalized Surface Magnetic Charge

The previous section showed that direct inversion of EM data does not allow recovering of a stable surface charge distribution and that a regularization of inversion is needed. In order to guide the regularization process with physical considerations, we now re-examine the assumption that surface magnetic charges can be normalized to produce a surface distribution that depends on the object only and is independent of excitation (relative position and orientation of object and illuminating field).

3.5.1 Field on a surface with charges

The field on the surface of a charge distribution can be calculated by integrating equation 3.2 by using a Gaussian pillbox on a charge surface (Figure 3.5). The integration over the volume gives

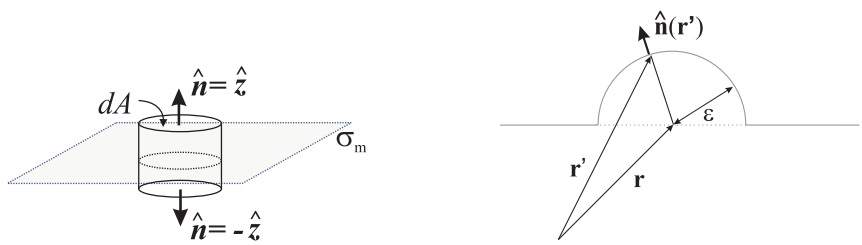

(a) Gaussian pill box on a charge distribtion σ_m.

(b) Integrating the singularity by distorting the charge surface with a semihemispherical surface.

Figure 3.5: Geometries for determining the field on a charge surface.

$$\int_V \nabla \cdot \mu_o \mathbf{H} dV = \int_V \sigma_m dV \tag{3.18}$$

The divergence theorem leads to surface integrals, and the following expression

$$\int_{top} \mu_o \mathbf{H} \cdot \hat{\mathbf{z}} dS - \int_{top} \mu_o \mathbf{H} \cdot \hat{\mathbf{z}} dS + \int_{side} \mu_o \mathbf{H} \cdot \hat{\rho} dS = \sigma_m dA \tag{3.19}$$

By symmetry, we can write

$$\mathbf{H} \cdot \hat{\mathbf{n}} = \frac{1}{2\mu_o} \sigma_m \tag{3.20}$$

Hence the charge distribution is proportional to the normal component of the field at the surface.

3.5.2 The normalized surface magnetic charge on a spherical surface for a dipole field

To understand the properties of the normalized surface magnetic charge, it is instructive to investigate the normalized charge distribution behavior for a dipolar field. The analytic solution for the secondary field of a sphere in a uniform field is a dipole. Consider a permeable and conducting sphere of radius a illuminated by a uniform primary field $\mathbf{H}^{\mathrm{P}}$. At a time $t = 0$ the primary field is terminated, and eddy currents are induced in the sphere; they subsequently decay because of the finite conductivity of the sphere. The secondary field $\mathbf{H}^{\mathrm{sc}}$ generated by the decaying currents is dipolar:

$$\mathbf{H}^{\mathrm{sc}}(t) = \frac{1}{4\pi r^3}\,\mathbf{m}(t)\cdot\left(3\hat{\mathbf{r}}\hat{\mathbf{r}} - \bar{\bar{\mathbf{I}}}\right) \tag{3.21}$$

where $\mathbf{m}(t)$ is the dipole moment induced at the center of the sphere at time t, r is the distance between the observation point and the sphere center, $\hat{\mathbf{r}}$ is the unit vector pointing from the sphere center to the observation point P, and $\bar{\bar{\mathbf{I}}}$ is the identity dyadic. The dipole moment is

$$\mathbf{m}(t) = \frac{2\pi}{\mu_o}\,\mathbf{H}^{\mathrm{P}}\,L(t) \tag{3.22}$$

where

$$L(t) = 6a^3\mu\sum_{s=1}^{\infty}\frac{\exp(-t/\tau)}{q_s^2 + (\mu_r - 1)(\mu_r + 2)} \tag{3.23}$$

with $\tau = \sigma\mu a^2/q_s^2$ (Kaufman and Keller, 1985). The values q_s are roots to the transcendental equation

$$\tan q_s = \frac{(\mu_r - 1)\,q_s}{q_s^2 + (\mu_r - 1)}. \tag{3.24}$$

Equation 3.21 reveals that the secondary field of a sphere in a uniform primary field is equivalent to the field of a single magnetic dipole located at the center of the sphere and oriented parallel to the primary field. The size and material properties (i.e. conductivity and magnetic permeability) are contained within the function $L(t)$. Now let us enclose the sphere with a spherical charge surface S that has a radius a_S (Figure 3.6(a)). On the surface S, the

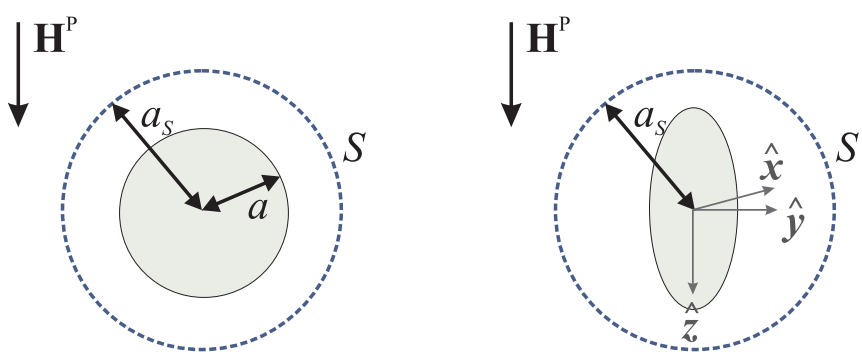

(a) Sphere example (b) Spheroid example

Figure 3.6: Sphere surface.

secondary field produced by the sphere will be

$$\begin{aligned}\mathbf{H}(t, \mathbf{r}\in S) &= \frac{1}{2\pi a_S^3}\mathbf{m}(t)\\ &= \frac{1}{\mu_o a_S^3}\mathbf{H}^{\mathrm{P}}L(t)\end{aligned} \tag{3.25}$$

The surface charge distribution can be expressed as a function of the primary field by taking the normal of $\mathbf{H}$ from equation 3.25, and substituting into equation 3.20

$$\begin{aligned}\sigma_m &= 2\mu_o \mathbf{H} \cdot \hat{\mathbf{n}} \\ &= 2\frac{1}{a_S^3} L(t) \left[\mathbf{H}^{\mathrm{P}} \cdot \hat{\mathbf{n}}\right]\end{aligned} \tag{3.26}$$

The NSMC is then

$$q_m = 2\frac{1}{a_S^3} L(t) \tag{3.27}$$

and, from equation 3.6, the TNMC is the surface integral of q_m on S

$$Q = \frac{8\pi}{a_S} L(t) \tag{3.28}$$

Equation 3.28 shows that, for the case of a sphere in a uniform field, the NSMC is uniform on the surface S. The normalized magnetic charge is proportional to $L(t)$ and, therefore, the normalized charge for a sphere is a measure of the size and material properties of the sphere. However, the total normalized magnetic charge is inversely proportional to a_S and is thus dependent on how we choose our charge surface S.

The above calculations demonstrate that, for a fixed a_S, the TNMC is a reasonable discriminant for modeling spheres. This is due to the geometry of the problem which causes the induced dipole to be parallel to the primary field. Let us consider a non-spherical target whose response is generated by charges on a spherical surface (for example, Figure 3.6(b)). The field of an compact metallic target, can be approximated by a dipole model. We can write the induced dipole as

$$\mathbf{m} = \mathbf{M} \cdot \mathbf{H}^{\mathrm{P}} \tag{3.29}$$

where, following the coordinate system of Figure 3.6(b),

$$\mathbf{M} = \frac{2\pi}{\mu_o} \begin{bmatrix} L_x(t) & 0 & 0 \\ 0 & L_y(t) & 0 \\ 0 & 0 & L_z(t) \end{bmatrix} \tag{3.30}$$

For a sphere $L(t) = L_x(t) = L_y(t) = L_z(t)$. The charge distribution for the dipole model can be written as

$$\begin{aligned}\sigma_m &= 2\mu_o \mathbf{H} \cdot \hat{\mathbf{n}} \\ &= \frac{\mu_o}{\pi a_S^3} \left[\mathbf{M} \cdot \mathbf{H}^{\mathrm{P}}\right] \cdot \hat{\mathbf{n}}\end{aligned} \tag{3.31}$$

and the NSMC is

$$q_m = \frac{\mu_o}{\pi a_S^3} \frac{\left[\mathbf{M} \cdot \mathbf{H}^{\mathrm{P}}\right] \cdot \hat{\mathbf{n}}}{\mathbf{H}^{\mathrm{P}} \cdot \hat{\mathbf{n}}} \tag{3.32}$$

It is clear from Equations 3.31 and 3.32 that charge distribution σ_m and normalized charge distribution q_m is dependent on the direction of excitation $\mathbf{H}^{\mathrm{P}}$ and the size of the charge surface. For example, for a unit vertical primary field $\mathbf{H}^{\mathrm{P}} = \hat{\mathbf{z}}$ the normalized charge distribution will be uniform:

$$q_m = \frac{2}{a_S^3} L_z(t) \tag{3.33}$$

with a total normalized charge of

$$Q = \frac{8\pi}{a_S} L_z(t) \tag{3.34}$$

If the primary field is $\mathbf{H}^{\mathrm{P}} = (\hat{\mathbf{x}} + \hat{\mathbf{y}}) / \sqrt{2}$, then the normalized charge distribution will vary along the azimuthal direction $0 < \lambda < 2\pi$:

$$q_m(\lambda) = \frac{2}{a_S^3} \left[\frac{L_x(t)\cos(\lambda) + L_y(t)\sin(\lambda)}{\cos(\lambda) + \sin(\lambda)} \right] \tag{3.35}$$

The TNMC is then

$$Q = \frac{4\pi}{a_S} \left[L_x(t) + L_y(t) \right] \tag{3.36}$$

Clearly, (1) the TNMC is dependent on the radius of the spherical charge surface, and (2) the TNMC is dependent on the direction of the primary field that illuminates the target.

3.5.3 Investigating the normalized magnetic charge using the Method of Moments

In order to study the normalized magnetic charge on a spheroidal surface, we will solve the modeling integral equations with the MoM.

Define integral equation

Let's determine the field on the surface S. There is a singularity, therefore we use a principle value integral and explicitly calculate the contribution of the singularity.

$$\mathbf{H}^s(\mathbf{r}) = \lim_{\epsilon \to 0} \frac{1}{4\pi\mu_o} \int_{S - S_\epsilon} \frac{\mathbf{r} - \mathbf{r}'}{|\mathbf{r} - \mathbf{r}'|^3} \, \sigma_m(\mathbf{r}') \, dS' + \lim_{\epsilon \to 0} \frac{1}{4\pi\mu_o} \int_{S_\epsilon} \frac{\mathbf{r} - \mathbf{r}'}{|\mathbf{r} - \mathbf{r}'|^3} \, \sigma_m(\mathbf{r}) \, dS' \tag{3.37}$$

where S_ϵ is the hemisphere in Figure 3.5(b). The singularity as $\mathbf{r} \to \mathbf{r}'$ is integrable, and can be determined by using the geometry of Figure 3.5(b) and letting $\epsilon \to 0$. The value of the field at the surface is

$$\begin{aligned} \mathbf{H}^s(\mathbf{r}) &= \lim_{\epsilon \to 0} \frac{1}{4\pi\mu_o} \int_{S_\epsilon} \frac{\mathbf{r} - \mathbf{r}'}{|\mathbf{r} - \mathbf{r}'|^3} \, \sigma_m(\mathbf{r}') \, dS' \\ &= \lim_{\epsilon \to 0} \frac{1}{4\pi\mu_o} \int_{S_\epsilon} \frac{\epsilon \mathbf{n}}{\epsilon^3} \, \sigma_m(\mathbf{r}') \, dS' \\ &\frac{1}{2\mu_o} \mathbf{n}(\mathbf{r}) \, \sigma_m(\mathbf{r}) \end{aligned} \tag{3.38}$$

Therefore, the field is

$$\mathbf{H}^s(\mathbf{r}) = \lim_{\epsilon \to 0} \frac{1}{4\pi\mu_o} \int_{S - S_\epsilon} \frac{\mathbf{r} - \mathbf{r}'}{|\mathbf{r} - \mathbf{r}'|^3} \, \sigma(\mathbf{r}') \, dS' + \frac{1}{2\mu_o} \mathbf{n}(\mathbf{r}) \, \sigma_m(\mathbf{r}) \tag{3.39}$$

where $\mathbf{r} \in S$. We want to match the normal components of the magnetic flux $\mathbf{B}$ at the surface:

$$\mathbf{n}(\mathbf{r}) \cdot \mathbf{B}^s = \frac{1}{4\pi} \int_S^{P.V.} \frac{\mathbf{n}(\mathbf{r}) \cdot (\mathbf{r} - \mathbf{r}')}{|\mathbf{r} - \mathbf{r}'|^3} \, \sigma_m(\mathbf{r}') \, dS' + \frac{1}{2} \, \sigma_m(\mathbf{r}) \tag{3.40}$$

The equations for the normalized surface magnetic charge are then

$$\mathbf{n}(\mathbf{r}) \cdot \mathbf{B}^s = \frac{1}{4\pi} \int_S^{P.V.} \frac{\mathbf{n}(\mathbf{r}) \cdot (\mathbf{r} - \mathbf{r}')}{|\mathbf{r} - \mathbf{r}'|^3} q_m(\mathbf{r}') \left[\mathbf{H}^P(\mathbf{r}') \cdot \mathbf{n}(\mathbf{r}') \right] \, dS' + \frac{1}{2} q_m(\mathbf{r}) \left[\mathbf{H}^P(\mathbf{r}) \cdot \mathbf{n}(\mathbf{r}) \right] \tag{3.41}$$

Define Basis for q_m

The first step to solving for q_m is to partition the surface into N patches of area ΔS_n. We assume pulse basis functions to represent q_m:

$$q_m(\mathbf{r}) = \sum_{n=1}^{N} a_n f_n \tag{3.42}$$

where

$$f_n = \begin{cases} 1 & \text{for } r \in \Delta S_n \\ 0 & \text{otherwise} \end{cases} \tag{3.43}$$

Substitution gives

$$\mathbf{n}(\mathbf{r}) \cdot \mathbf{B}^s \approx \frac{1}{4\pi} \int_S^{P.V.} \frac{\mathbf{n}(\mathbf{r}) \cdot (\mathbf{r} - \mathbf{r}')}{|\mathbf{r} - \mathbf{r}'|^3} \left[\sum_{n=1}^{N} a_n f_n(\mathbf{r}') \right] \left[\mathbf{H}^P(\mathbf{r}') \cdot \mathbf{n}(\mathbf{r}') \right] \, dS' + \frac{1}{2} \left[\sum_{n=1}^{N} a_n f_n(\mathbf{r}) \right] \left[\mathbf{H}^P(\mathbf{r}) \cdot \mathbf{n}(\mathbf{r}) \right] \tag{3.44}$$

Since we have pulse basis functions, we can approximate the integral as

$$\int_S = \sum_{n=1}^{N} \int_{S_n} \tag{3.45}$$

which gives

$$\mathbf{n}(\mathbf{r}) \cdot \mathbf{B}^s \approx \frac{1}{4\pi} \sum_{n=1}^{N} \int_{\Delta S_n}^{P.V.} \frac{\mathbf{n}(\mathbf{r}) \cdot (\mathbf{r} - \mathbf{r}')}{|\mathbf{r} - \mathbf{r}'|^3} \left[\sum_{k=1}^{N} a_k f_k(\mathbf{r}') \right] \left[\mathbf{H}^P(\mathbf{r}') \cdot \mathbf{n}(\mathbf{r}') \right] \, dS' + \frac{1}{2} \left[\sum_{n=1}^{N} a_n f_n(\mathbf{r}) \right] \left[\mathbf{H}^P(\mathbf{r}) \cdot \mathbf{n}(\mathbf{r}) \right] \tag{3.46}$$

Note that we changed indices for the pulse basis, in the the first term on the right hand side. Now, $f_k(\mathbf{r}')$ will act like a delta function, i.e. the integral will be zero unless $k = n$. Therefore, we rewrite the integral as

$$\mathbf{n}(\mathbf{r}) \cdot \mathbf{B}^s \approx \frac{1}{4\pi} \sum_{n=1}^{N} \int_{\Delta S_n}^{P.V.} \frac{\mathbf{n}(\mathbf{r}) \cdot (\mathbf{r} - \mathbf{r}')}{|\mathbf{r} - \mathbf{r}'|^3} a_n \left[\mathbf{H}^P(\mathbf{r}') \cdot \mathbf{n}(\mathbf{r}') \right] \, dS' + \frac{1}{2} \left[\sum_{n=1}^{N} a_n f_n(\mathbf{r}) \right] \left[\mathbf{H}^P(\mathbf{r}) \cdot \mathbf{n}(\mathbf{r}) \right] \tag{3.47}$$

Defining weighting functions

By defining a basis function for q_m, Equation 3.47 represents an approximation to the linear operator defined in 3.41. If we define the exact integral equation as $\mathbf{L} q_m = \mathbf{g}$, then we have a non zero residual

$$\mathbf{R} = \mathbf{L}\tilde{q_m} - \mathbf{g} = \mathbf{L} \left(\sum_{n=1}^{N} a_n f_n \right) - \mathbf{g} = \left(\sum_{n=1}^{N} a_n \mathbf{L} f_n \right) - \mathbf{g} \tag{3.48}$$

Weighting functions W_m are used to make the residual zero at a finite number of points, i.e.,

$$\int \langle W_m, \mathbf{R} \rangle \tag{3.49}$$

$$\sum_{n=1}^{N} a_n \langle W_m, \mathbf{L} \rangle = \langle W_m, \mathbf{g} \rangle \tag{3.50}$$

This defines a new linear system to solve for the basis coefficients a_n

$$\mathbf{G}\ \mathbf{a} = \mathbf{h} \tag{3.51}$$

We choose point matching weighting functions

$$W_m = \delta\left(\mathbf{r} - \mathbf{r}_m\right) \qquad \text{where } m = 1, .., N \tag{3.52}$$

and define an inner product

$$\langle f, h \rangle = \int_S f\left(\mathbf{r}'\right) h\left(\mathbf{r}'\right) dS' \tag{3.53}$$

Applying to the first term, gives

$$\begin{aligned} &\langle W_m, \text{1st term} \rangle = \\ &\int_S \delta\left(\mathbf{r} - \mathbf{r}_m\right) \left[\frac{1}{4\pi} \sum_{n=1}^{N} a_n \int_{\Delta S_n}^{P.V.} \frac{\mathbf{n}\left(\mathbf{r}\right) \cdot \left(\mathbf{r} - \mathbf{r}'\right)}{\left|\mathbf{r} - \mathbf{r}'\right|^3} \left[\mathbf{H}^P\left(\mathbf{r}'\right) \cdot \mathbf{n}\left(\mathbf{r}'\right)\right]\ dS' \right] dS \\ &= \frac{1}{4\pi} \sum_{n=1}^{N} a_n \int_{\Delta S_n}^{P.V.} \frac{\mathbf{n}\left(\mathbf{r}_m\right) \cdot \left(\mathbf{r}_m - \mathbf{r}'\right)}{\left|\mathbf{r}_m - \mathbf{r}'\right|^3} \left[\mathbf{H}^P\left(\mathbf{r}'\right) \cdot \mathbf{n}\left(\mathbf{r}'\right)\right]\ dS' \end{aligned} \tag{3.54}$$

Applying the weighting to the second term, gives

$$\begin{aligned} \langle W_m, \text{2nd term} \rangle &= \int_S \delta\left(\mathbf{r} - \mathbf{r}_m\right) \left[\frac{1}{2} \sum_{n=1}^{N} a_n f_n\left(\mathbf{r}\right) \left[\mathbf{H}^P\left(\mathbf{r}\right) \cdot \mathbf{n}\left(\mathbf{r}\right)\right] \right] dS \\ &= \frac{1}{2} \sum_{n=1}^{N} a_n f_n\left(\mathbf{r}_m\right) \left[\mathbf{H}^P\left(\mathbf{r}_m\right) \cdot \mathbf{n}\left(\mathbf{r}_m\right)\right] \\ &= \frac{1}{2} \delta_{mn} \left[\mathbf{H}^P\left(\mathbf{r}_m\right) \cdot \mathbf{n}\left(\mathbf{r}_m\right)\right] \end{aligned} \tag{3.55}$$

We now have the elements of $\mathbf{G}$:

$$G_{mn} = \frac{1}{4\pi} \int_{\Delta S_n}^{P.V.} \frac{\mathbf{n}\left(\mathbf{r}_m\right) \cdot \left(\mathbf{r}_m - \mathbf{r}'\right)}{\left|\mathbf{r}_m - \mathbf{r}'\right|^3} \left[\mathbf{H}^P\left(\mathbf{r}'\right) \cdot \mathbf{n}\left(\mathbf{r}'\right)\right]\ dS' + \frac{1}{2} \delta_{mn} \left[\mathbf{H}^P\left(\mathbf{r}_m\right) \cdot \mathbf{n}\left(\mathbf{r}_m\right)\right] \tag{3.56}$$

The surface integration in each patch ΔS is approximated by assuming that all values are constant within each patch ΔS_n

$$\begin{aligned} G_{mn} = \frac{1}{4\pi} \frac{\mathbf{n}\left(\mathbf{r}_m\right) \cdot \left(\mathbf{r}_m - \mathbf{r}_n\right)}{\left|\mathbf{r}_m - \mathbf{r}_n\right|^3} \left[\mathbf{H}^P\left(\mathbf{r}_n\right) \cdot \mathbf{n}\left(\mathbf{r}_n\right)\right] \Delta S_n \left(1 - \delta_{mn}\right) + \\ \frac{1}{2} \delta_{mn} \left[\mathbf{H}^P\left(\mathbf{r}_m\right) \cdot \mathbf{n}\left(\mathbf{r}_m\right)\right] \end{aligned} \tag{3.57}$$

which can be rewritten as

$$G_{mn} \begin{cases} \dfrac{1}{4\pi} \dfrac{\mathbf{n}\left(\mathbf{r}_m\right) \cdot \left(\mathbf{r}_m - \mathbf{r}_n\right)}{\left|\mathbf{r}_m - \mathbf{r}_n\right|^3} \left[\mathbf{H}^P\left(\mathbf{r}_n\right) \cdot \mathbf{n}\left(\mathbf{r}_n\right)\right] \Delta S_n & \text{if } m \neq n \\ \dfrac{1}{2} \left[\mathbf{H}^P\left(\mathbf{r}_m\right) \cdot \mathbf{n}\left(\mathbf{r}_m\right)\right] & \text{if } m = n \end{cases} \tag{3.58}$$

Now for the right hand side.

$$\begin{aligned} h_m = \langle W_m, \mathbf{n}\left(\mathbf{r}\right) \cdot \mathbf{B}^s\left(\mathbf{r}\right) \rangle &= \int_S \delta\left[\left(\mathbf{r} - \mathbf{r}_m\right) \mathbf{n}\left(\mathbf{r}\right) \cdot \mathbf{B}^s\left(\mathbf{r}\right)\right] dS \\ &= \mathbf{n}\left(\mathbf{r}_m\right) \cdot \mathbf{B}^s\left(\mathbf{r}_m\right) \end{aligned} \tag{3.59}$$

Examples of Method of Moments modeling

We apply the MoM modeling to the problem geometry of Figure 3.7. The field of the target is represented by a dipole.

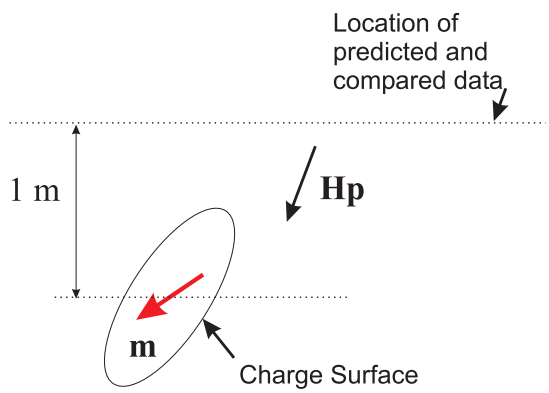

Figure 3.7: Geometry of example. We match boundary conditions on a surface and compare the data predicted by the charge distribution on the surface with the data predicted by a dipole model.

For this test we will use the method of moments to determine the charge distribution σ_m and the normalized charge distribution q_m on a surface that encloses the dipole. A separate matrix equation is solved for σ_m and q_m, i.e., we do not solve for the q_m (or σ_m) charge distribution and multiply (or divide) by the normal component of the primary field to obtain σ_m (or q_m). We will assume that the primary field $\mathbf{H}^{\mathrm{P}}$ is uniform. The field predicted by the charges obtained by method of moments and the field predicted by the dipole are compared on a surface 1 m above the dipole location.

Example 1: Solution on a spherical surface The first example is for a sphere in a uniform field. As was outlined in the Section 3.5.2, the dipole moment is due to a sphere and is, therefore, parallel to the primary field. For this example, we will try and use a spherical charge surface. The charge surface is discretized uniformly in azimuth (ϕ) and dip (η) angles.

Figure 3.8(a) plots the recovered un-normalized (σ_m) and normalized (q_m) charge distributions in the case where the primary field is vertical. The radius of the charge surface is 0.15 m. As predicted by the analysis in the previous section, the normalized charge is essentially uniform. The un-normalized charge is symmetric about $z = 0$, and is consistent with a vertical magnetic dipole. The field predicted by both the normalized and un-normalized distributions are compared to the field predicted by a dipole at the center of the sphere. The forward modeled charge and dipole model match very well, indicating that the charge and dipole models are equivalent in this case. Table 3.1 summarizes our results for illuminating the sphere in different directions, and a couple of different coarseness levels of discretization. The total unnormalized magnetic charge is zero (to numerical precision), and the total normalized magnetic charge is similar in each case. This numerical result is consistent with the analytic result presented earlier: the total normalized magnetic charge is stable to illumination direction for targets with spherical symmetry.

Figure 3.9 has a band of normalized magnetic charge that is zero. This is due to the normal component of the horizontally-directed primary field being zero at this point. The corresponding elements in the MoM modeling matrix also go to zero at this point, making the determination of the normalized magnetic charge at those points poorly determined. The coarser discretization of Figure 3.12 does not have surface patches that have normal perpendicular to the primary field. Consequently, all the surface patches are well determined.

Primary Field	num ϕ	num η	L_1	L_2	total unnormalized magnetic charge	total normalized magnetic charge	Figure Number
Vertical	30	30	1	1	-4.3e-014	20.6	3.8
Horizontal	30	30	1	1	-6.2e-015	19.3	3.9
Vertical	20	20	1	1	-1.4e-013	20.91	3.10
45 degrees	20	20	1	1	-9.7e-014	20.88	3.11
Horizontal	20	20	1	1	-4.2e-016	20.88	3.12

Table 3.1: Magnetic charge results for the sphere tests.

Primary Field	num ϕ	num η	L_1	L_2	total unnormalized magnetic charge	total normalized magnetic charge	Figure Number
Vertical	21	21	4	1	-8.9e-014	364.07	3.13
45 degrees	21	21	4	1	-6.1e-014	1052.86	3.14
Horizontal	21	21	4	1	-9.1e-015	22.00	3.15

Table 3.2: Magnetic charge results for the spheroid tests.

Example 2: Solution on a spheroidal surface Our second example is to determine the charge distribution for an axi-symmetric target. The secondary field for the axi-symmetric target is modeled using a dipole field with $L_1 = 4$ and $L_2 = L_3 = 1$. For this example, we use a spheroidal charge surface. The spheroidal surface has a length of 40 cm and a width of 20 cm. The spheroidal surface is oriented with the major axis parallel to the $\hat{\mathbf{z}}$-axis for each of the examples of this section.

Figure 3.13(a) plots the recovered un-normalized (σ_m) and normalized (q_m) charge distributions in the case where the primary field is vertical. The un-normalized charge is symmetric about $z = 0$, and is consistent with a vertical magnetic dipole. The field predicted by both the normalized and un-normalized distributions are compared to the field predicted by the dipole at the center of the spheroid. The forward modeled charge and dipole model match very well, indicating that the charge and dipole models are equivalent in this case.

Table 3.2 summarizes our results for illuminating the spheroid in different directions. As was the case with the sphere examples, the total un-normalized magnetic charge is zero. In each case the charge distribution and dipole fields match on a plane 1 m away from the center of the spheroid. In this case, the total normalized magnetic charge is not independent of the primary field direction.

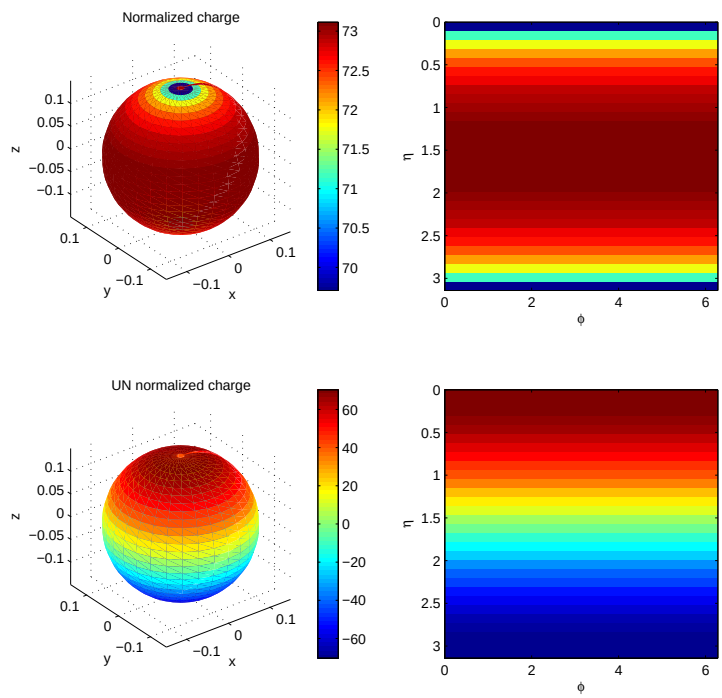

(a) Charge Distribution on a sphere. The top panel is the normalized surface magnetic charge distribution q_m. The bottom panel is the un-normalized surface magnetic charge distribution σ_m.

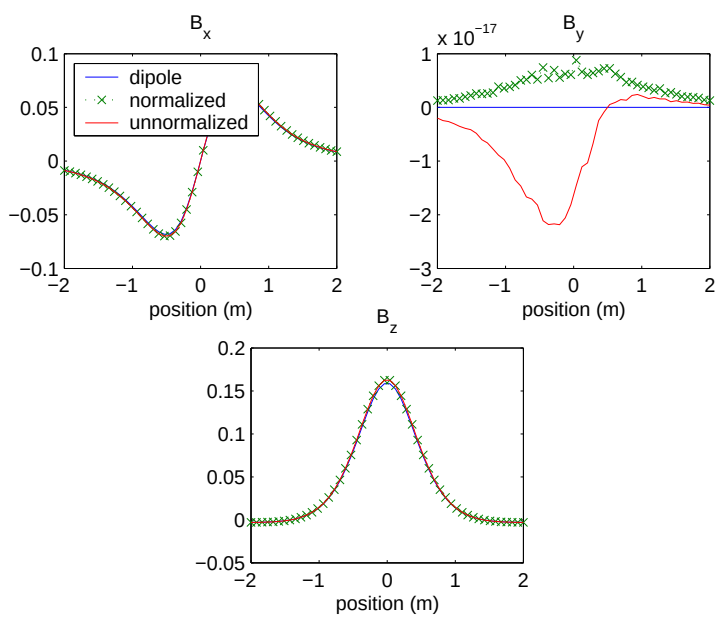

(b) Data modeled 1 m above the center of the sphere

Figure 3.8: Method of Moments solution for the surface magnetic charge distributions on a sphere with a vertical primary field excitation. The surface was discretized with 900 patches.

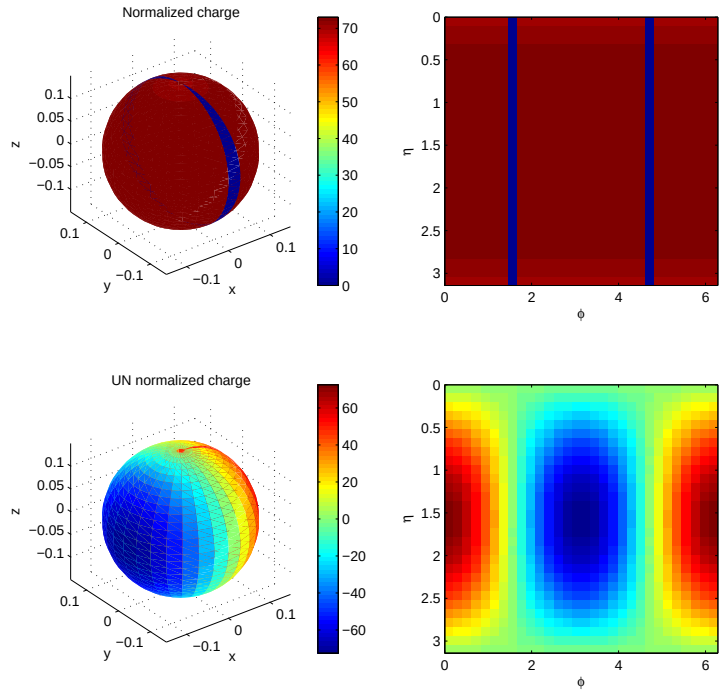

(a) Charge distribution. The top panel is the normalized surface magnetic charge distribution q_m. The bottom panel is the un-normalized surface magnetic charge distribution σ_m. The blue strips in the normalized charge distribution correspond to points where $\mathbf{H}^p \cdot \mathbf{n} = 0$

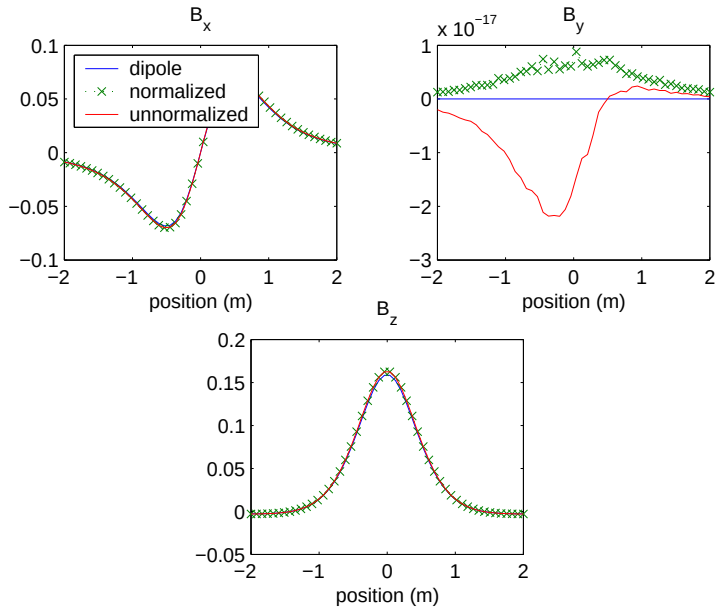

(b)

Figure 3.9: Method of Moments solution for the surface magnetic charge distributions on a sphere with a horizontal primary field excitation. The surface was discretized with 900 patches.

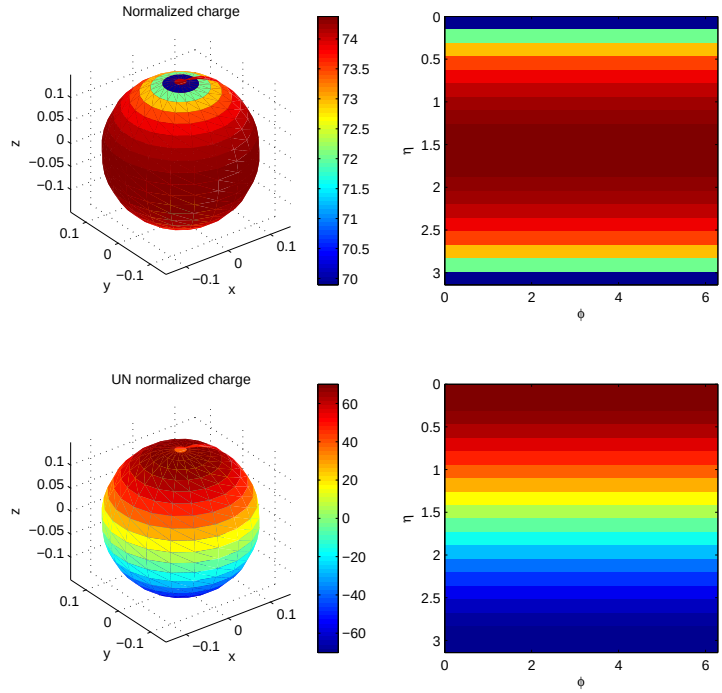

(a) Charge Distributions. The top panel is the normalized surface magnetic charge distribution q_m. The bottom panel is the un-normalized surface magnetic charge distribution σ_m.

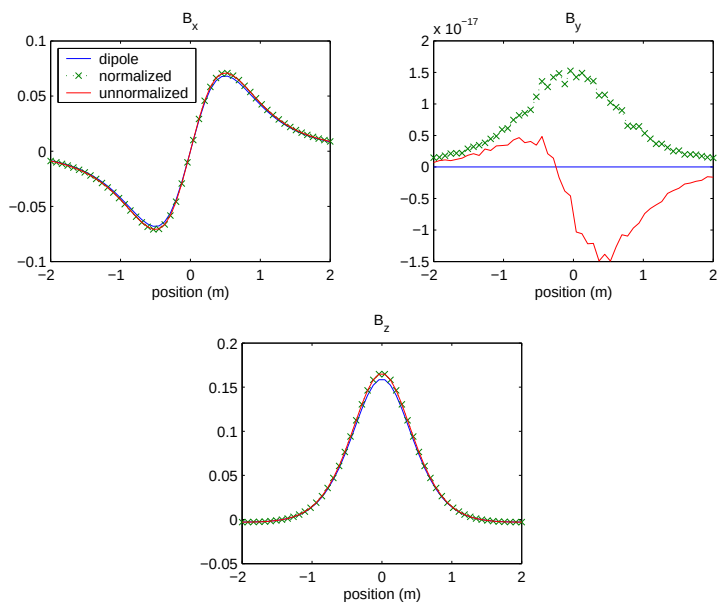

(b) Data modeled 1 m above the center of the sphere

Figure 3.10: Method of Moments solution for the surface magnetic charge distributions on a sphere with a vertical primary field excitation. The surface was discretized with 400 patches.

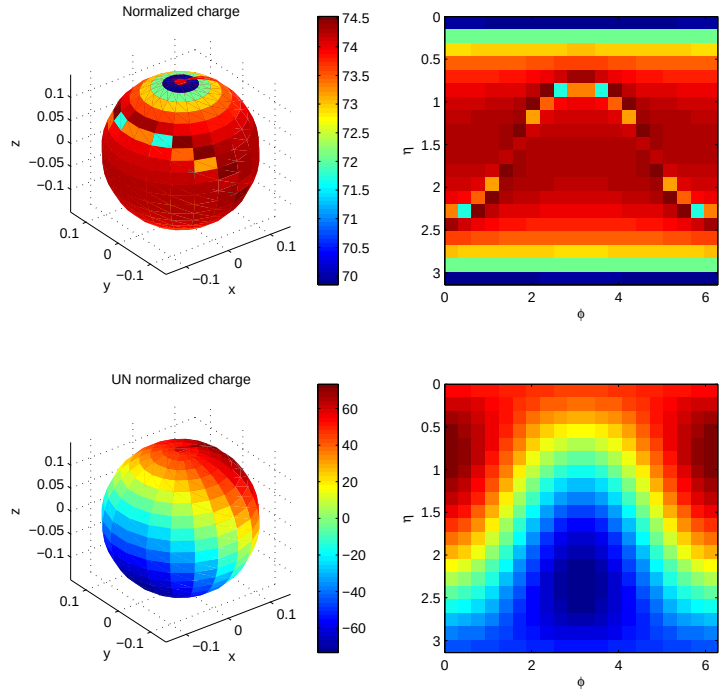

(a) Charge distribution. The top panel is the normalized surface magnetic charge distribution q_m. The bottom panel is the un-normalized surface magnetic charge distribution σ_m.

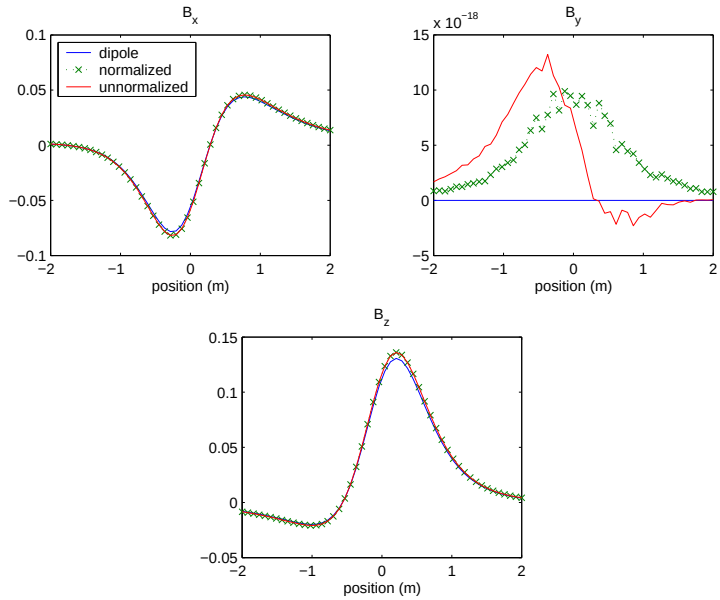

(b) Data modeled 1 m above the center of the sphere

Figure 3.11: Method of Moments solution for the surface magnetic charge distributions on a sphere with a primary field excitation at a 45 degree angle ($\mathbf{H}^P = (\hat{\mathbf{y}} + \hat{\mathbf{z}}) / \sqrt{2}$). The surface was discretized with 400 patches.

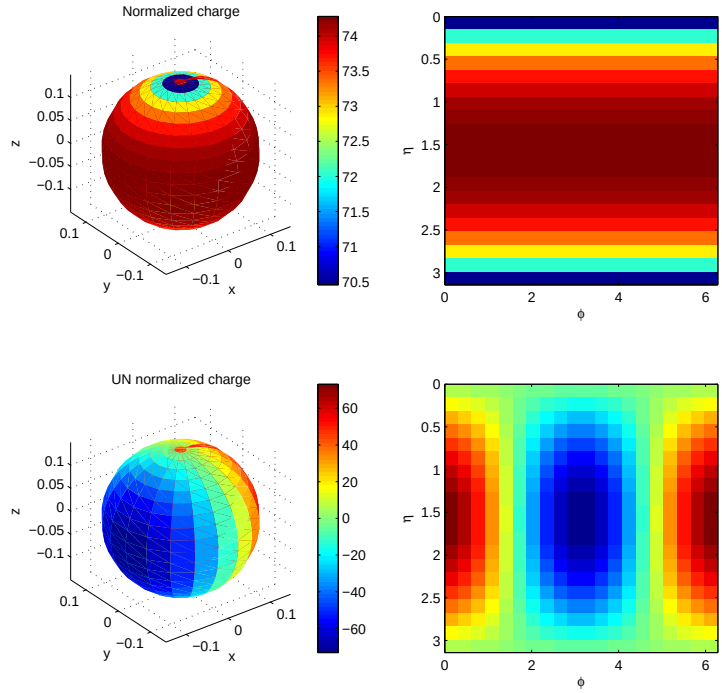

(a) Charge distribution. The top panel is the normalized surface magnetic charge distribution q_m. The bottom panel is the un-normalized surface magnetic charge distribution σ_m.

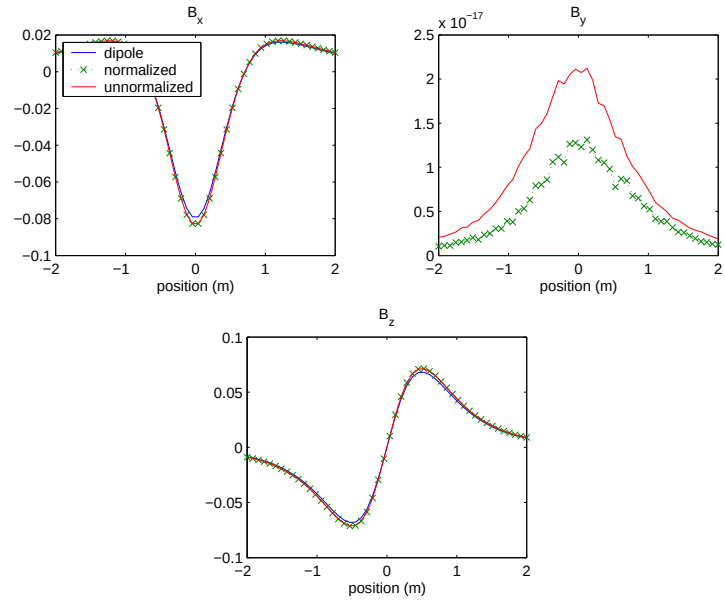

(b) Data modeled 1 m above the center of the sphere

Figure 3.12: Method of Moments solution for the surface magnetic charge distributions on a sphere with a horizontal primary field excitation. The surface was discretized with 400 patches.

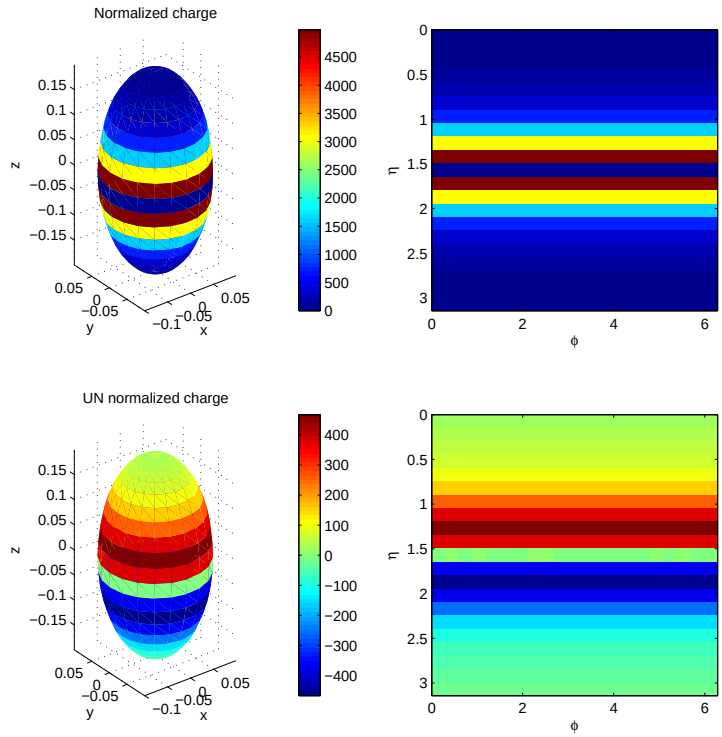

(a) Charge distribution. The top panel is the normalized surface magnetic charge distribution q_m. The bottom panel is the un-normalized surface magnetic charge distribution σ_m.

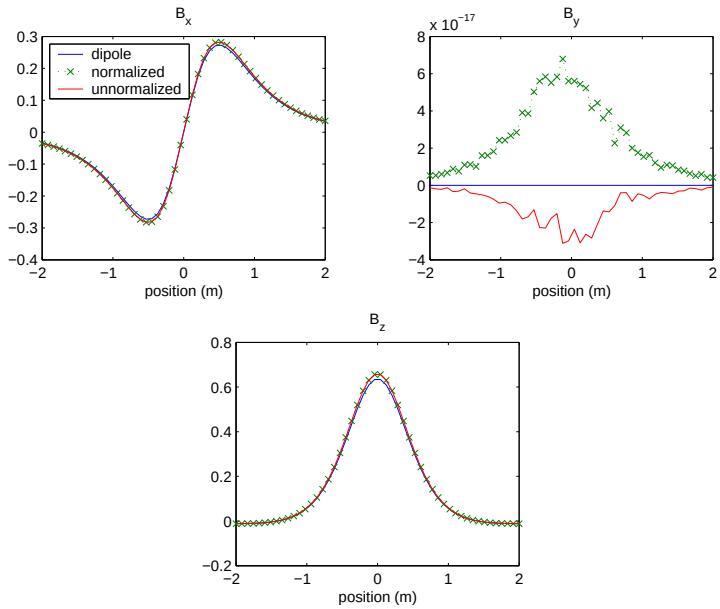

(b) Data modeled 1 m above the center of the spheroid

Figure 3.13: Method of Moments solution for the surface magnetic charge distributions on a spheroid with a vertical primary field excitation.

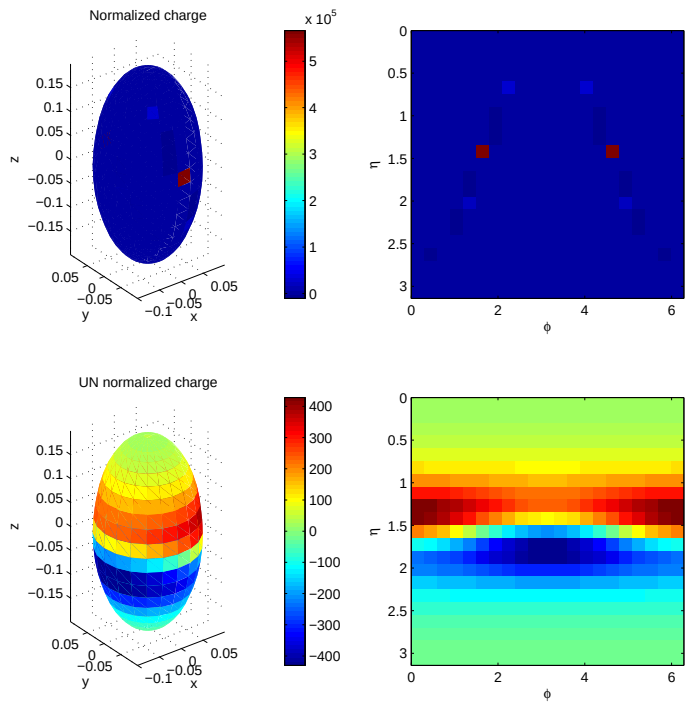

(a) Charge distribution. The top panel is the normalized surface magnetic charge distribution q_m. The bottom panel is the un-normalized surface magnetic charge distribution σ_m.

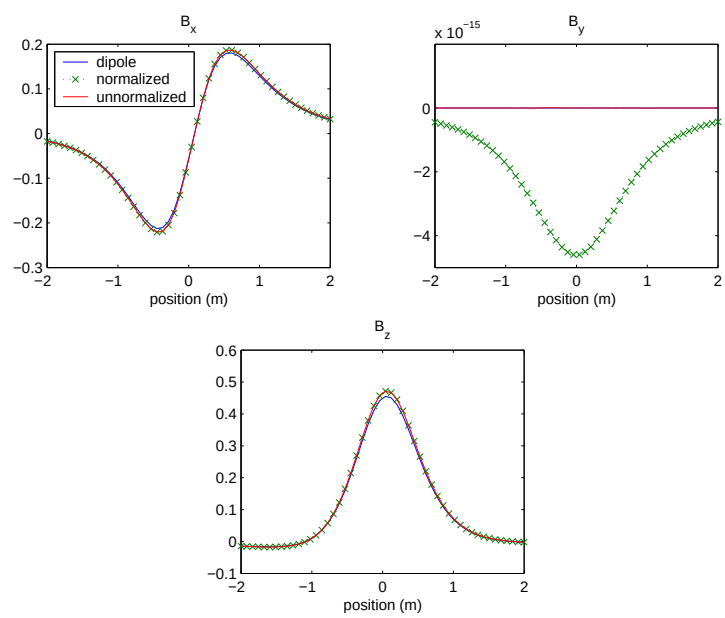

(b) Data modeled 1 m above the center of the spheroid

Figure 3.14: Method of Moments solution for the surface magnetic charge distributions on a spheroid with a primary field at a 45 degree angle ($\mathbf{H}^P = (\hat{\mathbf{y}} + \hat{\mathbf{z}})/\sqrt{2}$)..

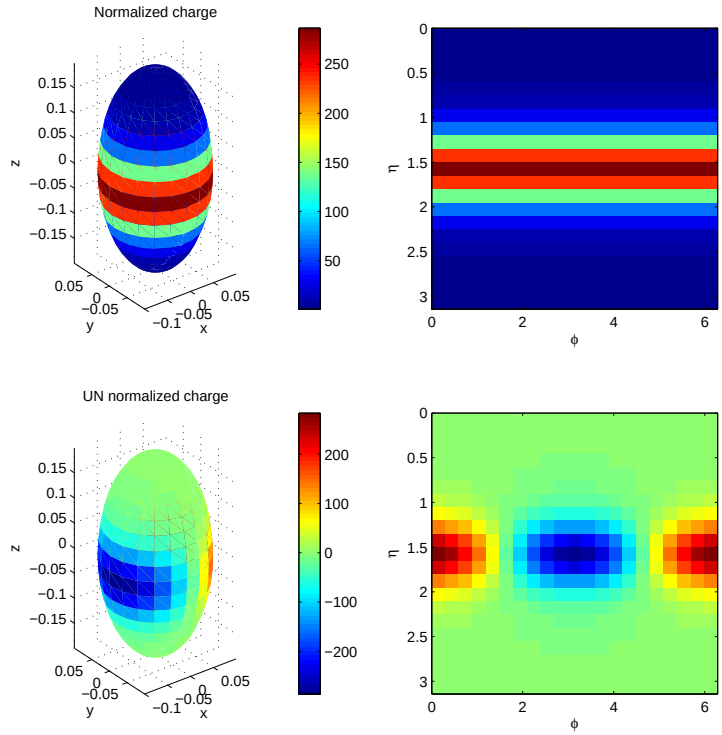

(a) Charge distribution. The top panel is the normalized surface magnetic charge distribution q_m. The bottom panel is the un-normalized surface magnetic charge distribution σ_m.

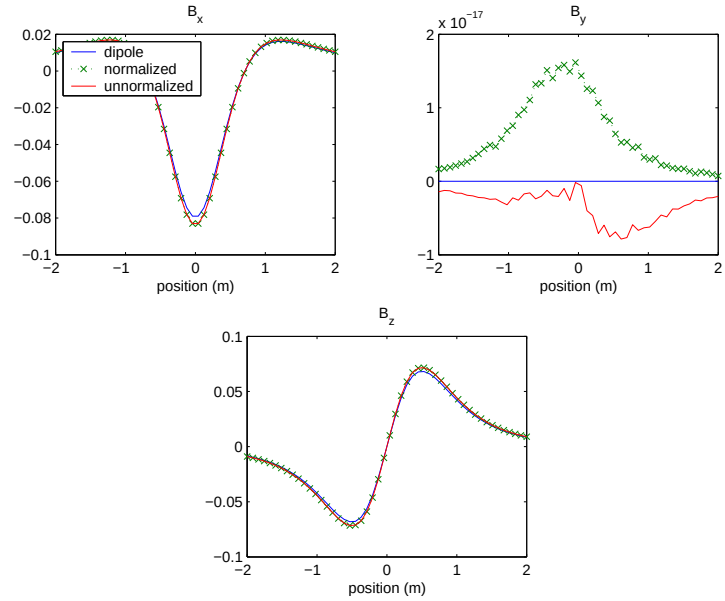

(b) Data modeled 1 m above the center of the spheroid

Figure 3.15: Method of Moments solution for the surface magnetic charge distributions on a spheroid with a horizontal primary field excitation.

3.5.4 Comparison to SEA modeled secondary fields

The previous section presented the distributions of surface charges

$$\sigma_m = 2\mu_0 \mathbf{H}^{\mathrm{sc}} \cdot \mathbf{n} \tag{3.60}$$

and normalized surface charges

$$q_m = \mu_0 \frac{\mathbf{H}^{\mathrm{sc}} \cdot \mathbf{n}}{\mathbf{H}^{\mathrm{p}} \cdot \mathbf{n}} \tag{3.61}$$

in the simplified case where the scattered field $\mathbf{H}^{\mathrm{sc}}$ could be represented by a dipole model and the primary field $\mathbf{H}^{\mathrm{p}}$ was uniform. Realistic conditions were tested for a cylinder for which the SEA library computed scattered fields at the surface of a spheroid enclosing the cylinder and with dimensions defined by the user. SEA was used after verification that the computation-intensive MAS and simplified SEA codes produced the exact same result. Realistic primary field was computed by modeling the effect of a frequency domain square transmitter of 1 x 1 m.

In the following, only the real part of the scattered field measured at the first frequency (0.1 mHz) is displayed, as later frequencies and the imaginary part exhibit similar trends. Each figure presents on a spheroid encapsulating the same cylinder the distribution of normal component of the scattered and primary fields, as well as the normalized charge taken as their direct ratio and that obtained by resolution through the method of moment. The effect of the sizes and shapes of the modeling spheroid (and sphere) and those of the relative orientations and positions of transmitter and target were tested.

Reference test

As a reference test presented in Figure 3.16 the cylinder is placed vertically directly below the transmitter at a 42.7 cm depth. The enclosing modeling spheroid has semi-axes of length 21 cm and 10 cm and a resolution of 40 points in latitude and 39 in longitude, with longitude ranging from 0 to 2π and latitude from 0 (North) to π (South). In each panel, quantities are shown on the spheroid by unwrapping its surface and using contours with a special contour in magenta to indicate zero crossings for normalized charge density. The vertical position exactly below the transmitter implies that all fields are longitudinally symmetric, contour lines therefore follow latitudes. In the two left panels of Figure 3.16 the normal component of the scattered and primary fields approach zero at different latitudes because the primary field is not uniform, their direct ratio therefore yields large values (infinite value if discretization allowed) in the upper central panel while MoM gives large but well defined values (right panels). Normalized charges computed by direct ratio or MoM show similar but different values, their integral over the surface of the spheroid, the TNMC differs by 30%.

Changes of orientation

The same cylinder and its spheroid are rotated into a horizontal position in Figure 3.17. Although distributions of normalized charges by field ratios and MoM appear qualitatively similar, with most of the spheroid covered with negative charges, differences in charge amplitude are such that their respective Total Magnetic Charge (TMC) obtained by numerical integration vary by a factor of two (with the resolution applied here). Comparison with the previous figure shows that rotation of the illuminating field by 90 ° stimulates a totally different charge distribution at the surface of the spheroid and TMC. Dependency on the illuminating field is further illustrated in Figure 3.18 with a rotation of 45 ° and yet another normalized charge distribution characterized by large regions of positive and negative charges and a different value for TMC.

Change of position

The transmitter was modeled at 30 cm to the left of the center of the cylinder and spheroid for the tests presented in Figures 3.19–3.21. For each case the normalized charge distribution and TMC, derived by direct ratio and MoM, show different patterns and values and confirm strong dependency on the relative position and orientation of transmitter and modeled target.

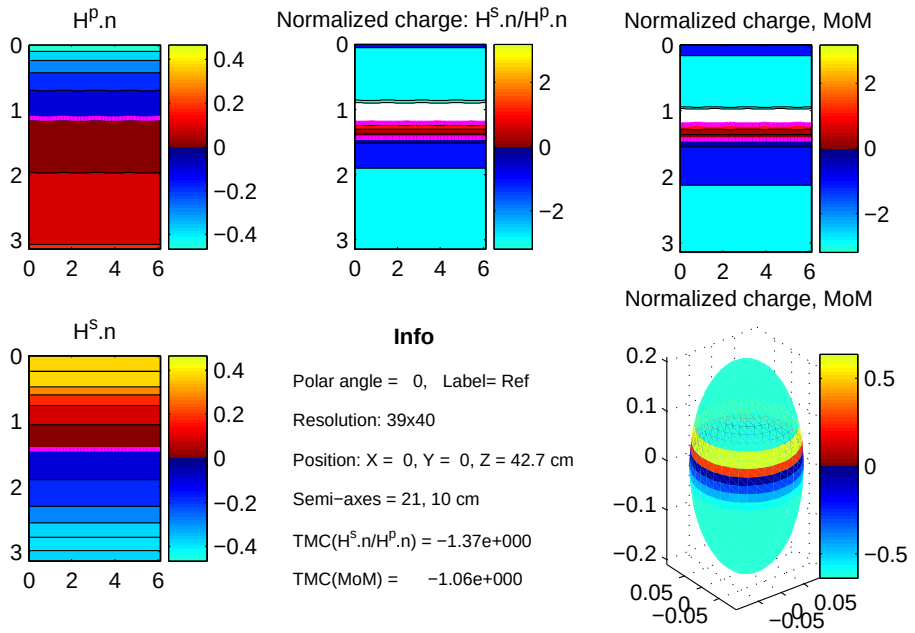

Figure 3.16: Distribution of the normal component of the scattered and primary fields and their ratio at the surface of a spheroid enclosing a vertical cylinder. Reference case.

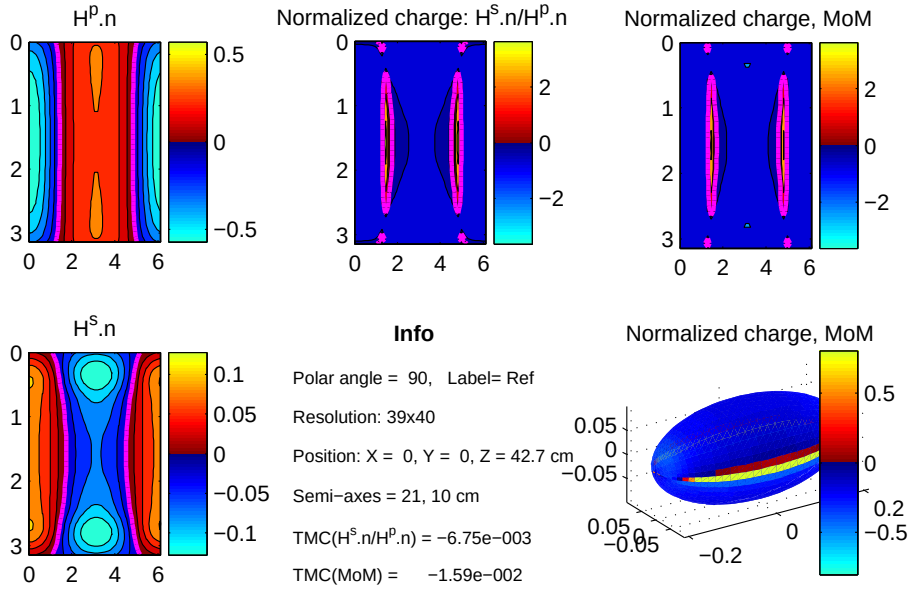

Figure 3.17: Distribution of the normal component of the scattered and primary fields and their ratio at the surface of a spheroid enclosing a horizontal cylinder.

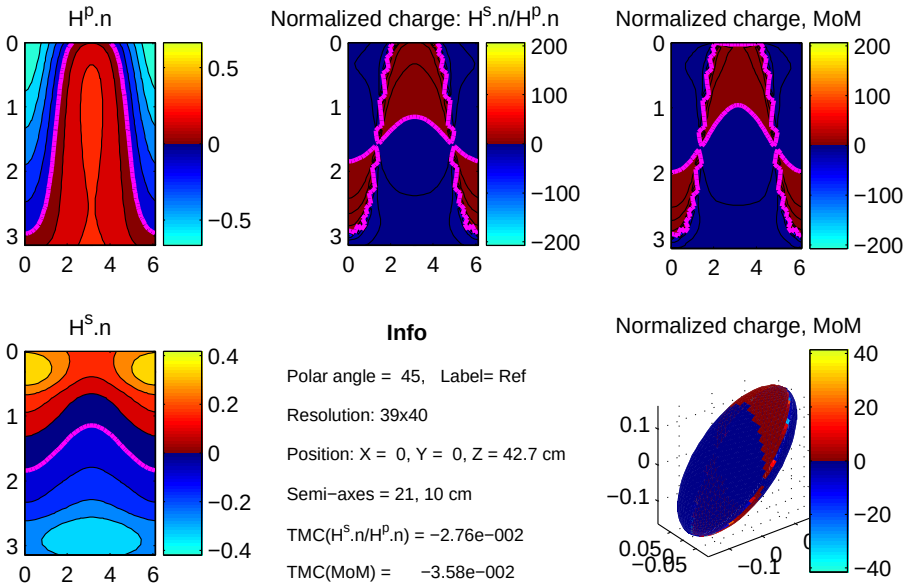

Figure 3.18: Distribution of the normal component of the scattered and primary fields and their ratio at the surface of a spheroid enclosing a cylinder at 45°.

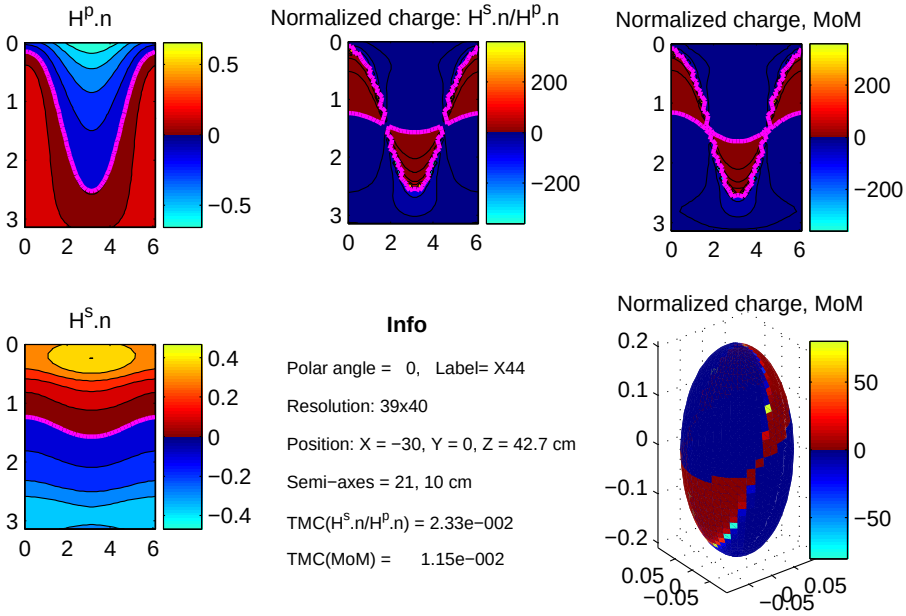

Figure 3.19: Distribution of the normal component of the scattered and primary fields and their ratio at the surface of a spheroid enclosing a vertical cylinder located 30 cm off the center of the transmitter.

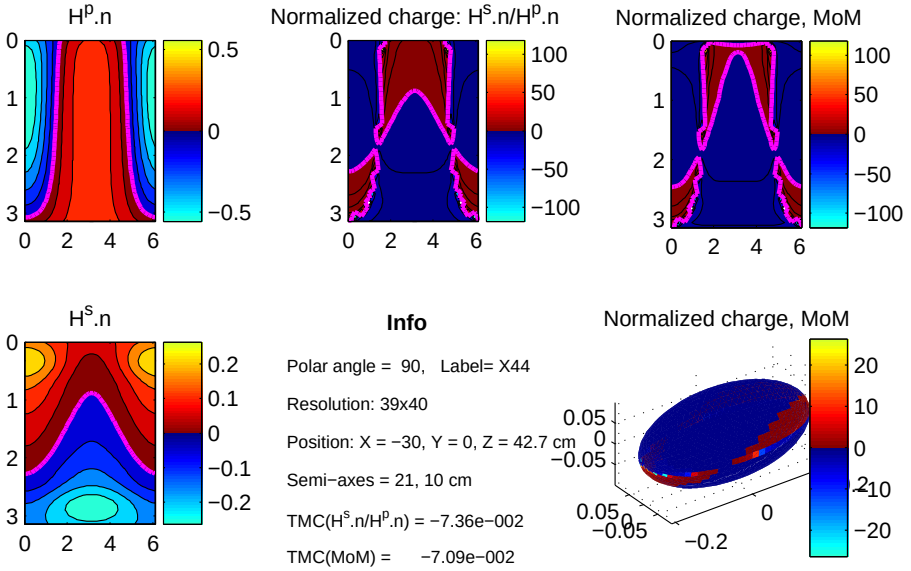

Figure 3.20: Distribution of the normal component of the scattered and primary fields and their ratio at the surface of a spheroid enclosing a horizontal cylinder located 30 cm off the center of the transmitter.

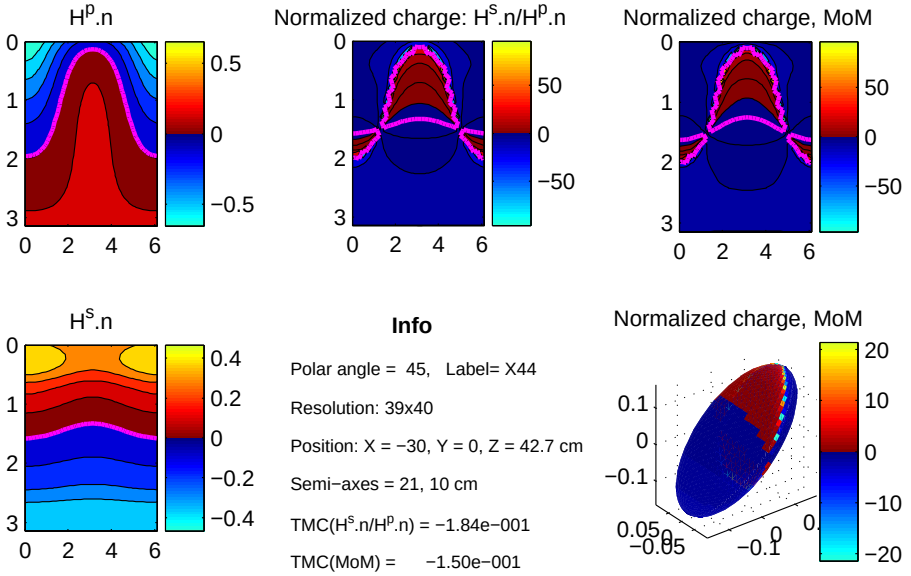

Figure 3.21: Distribution of the normal component of the scattered and primary fields and their ratio at the surface of a spheroid enclosing an oblique cylinder located 30 cm off the center of the transmitter.

Effect of resolution, size and shape

In order to check whether the observed trends are artifacts of the numerical implementation of the problem, effect of resolution in discretization, size and shape of the spheroid were tested in Figures 3.22–3.24. In all cases the charge distribution remains qualitatively similar. The total magnetic charge, however, varies by a factor 60 in the first case with lower resolution, by factor -3 in the second case with semi-axes increased by 50% and by a factor 6 in the third case of a spherical surface.

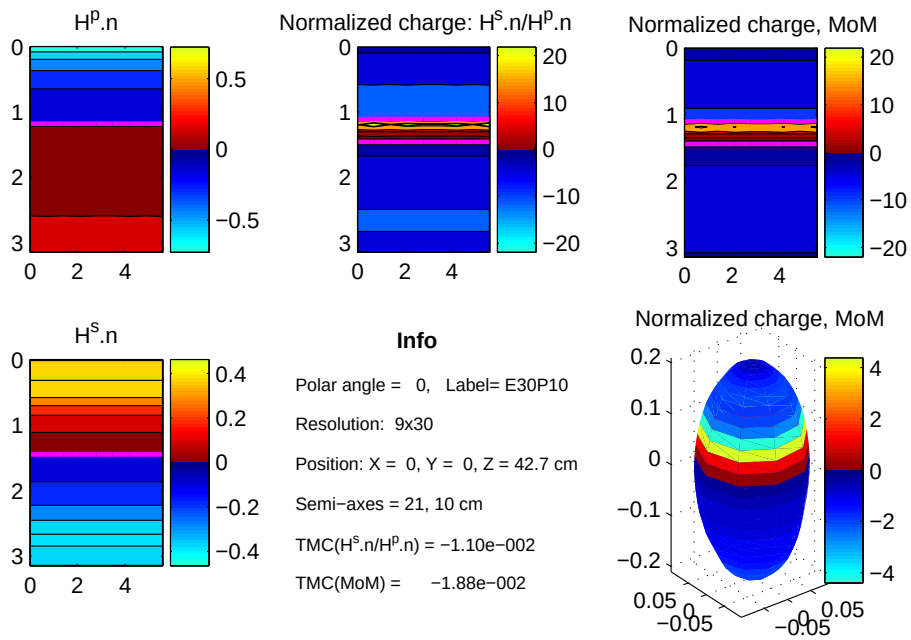

Figure 3.22: Distribution of the normal component of the scattered and primary fields and their ratio at the surface of a spheroid enclosing a vertical cylinder using lower resolution.

Result

The normalized surface charge density distribution varies at the surface of a sphere or spheroid. Its sign varies in a predictable manner that reflects the projections of the primary and secondary fields at the surface of the spheroid. Moreover, singularities in the normalized charge distribution can occur when the normal component of the primary field does to zero. The singularities are avoided only if the normal component of the secondary field also vanishes at the exact same location. That distribution changes when the relative position of the spheroid and transmitter varies, therefore the normalized surface charge density distribution is not a characteristic of an object. TMC changes with the position and orientation of the object, as well as with the shape, size and resolution used for the spheroid, an effect of the aforementioned singularities. This result is in direct agreement with the previous section, this time using spatially varying primary field and a physical model of the secondary field derived from MAS.

3.5.5 Conclusion

The series of tests presented in this section has shown that the normalized magnetic charge q_m is a function of the geometry of the measurement. In order for the total normalized magnetic charge Q to be an effective discriminant, we need to ensure high quality data is taken where the target is excited at numerous angles of primary field excitation. The total magnetic charge for such a measurement then reflects an “average” of the total magnetic charges.

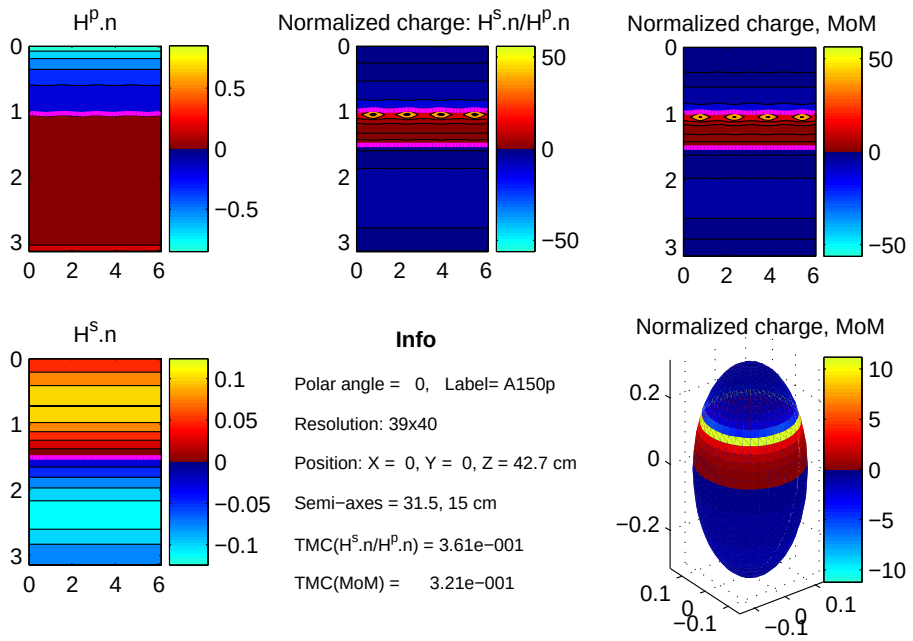

Figure 3.23: Distribution of the normal component of the scattered and primary fields and their ratio at the surface of a large elongated spheroid enclosing a vertical cylinder.

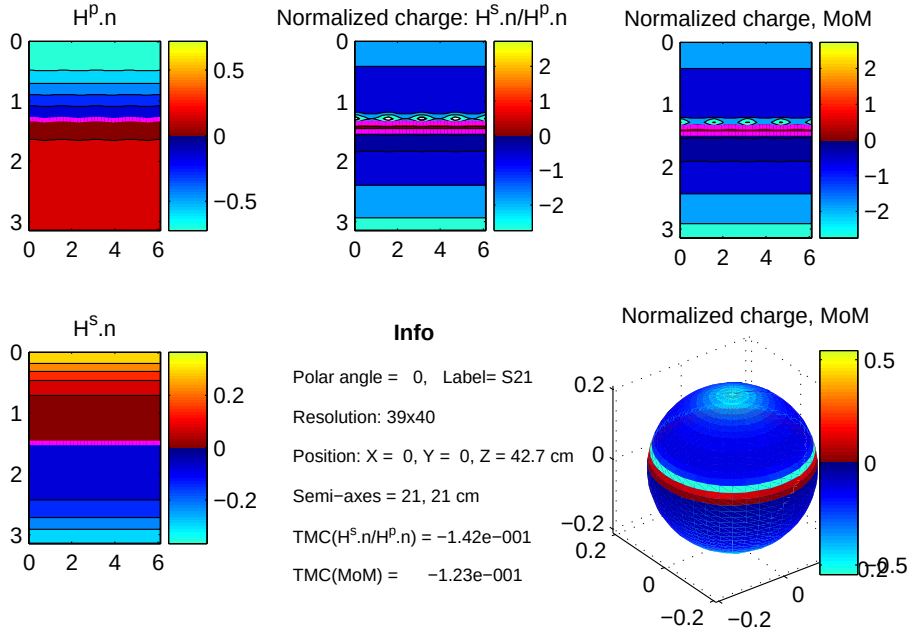

Figure 3.24: Distribution of the normal component of the scattered and primary fields and their ratio at the surface of a sphere enclosing a vertical cylinder.

3.6 Regularized Inversion for a Surface Charge Distribution

Section 3.3.1 describes the numerical forward model that calculates the secondary field produced by a surface charge distribution expanded by a pulse basis function. For a given charge distribution surface, the forward model is linear and can be written as $\mathbf{Zm} = \mathbf{d}$. The objective of the inverse problem is to determine a charge distribution $\mathbf{m}$ from a data set $\mathbf{d}$. There are a number of challenges in determining an optimal $\mathbf{m}$. First, the number of parameters used to represent the charge distribution (i.e., the coefficients multiplying the basis functions) can be greater than the number of data. In such a case the problem is under-determined. Second, data are noisy and special care has to be taken to ensure that our model does not fit the noise. Third, the data may be insufficient to constrain all the model parameters. For example, if the illuminating field is only in a single direction, then the problem is ill-posed.

As demonstrated in Section 3.4, determining the charge distribution by minimizing a data misfit objective function is ill-advised. Figures 3.4(a) and (b) demonstrated that minimizing the data misfit $\|\mathbf{Zm} - \mathbf{d}\|$ produces large spikes in the charge distribution which, in turn, lead to very unstable estimates of the total normalized magnetic charge. In order to solve such an ill-posed inverse problem, the data fitting problem has to be reformulated in order to introduce prior information of the model that we seek. There are several ways to do this reformulation. A statistical framework (Tarantola, 1987; Scales and Tenorio, 2001) is appropriate when our notion of the charge distribution's characteristics can be represented by probabilities. The statistical approach can be used to determine a single model by determining the maximum *a posteriori* probability model, which can be determined by solving an optimization problem.

In the previous section we saw that the surface integral of the un-normalized surface charge (σ_m) was zero. For the remainder of this report, we will use the terms TMC and TNMC to represent the same quantity, i.e., Q.

3.6.1 Formulation of the regularized inverse problem

We use an alternative approach where the prior information is introduced through the introduction of a regularization functional, or model objective function (Parker, 1994; Menke, 1989). The regularization functional quantifies model features (such as amplitude, smoothness, and curvature), and provides a quantitative means of choosing models that are consistent with our preconceived notion of the characteristics of the model. We achieve this by solving an optimization problem:

$$\text{minimize} \quad \Phi = \Phi_{\mathrm{d}} + \lambda \Phi_{\mathrm{m}} \tag{3.62}$$

where Φ_{d} is the data misfit objective function, Φ_{m} is the model objective function, and $0 < \lambda < \infty$ is the regularization parameter. The data misfit function measures the misfit between data predicted by a model and the observed data that we seek to fit. The relationship between the modeled and observed data can be written as

$$\mathbf{d}^{obs} = \mathbf{Zm} + \text{noise} \tag{3.63}$$

Our goal is to fit the data without fitting "noise", where we define "noise" as any component of the observed data that should not be accounted for by the modeling. Therefore noise would include sensor measurement errors, and modeling errors. For our work we will assume that the "noise" is Gaussian and independent. With this assumption, we can write the data misfit as

$$\Phi_{\mathrm{d}} = \|\mathbf{W}_d \left(\mathbf{Zm} - \mathbf{d}\right)\|_2^2 \tag{3.64}$$

where $\mathbf{W}_d$ is the diagonal matrix $\mathbf{W}_d = \text{diag}\left(1/\epsilon_i\right)/\sqrt{(N)}$, with ϵ_i defined as the standard deviation of the ith datum and N the number of data points. With this definition of $\mathbf{W}_d$ the expectancy of data misfit $E[\Phi_{\mathrm{d}}] = 1$ if the model is consistent with the standard deviation of data.

The model misfit Φ_{m} is defined as

$$\Phi_{\mathrm{m}} = \|\mathbf{W}_m \left(\mathbf{m} - \mathbf{m}_o\right)\|_2^2 \tag{3.65}$$

where $\mathbf{W}_m$ is the regularization operator and $\mathbf{m}_o$ a reference model.

Having observed in Section 3.5 that for a homogeneous sphere the normalized charge is uniform, we assume at first order that the charge distribution would be uniform (i.e., similar to a sphere), and that additional structure to the charge distribution would be allowed in order to fit the data. Therefore we define the reference model $\mathbf{m}_o$ to be the uniform charge distribution, where the charge density on each surface element of the discretization can be defined as:

$$[\mathbf{m}_o] = q^{uni} = \text{median}\left[\mathbf{H}_i^{\text{sc}} / \sum_{j=1}^{N} [\mathbf{Z}]_{ij}\right] \tag{3.66}$$

Because un-regularized inversion of data such as in Figure 3.4(b) shows large oscillations of charge amplitude between neighboring rings, we choose to impose a smoother model and define $\mathbf{W}_m$ as the first derivative operator. We note that in that case $\mathbf{W}_m\mathbf{m}_o = 0$; $\mathbf{m}_o$ remains useful to define an approximation to the total magnetic charge of the uniform distribution, while the true uniform distribution is identified after solving the optimization problem of Equation 3.62 and taking the most regularized model, the smoothest model being a uniform one. This subtlety arises from our finding that these two definitions of the uniform model can depart from one another when noise levels are high, thus introducing a bias in Equation 3.66 through the data $\mathbf{H}^{\text{sc}}$.

The parameter λ is chosen to balance the trade-off between the fit to the data and the *a priori* information introduced through the regularization. There are several methods for determining the trade-off parameter (see Farquharson and Oldenburg, 2004, and references therein). For this work we adopt the L-curve criterion for determining the trade-off parameter. The L-curve technique involves generating an $L - curve$ or Tikhonov curve ($\Phi_{\text{d}} = f(\Phi_{\text{m}})$), which are the values of Φ_{d} and Φ_{m} for different values of the trade-off parameter. The optimal λ is chosen to be at the corner of the "L" in the Tikhonov curve, i.e., the point with maximum curvature. By adopting this criterion, the data misfit is large enough to accommodate the presence of noise, while being small enough to provide a satisfactory solution to $\mathbf{Zm} = \mathbf{d}$.

We can now write the inverse problem as

$$\text{minimize} \quad \Phi = \|\mathbf{W}_d\left(\mathbf{Zm} - \mathbf{d}\right)\|_2^2 + \lambda\|\mathbf{W}_m\left(\mathbf{m} - \mathbf{m}_o\right)\|_2^2 \tag{3.67}$$

The solution is obtained by taking the gradient of the Φ and setting $\nabla\Phi = 0$:

$$\mathbf{m}^{rec} = \left(\mathbf{Z}^T\mathbf{W}_d^T\mathbf{W}_d^T\mathbf{Z} + \lambda\mathbf{W}_m^T\mathbf{W}_m\right)^{-1}\left(\mathbf{Z}^T\mathbf{W}_d^T\mathbf{W}_d^T\mathbf{Zd} + \lambda\mathbf{W}_m^T\mathbf{W}_m\mathbf{m}_o\right) \tag{3.68}$$

where we define $\mathbf{m}^{rec}$ to be the recovered model.

Figure 3.25 demonstrates the effect of a regularization on the ring model with the same noisy data as in Figure 3.4(b). The regularized charge model shows a smooth distribution of charge density along the spheroid, in sharp contrast with the large amplitudes observed in the un-regularized case. Additional experiments with 20, 40 and 60 rings show that the same regularization procedure yields the exact same distribution. For the remainder of this study we use 40 rings to discretize the spheroidal surface, as we feel that this level of discretization is sufficiently fine to model the charge distributions of relatively complex objects without requiring excessive computational effort.

The low data misfit and high correlation coefficient between the observed data and the model prediction are similar to those of the un-regularized model. However, the calculated total magnetic charge derived from the different models differ by several orders of magnitude. The patch model, the unregularized ring model and the regularized ring model have total magnetic charge values of 38×10^3, -1.09×10^1 and -2.15×10^{-2}, respectively. For the total magnetic charge to be a stable discrimination criterion we must understand how discretization and regularization affect the total magnetic charge.

Figure 3.26 demonstrates the effect of regularization on the amplitude of the charge density distribution. At early stages of the regularization (small λ), charges vary between 10^4 and -10^4 (the top panel). At later stages, larger values of λ bring down the amplitude by a factor over 10^5, shift the peaks of oscillations and force convergence toward a flat uniform distribution near the value of $\mathbf{m}_o$.

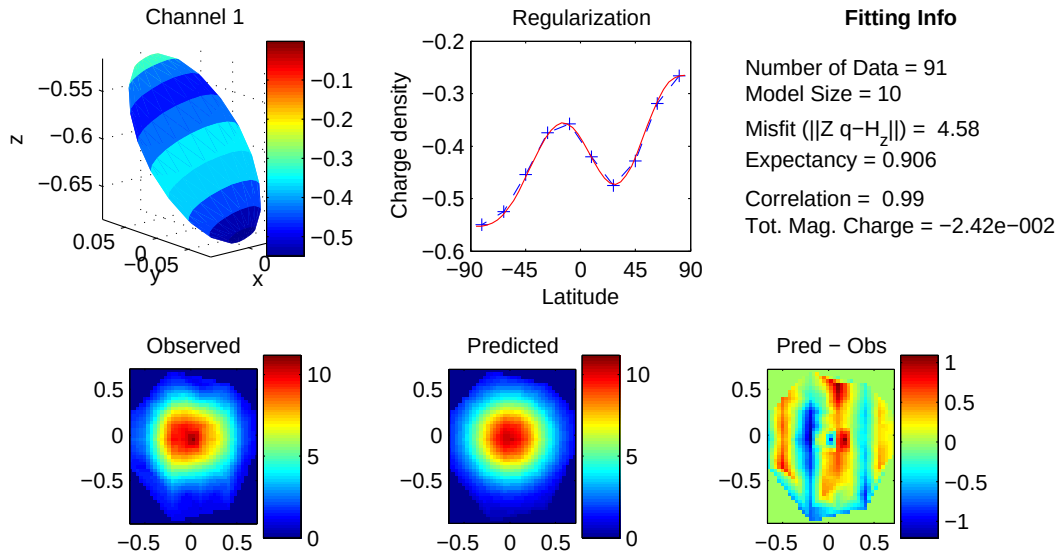

Figure 3.25: Regularized ring solution for 40 mm projectile (45 degrees, 60 cm below sensor). In top central panel, crosses show the 10-ring solution, the solid red line the 40-ring solution using the exact same automated regularization procedure (described in section 3.6.3). Misfit, expectancy, correlation and total magnetic charge exactly coincide for 10-40 rings.

3.6.2 Total magnetic charge and regularization

The left panel of Figure 3.27 illustrates the concept of L-curve for the previously exposed case of a 40 mm projectile at 45 degrees and 60 cm below an EM-63 sensor. A common method for choosing an appropriate regularization is to pick the one that corresponds to the corner of the L-curve. As regularization becomes larger the misfit Φ_{d} grows and the charge distribution becomes smoother. Conversely, for weak regularization the model can fit the data so well that it also fits noise, and therefore becomes sensitive to noise. The corner of the L-curve is shown with a star. The large dot represents an alternative pick explained in the next section. The right panel shows L-curves for the same projectile at different depths and orientations. For instance, the dashed line corresponds to a vertical orientation, where regularization plays an important role on model misfit, as reflected by the larger variation of Φ_{d}.

The previous sections showed that the total magnetic charge can depend on discretization and regularization. This first result is troubling because it contradicts the claim of Shubitidze that the total magnetic charge can be used as a classification criterion among UXO, and therefore that it should remain independent of object position, orientation and background noise. Focusing on the method of rings, we study in Figure 3.28 the total magnetic charge Q during regularization (parameter λ) for the same 40 mm target as in Figure 3.27. In the left panel the object is at 45 degrees. Its total charge, the blue solid dotted line, varies significantly as λ increases and seems to converge at a later stage toward the horizontal dashed line, the total magnetic charge Q_{uni} for the model with uniform distribution of charge density. This is expected because the limit case of regularization by smoothing is a flat uniform model. As in Figure 3.27, the star indicates the model chosen for the corner of the L-curve (λ_{reg}), the dot an alternative regularization. Neither of these points marks any particular position for the Q curve.

We consider different orientations and depths of the same target in the right panel of Figure 3.28 to further study the total magnetic charge of the 40 mm projectile. Each line style corresponds to the same cases as in Figure 3.27. Figure 3.28 shows that each configuration of depth and orientation generates different variations of Q during the regularization process. These variations are larger when the inclination of the object is greater, as

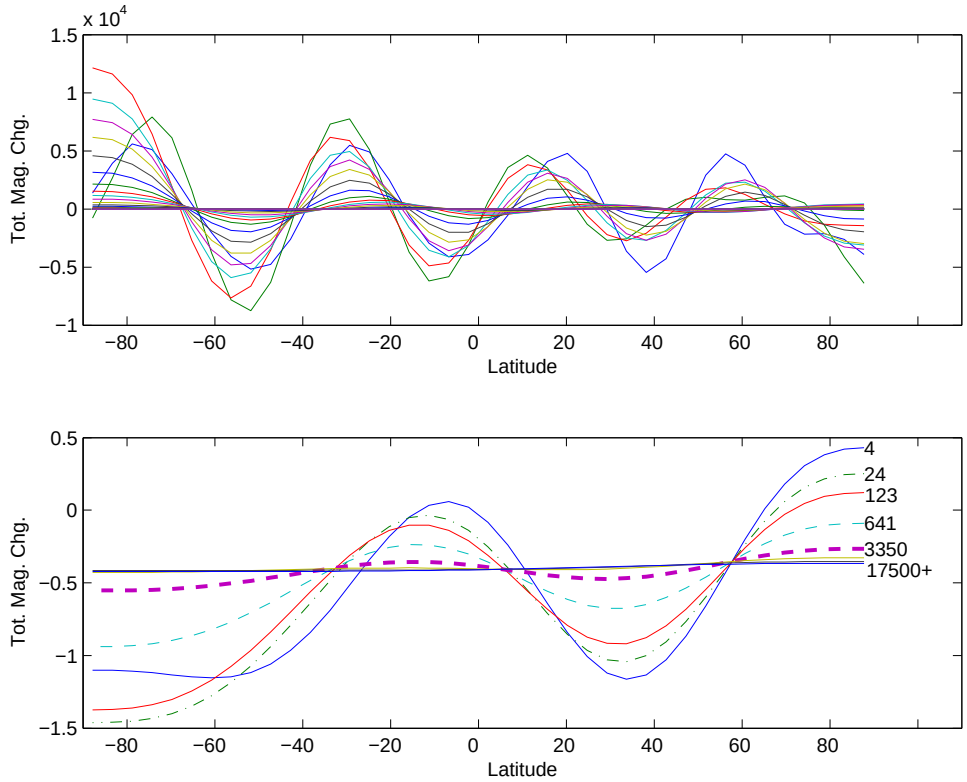

Figure 3.26: Charge distribution on 40 rings along modeling spheroid for same 40 mm item (Latitude +90 for the pole closest to the surface, 0 equator, -90 bottom). Top panel: all regularized models, least regularized with largest amplitude, λ in log scale from $10^{-}10$ to 10^{5}. Lower panel: sampled models for lambda = 4, 24, 123, 641, 3350, 17500 and above. The thick dashed line corresponds to the regularization applied for Figure 3.25.

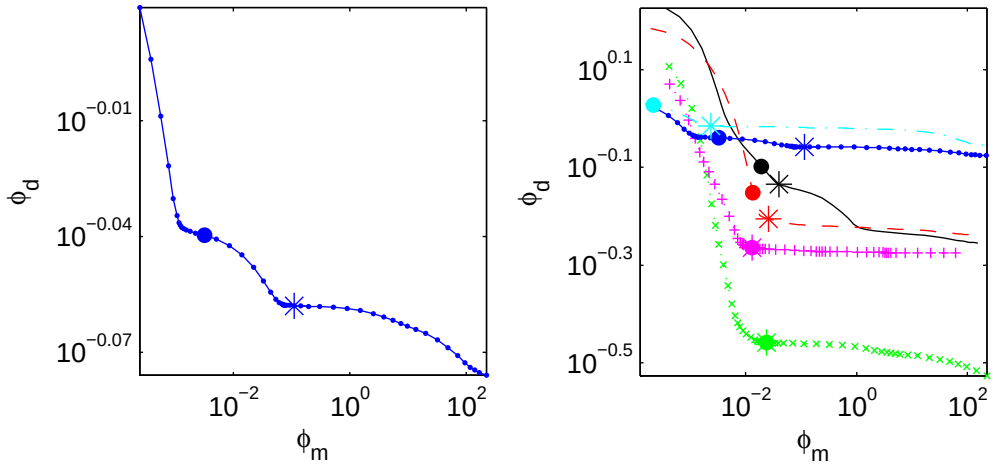

Figure 3.27: Example of L-curves (i.e. Φ_{d} vs. Φ_{m} curves) for a 40 mm projectile. Left panel: object at 45 degrees, 60 cm below sensor. Stars indicate maximum curvature, large dots alternative pick for regularization. Right panel: black, red and green curves correspond to shallow depth (20-25 cm), the remaining ones to deeper position (60 cm); black solid line and blue line-dot at 45 degrees, red dashed and cyan dash-dot vertical, green crosses and magenta plus markers horizontal.

illustrated by the red and cyan curves that span several orders of magnitude with change in sign, as opposed to the more contained variations for a horizontal position (green crosses and magenta plus signs). Furthermore, none of these Q curves seems to share any common global or local extremum, which *a priori* complicates the choice of Q. Star markers show that choices of Q(λ_{reg}) from the corner of the L-curve do not provide a consistent value, thus a traditional approach to regularization is not compatible with a unique and invariant total magnetic charge of the 40 mm projectile.

Searching for common features among Q curves, we consider the total magnetic charge Q_{uni} for the model of uniform distribution of charge density. The dashed horizontal lines in the right panel of Figure 3.28 show that its value remains similar for all these different positions and orientations, with mean –0.0231 and standard deviation 0.0024. Could the uniform distribution provide an adequate forward model to predict data recorded at the surface? Detailed analysis reveal that these models are limited to predicting radial EMI responses, yielding misfits that are generally too large to qualify them as acceptable solutions to $Zm = d$. This is particularly obvious for heterogeneous objects that lie in sub-horizontal position because their EMI response reflects their spatial heterogeneity. This test and many more with real data (some of which are discussed in the next section) and synthetic data show that the uniform distribution is a stable characteristic of an item but a poor forward model. An alternative choice of regularization is thus warranted for the forward model.

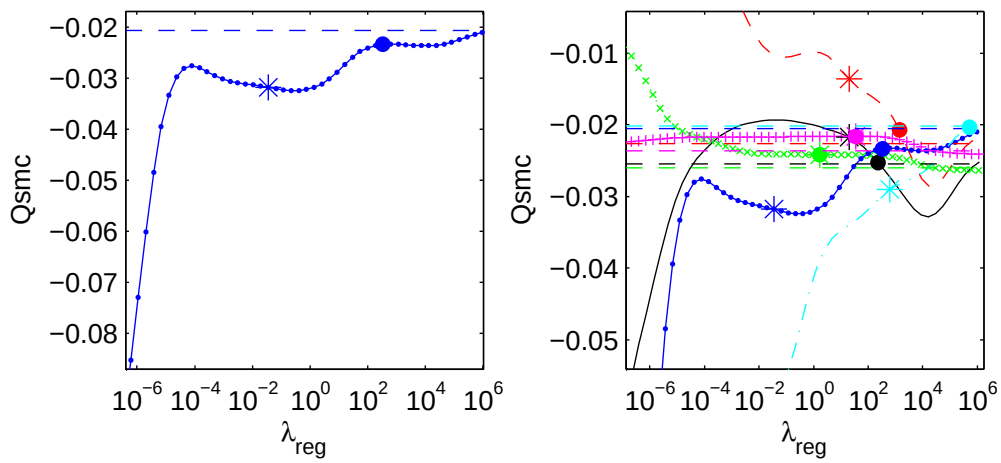

Figure 3.28: Total magnetic charge vs. regularization parameter, same legend and setting as previous figure. Left panel shows large variations of total magnetic charge Q_{smc} during the regularization. The dashed horizontal line shows $Q_{\mathrm{smc}}(\mathbf{m}_o)$ (also called Q_{uni}). Right panel shows Q_{smc} and Q_{uni} for different orientations and depths. Q_{uni} is similar for all cases.

3.6.3 Regularizing for a stable total magnetic charge

The previous section has shown that the corner of the L-curve does not guarantee an invariant total magnetic charge whereas a uniform charge distribution provides a stable Q but a potentially deficient forward model, especially for sub-horizontal items. In that context, we consider the best solution to be one that satisfies both Q(λ) is close-enough to Q_{uni} and the misfit is of the same order as the noise. Theory and extensive tests with real measurements and synthetic data show that there is always a solution to the first condition because large regularization imposes smoothness and eventually flatness to the charge distribution. Besides, there are often models whose total magnetic charge approach Q_{uni} at early stages of regularization, as illustrated in Figure 3.28 by crossings of Q_{uni} curves by Q curves for small values of λ. These models are potential candidates because their misfit is low without them fitting noise owing to some regularization. Other possible candidates appear as regularization increases and Q gradually approaches Q_{uni}, before the charge distribution becomes uniform. Practically, quantitative values must be assigned to properly define the notion of approaching Q_{uni}.

Method 1

We propose to choose the regularization parameter λ such that

$$\frac{\|Q(\lambda) - Q_{uni}\|}{\|Q_{uni}\|} < \delta \tag{3.69}$$

and

$$\frac{1}{K_1} < \Phi_{\mathrm{d}} < K_2 \tag{3.70}$$

with $E(\Phi_{\mathrm{d}})$ = 1 if the model fits data but not noise. We applied this method by first setting $delta = 20\%$, $K_1 = 2$ and $K_2 = 1.5$, allowing an error of 20 % on Q and 50% on noise estimate. If there is no solution we first relax δ to 30% and set $K_1 = 4$, $K_2 = 2$, then relax further to $\delta = 50\%$, $K_1 = 8$ and $K_2 = 3$.

Method 2

Noise and errors from instruments, measurements and modeling are not necessarily straightforward to assess. *A priori* error estimate can be inaccurate and misleading and cause the method above to fail, even though we find it to perform well most of the time. When it fails we can either choose the model with Q closest to Q_{uni}, or pick the corner of the L-curve. In either case we loose control on one of the criteria. To circumvent this difficulty one can assume that the corner of the L-curve provides an acceptable misfit thanks to its balance position in fitting data and noise, with expectancy of Φ_{d} is $E(\Phi_{\mathrm{d}})\Phi_{\mathrm{d}}(\lambda_{\mathrm{corner}})$. This is the classical justification for using the L-curve (e.g Hansen, 1997; Farquharson and Oldenburg, 2004). Identifying the corner of the L-curve by its maximum curvature, we search for a model near that corner and with a total magnetic charge close to Q_{uni}. Similarly with the previous method, our search algorithm identifies the regularization parameter λ that simultaneously minimizes the relative difference between Q_{uni} and Q on the one hand, and between $E(\Phi_{\mathrm{d}})$ and Φ_{d} on the other hand:

$$DQ = |max(Q(\lambda), Q_{\mathrm{uni}})/min(Q(\lambda), Q_{\mathrm{uni}})) - 1| < dQ \tag{3.71}$$

$$D\Phi = |max(\Phi_{\mathrm{d}}, E(\Phi_{\mathrm{d}}))/min(\Phi_{\mathrm{d}}, E(\Phi_{\mathrm{d}})) - 1| < dE. \tag{3.72}$$

After testing several methods for satisfying both conditions, we choose to search for the minimum of $P = [DQ * D\Phi](\lambda)$ within the tolerance defined by dQ and dE. Variation on the definition of the product P of the two conditions do not offer any gain.

With this second method and estimation of noise through the L-curve we find that tighter constraints are applicable. The method is validated by inversion of synthetic data (produced with dipole model) and real data obtained from the USACE-ERDC test stand for 40 mm, 60 mm, 90 mm and M42 projectiles, for which two depths (1 shallow, 1 deep) and three inclinations (0, 45, 90 degrees) were surveyed with a 26-time-channel Geonics EM-63. In the case of real data, the corner of the L-curve proved to be an adequate solution in 19% of inversions with $DQ \leq$12.5%; for the remaining inversions, 38% of cases were within the bound dQ=dE=12.5%, 30% within dQ=dE=25%, 12% within dQ=2dE=100% and the last 1% within dQ=200% and dE=75%.

Application of this method to the 40 mm projectile is illustrated in Figures 3.27 and 3.28 by the large dots previously defined as alternative regularization. Extensive tests presented in the following section confirm the robustness of the method in a wider setting. Figure 3.29 illustrates the effect of different regularizations for the inversion of noisy data acquired over a 40 mm UXO at the Sky Research test plot. Comparison between observed data and predictions shows that all models except for the most regularized one yield acceptable fit with the observed data. Differences between the models for the L-curve and the chosen regularization are negligible.

Conclusion

We have now established a procedure for regularized inversion of electromagnetic data with SMC that provides a forward model that closely predicts surface observations and a stable total magnetic charge derived from

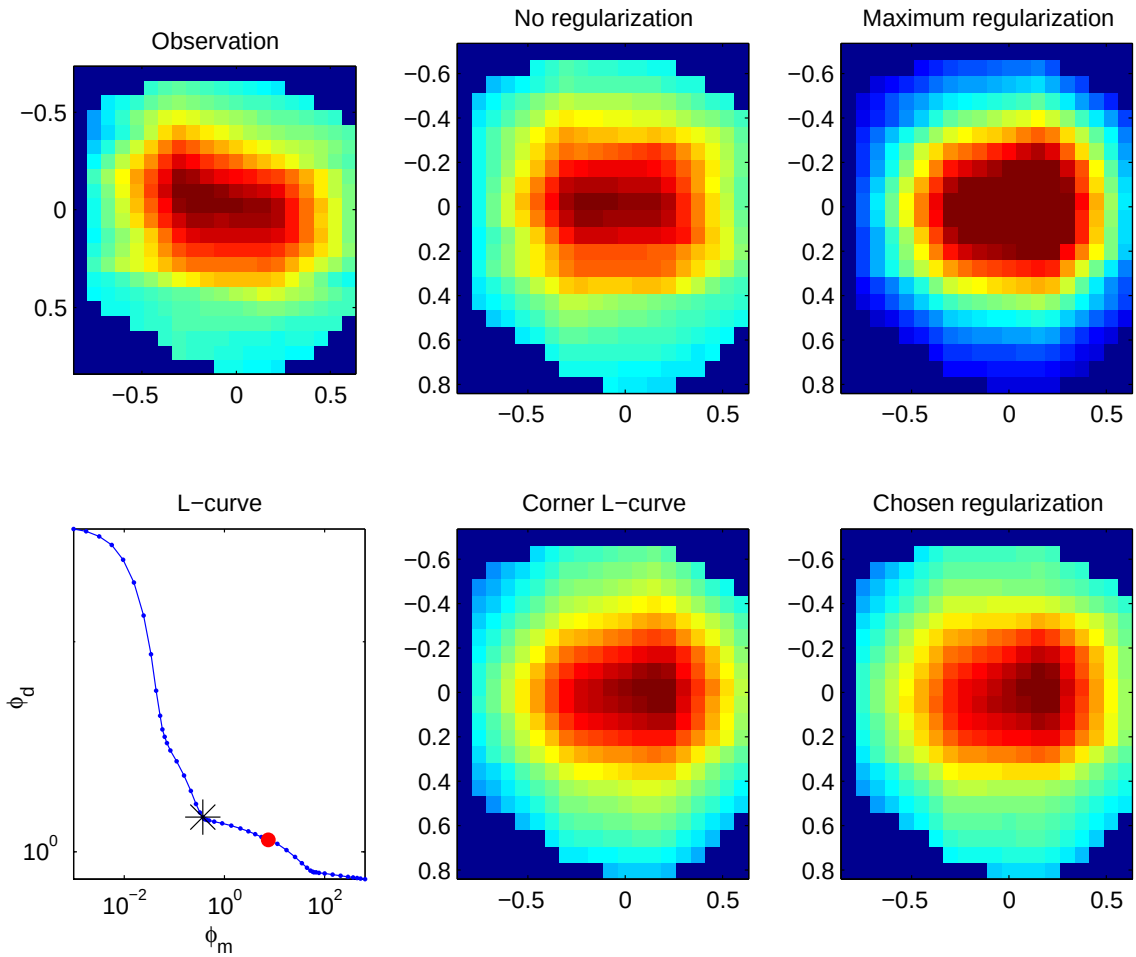

Figure 3.29: Regularization of field data over a 40 mm UXO. L-curve, Observation and model for different levels of regularization. Corner of L-curve indicated with a star, our chosen regularization with a red dot.

the uniform charge density. The total magnetic charge derived with this method is independent of the number of rings used for discretization, would they be 10, 40 or 60. In the following applications 40 rings are used to allow for the complexity of bodies with composite structure (geometry, material with different conductivity and magnetic permeability), while regularization handles the redundancy of parameters.

Alternative avenues of regularization were also explored during our close examination of the surface magnetic charge model. We replaced, for instance, the search for a smooth model by one that exhibits the smallest total magnetic charge (replacing the elements of the regularization matrix $\mathbf{W}_m$ by the surface area of each ring). The resulting regularization remained too weak to temper out the large oscillations in charge amplitudes. We also tested $\mathbf{W}_m$ as the second derivative operator, $\mathbf{W}_m$ becoming either a rank-2 deficient operator, or a full-rank matrix when boundary conditions such as null charge beyond the spheroid were applied. These formulations lead to similar results to those reported for the standard case. Black-box types of regularization procedures such as the MatLab functions lsqnonneg (positivity constraint) and linprog (linear programming solutions) were found to be less stable than the regularizations discussed above, both for rings and patches. Another possible way of controlling the charge distribution is decomposition through a given number of simple basis functions (sine-cosine). This method was tested on a sphere (icosahedron) with two-dimensional Fourier series truncated to limited modes to restrict the amount of features in the charge distribution. Results not presented here show that stability of the total magnetic charge can be achieved with careful choice of truncation. A systematic procedure remains to be formulated. Because modeling an ordnance with a sphere simplifies the inversion problem by removing the orientation variables, further work is warranted to explore that possible avenue.

3.6.4 Stability of the regularization method

Adding controlled noise

Ability of the regularized inversion to produce a model with misfit $\|Zm - d\|$ comparable to noise can be tested in an environment where noise is controlled. This can be done by considering shallow measurements ($\mathbf{H}^{\mathrm{sc}}$) with the 40 mm projectile where signal is high and noise remains low. Noise can then be arbitrarily added to the instrument (ϵ_{inst}, $\%$) and to the data (ϵ_{data}, $\%$) according to

- added instrument error: $IE = R1 * \epsilon_{\mathrm{inst}}$

- added data error: $DE = \mathbf{H}^{\mathrm{sc}} * diag(R2) * \epsilon_{\mathrm{data}}$

- total added noise $\Delta E = IE + DE$,

with $R1$ and $R2$ vectors of length M with random entries, chosen from a normal distribution with mean zero, variance one and standard deviation one; $diag(R2)$ is the matrix with diagonal $R2$ and zeros everywhere else. Results are summarized in Table 3.3 and 3.4.

ϵ_{inst}, ϵ_{data}	Φ_{d}	$\|1/\mathbf{W}_d\|$	$\|\Delta E\|$	$E(\Phi_{\mathrm{d}})$	**Q**	Q_{uni}	**Corr.**
No noise	28	80	0	0.35	-0.0242	-0.0260	1
500, 10	100	84	95	1.0	-0.0248	-0.0265	0.99
2000, 30	323	73	315	3.8	-0.0252	-0.0253	0.92
2000, 50	419	73	496	5.2	-0.0259	-0.0273	0.87

Table 3.3: 40 mm object in horizontal position, 25 cm below sensor, 1st time channel. Φ_{d} is model misfit; $\|1/\mathbf{W}_d\|$ is the assigned error (from automated estimate of standard deviation of data and instrument error); $\|\Delta E\|$ is noise added to noise-free data; $E(\Phi_{\mathrm{d}})$ is the expected noise as in $\mathbf{W}_d$, departure from 1 means that automated guess on noise level was inaccurate. The method is deemed successful if Φ_{d} is close to $\|\Delta E\|$ and Q to Q_{uni}.

Both tables confirm that even when data are largely corrupted by noise the proposed regularized inversion

ϵ_{inst}, ϵ_{data}	Φ_{d}	$\|1/\mathbf{W}_d\|$	$\|\Delta E\|$	$E(\Phi_{\text{d}})$	**Q**	Q_{uni}	**Corr.**
No noise	82	102	0	0.80	-0.0253	-0.0254	1.00
500, 10	153	92	158	1.5	-0.0237	-0.0239	0.98
2000, 30	442	99	403	4.1	-0.0242	-0.0246	0.89
2000, 50	715	134	807	4.84	-0.0413	-0.0277	0.87

Table 3.4: 40 mm object, 45° inclination, 25 cm below sensor, 1st time channel.

method maintains (1) stable total magnetic charge, (2) misfit comparable with added noise $\|\Delta E\|$ and (3) large correlation between data and prediction. The third columns in both tables suggest that the method for assigning expected errors in the weighting matrix Wd is not optimal, expected errors are generally over-estimated when noise is low and under-estimated when noise is high. This shortcoming does not, however, affect the performance of the proposed regularization method, which relies instead on the corner of the L-curve to identify eligible models that strike the right balance between model complexity and misfit. This property is confirmed by the general agreement between added noise and misfit with the chosen model. It is also confirmed that amongst those eligible models it is possible to select some with total magnetic charge near Q_{uni}. Results hold for large amounts of noise: relative error for Q reaches 62% for added noise $\epsilon_{\text{data}} = 50\%$ in Table 3.5.

Noise and regularization for different types of ordnance

Adaptability of the method to different size and shape of ordnance is tested on three additional standard items: the 60 mm, 90 mm and M42 ordnance. Several orientations and depths are tried (Table 3.5) with the 1st and 12th time channels of data collected with a Geonics EM-63 sensor at the USACE-ERDC Vicksburg, MS test stand. These items are chosen because the 40 mm, 60 mm and 90 mm have distinct sizes, while the 40 mm and M42 have similar size but different physical properties (40 mm is made out of aluminum and copper, M42 of steel). The 1st time channel is taken for its high SNR and the later 12th time channel to illustrate the effect of high noise levels. Figure 3.30 and 3.31 show results of inversions for data processed with their original noise. Table 3.6 gathers significant statistics for the total magnetic charge derived from the uniform distribution.

Object / Inclination Depth	**Horiz. Shallow**	**45° Shallow**	**Vert. Shallow**	**Horiz., 45°, Vert. Deep**
40 mm	25.4 cm	21 cm	24 cm	60 cm
60 mm	60 cm	60 cm	60 cm	100 cm
90 mm	60 cm	60 cm	60 cm	100 cm
M42	25.8 cm	21.8 cm	25 cm	60 cm

Table 3.5: Depth and inclination of measurements over test stand.

Figure 3.30 shows results for the 1st time channel. In all panels the total magnetic charge exhibits large variations during regularization, except when the item is not horizontal, as previously observed in Figure 3.28. Choice of the corner of L-curve (star markers) yields unstable total magnetic charge, especially for 60 mm and M42 items. Conversely, Table 3.6 show that Q_{uni} obtained with the uniform charge model keeps a stable value through changes of position, its standard deviation remaining at least five times smaller than the amplitude of Q_{uni}. Use of regularization for Q near Q_{uni} (dot markers in Figure 3.30) provides both stable total magnetic charge and adequate fit to data.

Figure 3.31 shows the same four items at the 12th time channel, where signal gets weaker and noise relatively increases. Examination of SNR reveals that at a shallow depth clear distinction of the target is possible with SNR larger than 12. At deeper positions inversion of data remains possible even though SNR lowers to 2–8 (minimum for 60 mm item horizontal at 1 m below sensor and M42 horizontal at 60 cm below sensor, both shown with magenta line with plus signs). Study of late time channels and noisy environments suggests increasing separation between "classic" (L-curve) and "special" (L-curve+Q_{uni}) regularization methods when SNR decreases, here visible for all four items in Figure 3.31. With different choices of the regularization parameter Q can vary tenfold

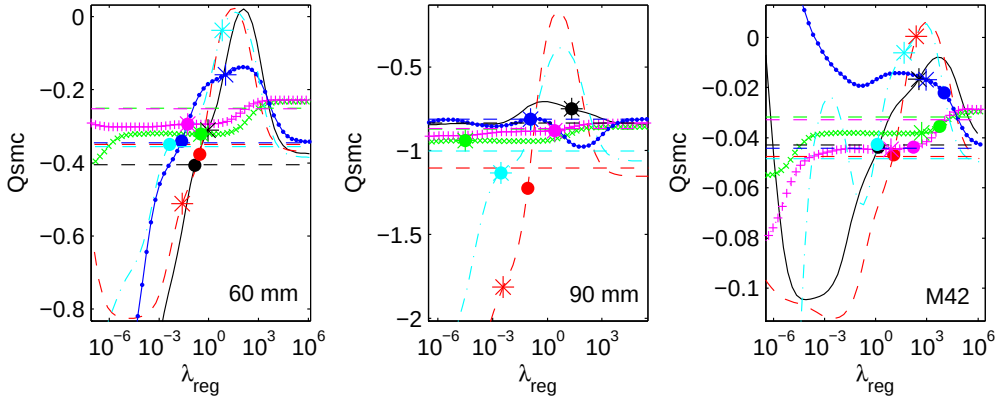

Figure 3.30: Variation of Total magnetic charge $Q_{\rm smc}$ during regularized inversion of first time channel for 60 mm, 90 mm and M42 projectiles. For all panels, each curve shows $Q_{\rm smc}$ for a different position/orientation of target relative to test stand. Horizontal dashed lines show $Q_{\rm uni}$ for each case and define the region of stability of the total charge. Large dots indicate $Q_{\rm smc}$ for the proposed regularization choice whereas stars highlight failure to obtain stable charge with corner of L-curve. Positions/orientations are given in Table 3.5. Black, red and green curves correspond to shallow depths, blue, magenta and cyan to deeper positions; black solid line and blue line-dot at 45 degrees, red dashed and cyan dash-dot vertical, green crosses and magenta pluses horizontal, as in Figure 3.27.

UXO / $Q_{\rm uni}$	**Mean** $Q_{\rm uni}(T_1)$	$\sigma Q_{\rm uni}(T_1)$	**Mean** $Q_{\rm uni}(T_{12})$	$\sigma Q_{\rm uni}(T_{12})$
40 mm	-0.023	0.0024	-0.0076	0.0007
60 mm	-0.326	0.062	-0.073	0.022
90 mm	-0.915	0.114	-0.206	0.051
M42	-0.041	0.007	-0.003	0.0009

Table 3.6: Mean and standard deviation of $Q_{\rm uni}$, the total magnetic charge for uniform distribution of normalized surface charge density, at 1st (T_1) and 12th (T_{12}) time channels.

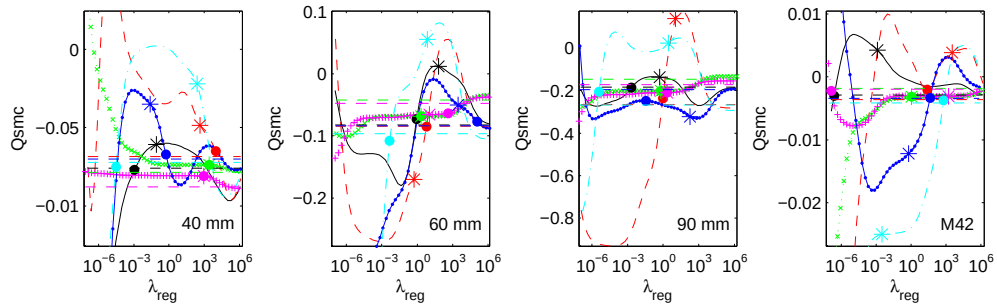

Figure 3.31: Total magnetic charge $Q_{\rm smc}$ during regularization for 40 mm, 60 mm, 90 mm and M42. Each panel shows all six positions given in Table 3 using the 12th time channel with the same plotting conventions as previous figure.

and even change sign, as observed for the 60 mm and M42, while Q_{uni} remains stable for all items (Table 3.6).

3.6.5 Detailed analysis of four standard ordnance

Total magnetic charge and time

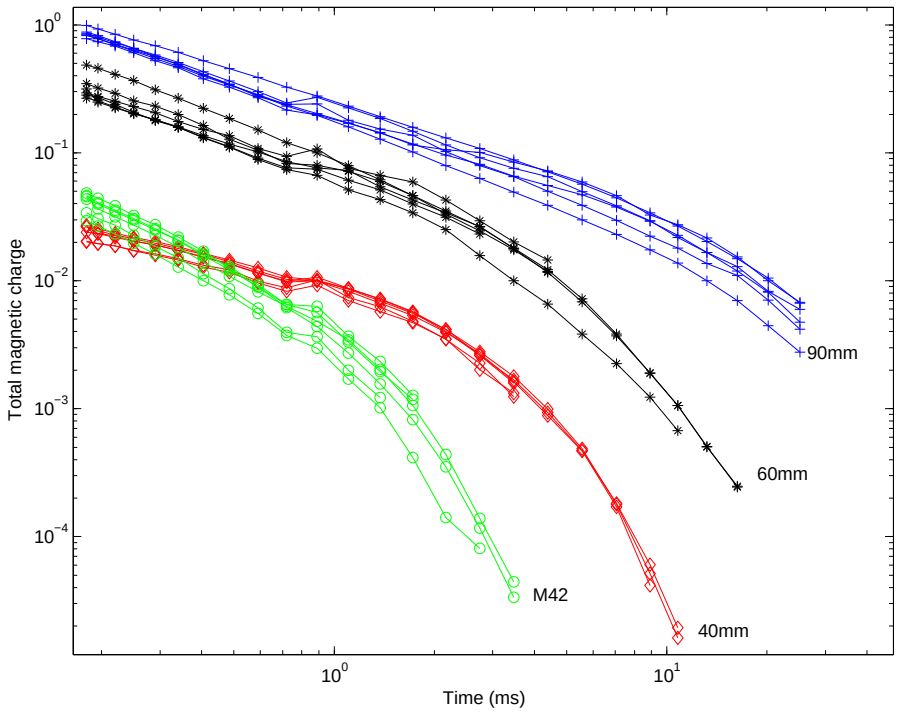

Figure 3.32: Total magnetic charge as a function of time for 40 mm, 60 mm, 90 mm and M42 projectiles, using EM-63 data from test stand at positions summarized in Table 3. Time series are shorter for smaller objects because SNR is too low at later time channels.

As a last test on method stability, regularized inversion and detailed analysis are applied to data sets for 40 mm, 60 mm, 90 mm and M42 standard ordnance at multiple depths and orientations. The Geonics EM-63 sensor acquired data on the USACE-ERDC Vicksburg test stand at 26 time channels (0.18 ms to 25.14 ms), two depths (one shallow, one deep) and three inclinations (0, 45, 90 degrees), as in Table 3.5. Figure 3.32 shows the total magnetic charge as a function of time for all measured configurations obtained with the proposed regularized inversion algorithm for NSMC. Several conclusions can be drawn:

- All lines cluster for each object; the recovered total magnetic charge is therefore a stable feature and the inversion is robust;
- Each object has a distinct time evolving total magnetic charge;
- The magnitude of the total magnetic charge scales with the volume of the object;
- Objects with different physical properties have different time decay for the total magnetic charge, as illustrated by the M42 and 40 mm items that have similar size but different material.

These results suggest clear and stable separation with NSMC and the total magnetic charge for these four types of ordnance, thus opening the possibility of applying automated discrimination procedures. As a side note, there is a slight increase of the total magnetic charge for the 10th and 11th time channels. This effect is only due to a pervasive instrument bias, not to any physical property or modeling issue, and would not appear should the sensor be perfectly calibrated.

Error analysis

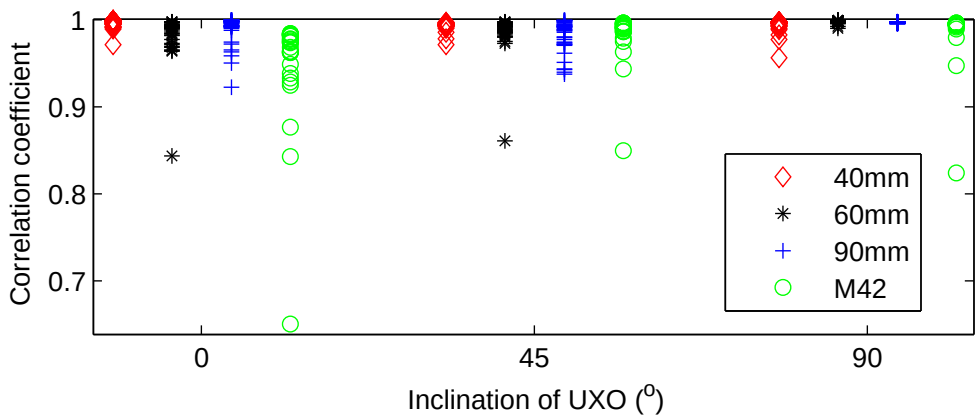

Figure 3.33: Correlation coefficient between observed data and model prediction for all time channels, 2 depths and 3 inclinations (0 for horizontal).

Having established the stability of the total magnetic charge for the 40 mm, 60 mm, 90 mm and M42 at various depths and orientations, we examine the quality of prediction of the forward models employed above. Special consideration is given to correlation, misfit and ability to perform at low SNR. Figure 3.33 shows the correlation coefficient between the observation and model prediction for all time channels as a function of the inclination of the item, with the different depths superposed. Correlation close to unity in most cases proves that model predictions are reliable. The few occurrences of low correlation correspond to late time channels where data quality is poor. Best performance is achieved for targets in vertical position, in which case the signal recorded at the surface takes the shape of a simple radial decay away from the center of target because UXO are bodies of revolution. Success when there is central symmetry in the data is not surprising because our model does assume central symmetry of charges along the main axis of the modeling spheroid (i.e., rings with uniform charge) here in vertical position, and thus naturally fits the data.

Figure 3.34 measures the misfit of models obtained through the proposed regularized inversion method with the expected noise estimated from the corner of the L-curve. In 97% of tested cases misfit lies within a 25% relative difference with estimated noise, thus proving that the method generally converges.

Figure 3.35 provides the conditions of signal to noise ratio throughout the sets of measurements. SNR varies by several orders of magnitude for different depths and times. Inversions are not carried out when SNR is lower than two or when there are less than ten data with values above the estimated standard deviation of noise; SNR is then set to 0. SNR is particularly low at late time channels, or at all times for small items placed at greater depth, e.g. 40 mm, 60 mm and M42. Regularized inversion of NSMC is able to perform at low SNR and has potential for use even with highly contaminated data.

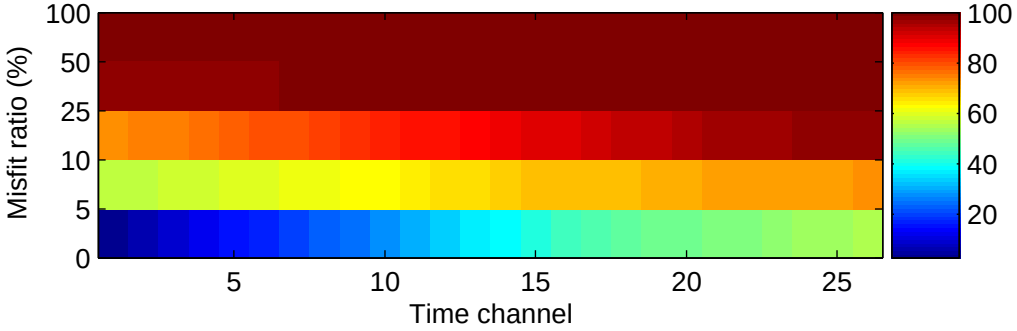

Figure 3.34: Percentage of solutions for which $|\Phi_{\mathrm{d}}(regu)/\Phi_{\mathrm{d}}(corner) - 1|$ smaller than misfit ratio ($D\Phi$) as a function of time channel. The lowest row shows that in 55% of cases the misfit ratio is below 5%, which means that the misfit for the chosen parameter is within 5% of that of the corner of the L-curve (assumed best guess for noise estimation). The next lines show that 73% of cases are below 10% misfit ratio, 97% below 25%, 99.5% below 50% and 100% below 100%.

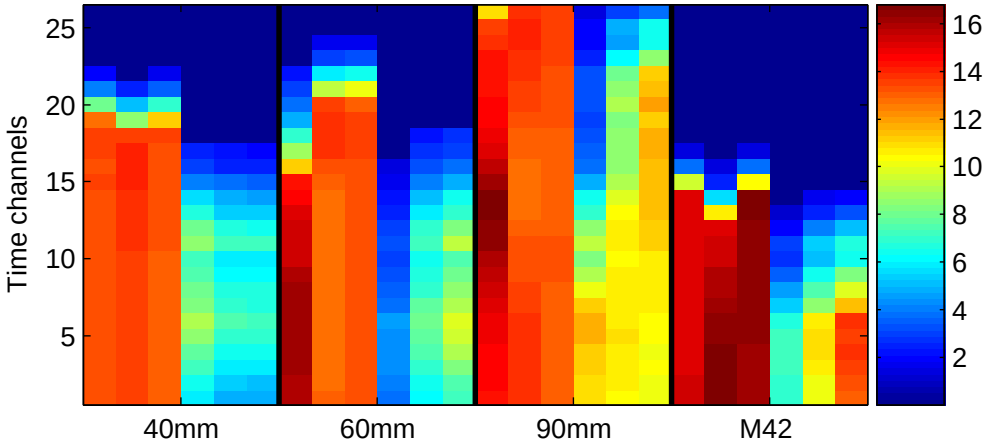

Figure 3.35: Square root of signal to noise ratio. For each item, the first three columns correspond to shallow positions, the next three to deeper positions, where SNR is lower. SNR=0 at later time channels if too few data for inversion (22% of cases), SNR$\geq$2 otherwise. Inversion was successful even for SNR as low as 2.

3.7 Application of the regularized NSMC

3.7.1 Time domain analysis of standard items

Fifteen standard ordnance were measured at the USACE-ERDC Vicksburg test stand using a Geonics EM-63 time domain sensor to test and develop the capabilities of current EMI forward models. These ordnance span a wide range of sizes, from 155 mm to 20 mm projectiles, and different material. Data were taken at two depths and three orientations, as in the previous section. Figure 3.36 shows total magnetic charge for all these items. To avoid saturating the figure only the median among all positions at each time channel is displayed. Not shown here, the distribution of total magnetic charge with time when depth and orientation has similar standard deviation as the four items presented in the previous section. This illustrates that the method of deriving the total magnetic charge is stable for all types of ordnance at hand.

Several observations can be made. The amplitude of total magnetic charge decays with time as the amplitude of the scattered field does. At early time, the magnitude of the total magnetic charge scales with the size of the ordnance. At later times, the charge signal reflects other properties of ordnance (shape, material). The latest time channels are not inverted for small items because the signal is too weak. The forward model provides adequate fit to data and high degrees of correlation between observations and predictions are achieved. All data were successfully inverted on the same size of spheroid, *a priori* information on the size of the object to model is therefore not required.

These results indicate that the time-evolving total magnetic charge acts as a unique signature for each type of ordnance. For instance the 37 mm, MK118 and BLU26, which have similar diameters but different material, length and density, have similar amplitudes at early time channels whereas their relative charge varies with several orders of magnitude beyond the 15th time channel. A preliminary attempt to quantify the degree of separation between each class of ordnance is presented in Figure 3.37 in a simple canonical analysis as in Beran (2005), using the first 18 time channels. In the left panel most of the variability recorded amongst all test stand data for the 15 ordnance can be summarized with two eigenvalues and feature vectors $xc1$ and $c2$. The resulting two-dimensional space $xc1 - xc2$ (right panel) of Figure 3.37 has total charges corresponding to different positions for each ordnance cluster and separate from those of other ordnance. The NSMC appears to be suitable for discrimination algorithms. Further work is warranted to extract the most relevant information out of the total charge distributions and to deal with complex situations, such as discrimination with incomplete time series of total charge.

As a further discrimination test, a series of cylinders were measured over the USACE-ERDC test stand in the same conditions as the standard ordnance to study their EMI response and test models. These six cylinders were chosen to be solid or hollow, short or long, made of steel or aluminum. Their total magnetic charge is presented in Figure 3.38, along with three large fragments of 105 mm HEAT rounds. Comparison with Figure 3.36 shows that the charge of these cylinders has a smaller time decay rate, which distinguishes the cylinders from their UXO counterparts. The fragments of 105 mm also produce distinct total charge.

3.7.2 Frequency domain analysis of standard items

Data were also collected with a Geophex GEM-3 sensor at the USACE-ERDC Vicksburg test stand to test the models' ability to perform with frequency-domain electromagnetic data. The sensor provides the real and imaginary part of the signal sampled at 10 frequencies from 90 to 41010 Hz. Data were processed and inverted by taking the modulus of data for every time channel so that amplitude reached maximum value directly above target, easing comparison with uniform charge distribution model so that the exact same regularized inversion procedure as for time domain could be applied. Information on phase was not used. Results are presented in Figure 3.39.

The regularized inversion of NSMC performs as well in the frequency domain as in the time domain. Predicted total magnetic charge is consistent for different positions and orientations of the item. The data misfit is

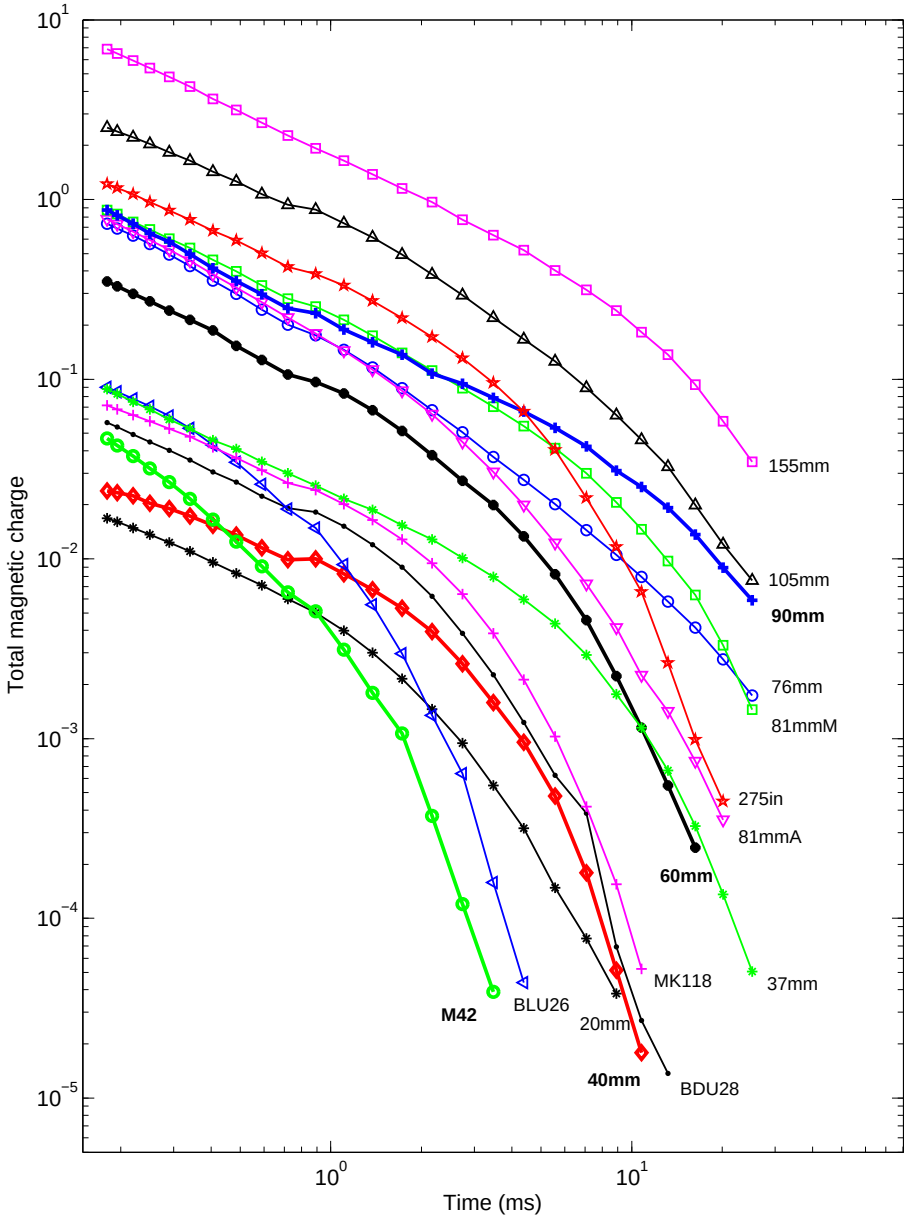

Figure 3.36: Total magnetic charge of 15 standard ordnance as a function of time. Data acquired over test stand with EM-63 sensor at 26 channels. Only median is shown for clarity, standard deviations similar to those of Figure 3.32. Note: there are 2 types of 81 mm items, the ATC and Montana.

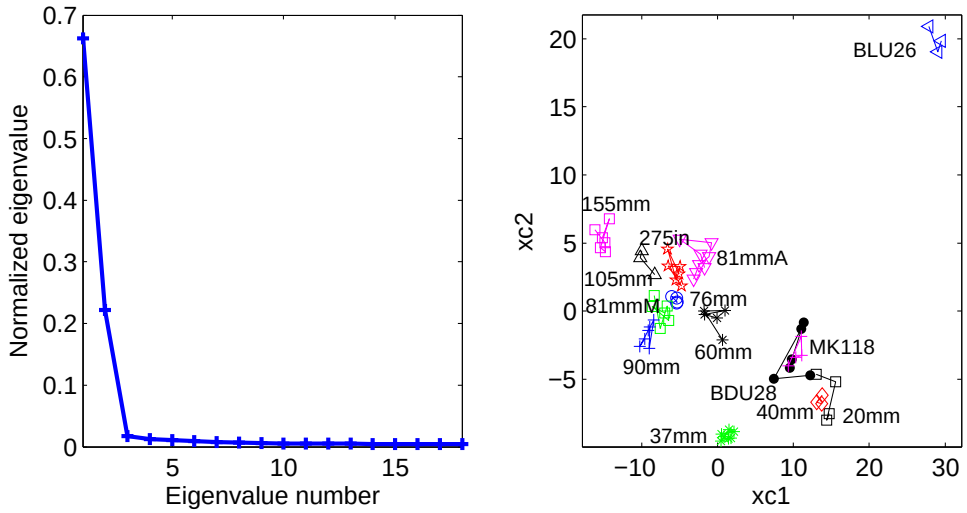

Figure 3.37: Canonical analysis of the 15 standard UXOs shown in Figure 3.36. Left panel: eigenvalues. Right panel: representation of features from total magnetic charges taken at different depths and orientations in plane of the two first eigenvectors.

close to expected noise and correlation coefficients are close to unity, but those details are not presented here. The method is therefore robust and the magnitude of the total charge scales with the size of objects. Canonical analysis presented in Figure 3.40 confirms stability of the total magnetic charge obtained by regularized inversion, and shows that each class of UXO has a distinct signature and belongs to a different part of feature space. These results show similar performance for regularized inversion of the surface charge model can indeed be expected for time domain and frequency domain electromagnetic induction-based identification of ordnance.

3.7.3 Application to field data

The following presents a series of preliminary tests to assess the type of difficulties the regularized inversion of NSMC would face when confronted with field realities.

Discrimination by total magnetic charge

Most of our development work on the regularized inversion of NSMC presented so far is based on test stand data, which offers a mostly noise-free environment. As a first step toward dealing with real site conditions, inversion was performed on data collected over a test plot at the Sky Research center in Ashland, Oregon, where a series of standard UXO were seeded. Data were acquired with an EM-63 sensor in cued interrogation mode, that is a stable platform with fix stations, as opposed to the regular dynamic acquisition mode of real survey. Data used here were taken 40 cm above the surface, slightly higher than the position of the sensor on its cart, which partially reduces the electromagnetic response of the magnetic soil. The following analysis includes a uniform background as additional parameter in the inversion to solve for the additional EM effect of soil.

Inversion results for three unknown targets, for which the position was estimated by other means, are presented in Figure 3.41. Thick lines show their total magnetic charge (derived from the field data), thin lines recall the total magnetic charge obtained from the test stand, as in Figure 3.32. Recovered total charges clearly overlap with their test stand counterparts; all three items are identified despite significant noise that corrupts late time channels. Results for the 40 mm and 60 mm ordnance are unambiguous for all time channels, whereas the M42 drifts toward a 40 mm-type response at later times. Work in progress is trying to address that issue.

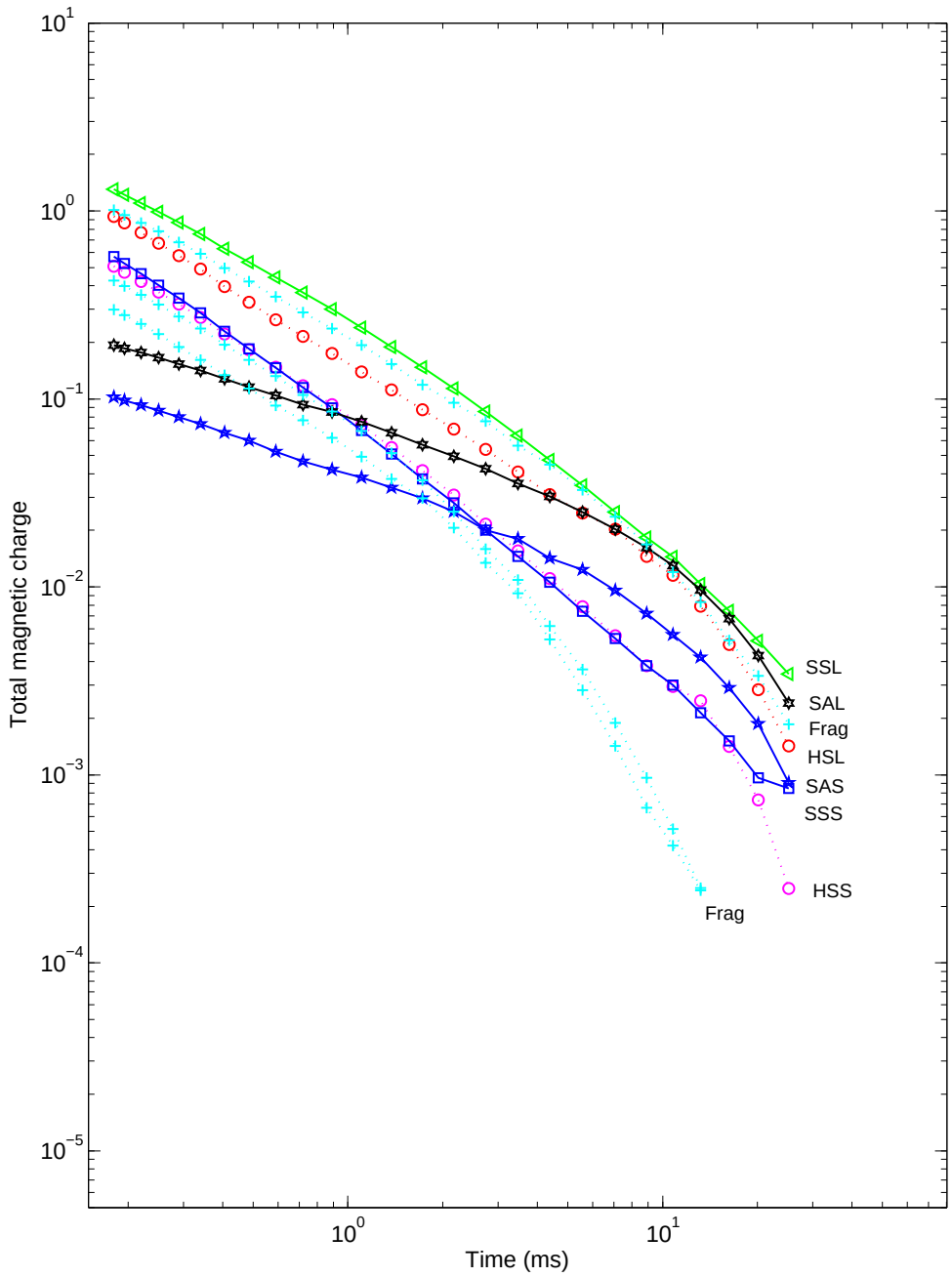

Figure 3.38: Total magnetic charge of six types of cylinders as a function of time using EM-63 data taken over a test stand. SSL: solid steel long, SSS: solid steel short, HSL: hollow steel long, HSS: hollow steel short, SAL: solid aluminum long, SAS: solid aluminum short.

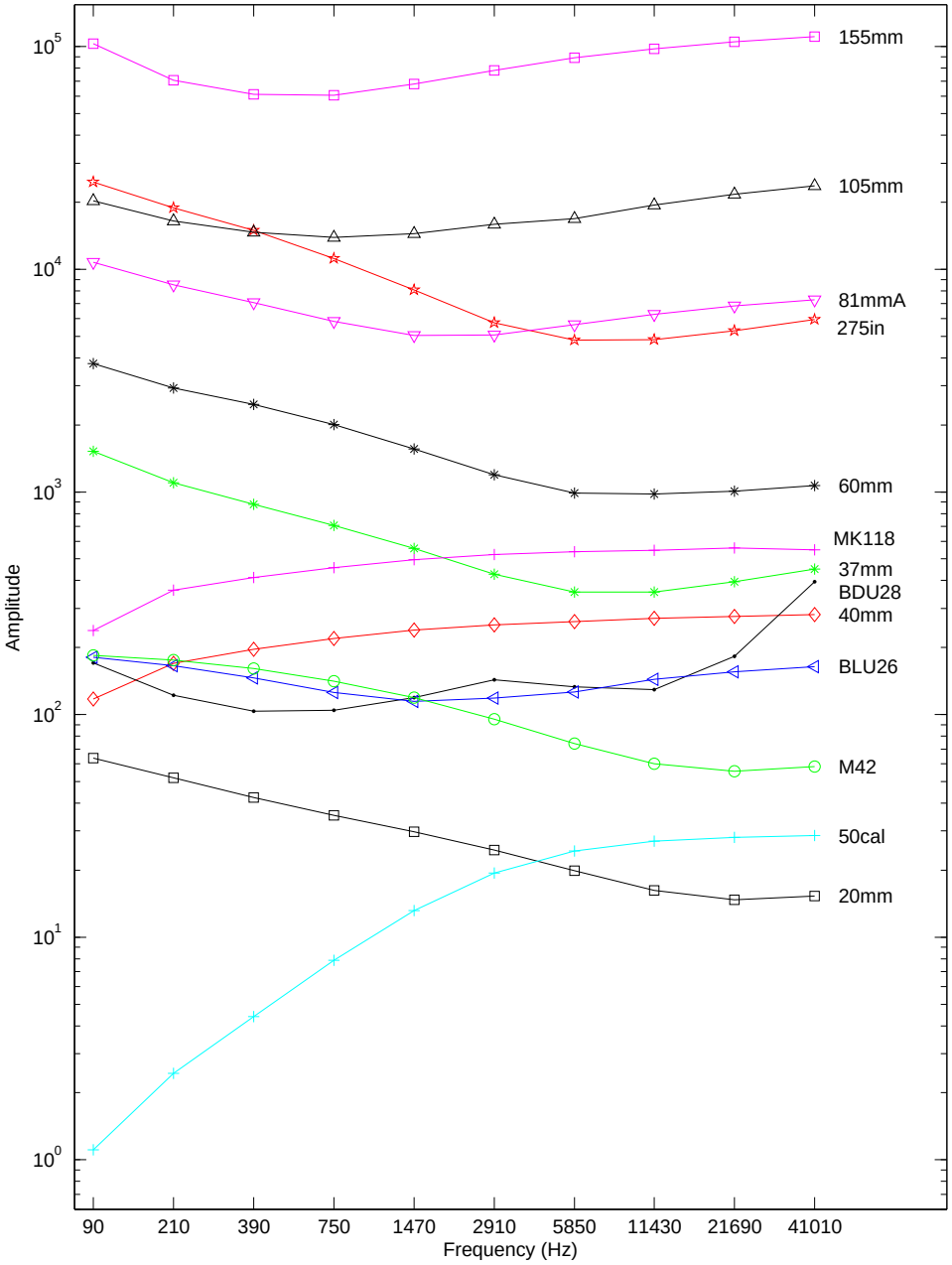

Figure 3.39: Total magnetic charge of 13 standard UXO items as a function of time, for data acquired with an GEM-3 sensor over Vicksburg test stand. Only median is shown for clarity, variance is illustrated in canonical analysis of Figure 3.40.

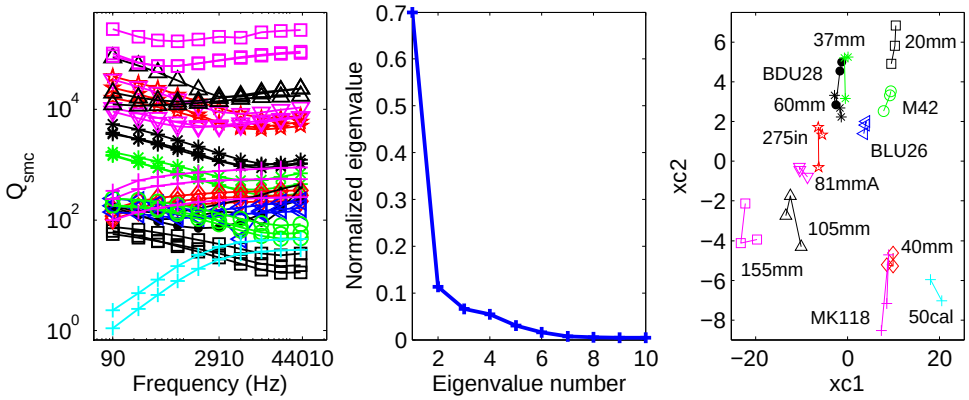

Figure 3.40: Canonical analysis on GEM-3 data for 13 classes of items. Left panel: total magnetic charge obtained for all positions measured on test stand. Central panel: eigenvalues. Right panel: representation of features from total magnetic charges taken at different depths and orientations in plane of the two first eigenvectors.

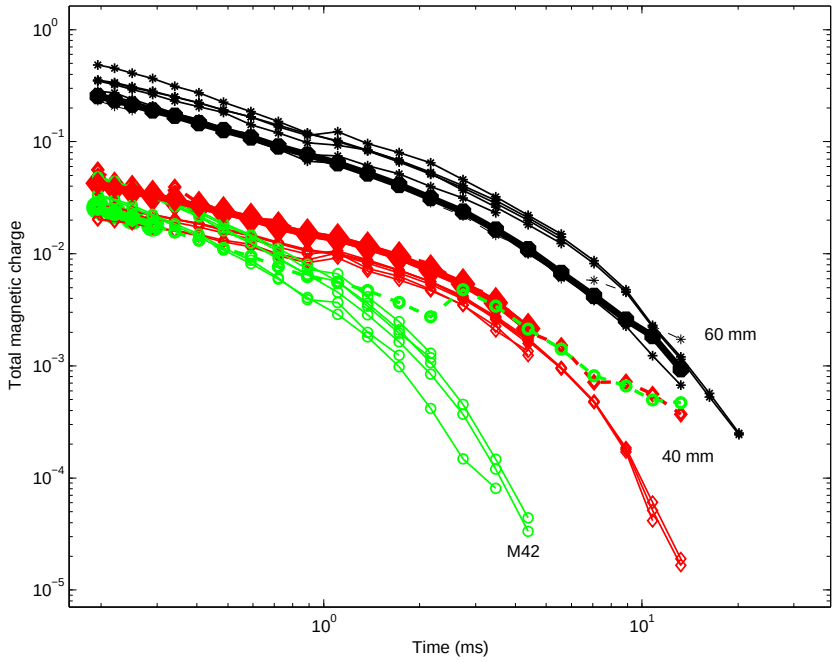

Figure 3.41: Field test of NSMC. Total magnetic charge for three buried items, shown in thick lines, overlaid on top of the total magnetic charge derived for the same ordnance on test stand.

As a side note, inversion of field data proved to be beneficial for the development of our inversion procedure because it forced a clear definition of the uniform distribution. When regularization was introduced (Section 3.6), the uniform charge distribution was taken as the median of the distribution of $H_i^{\mathrm{sc}}/\Sigma_j Z_{ij}$, the ratio of the measured scattered field and the sum of rows in the modeling matrix. The distribution and median change when noise and background value increase. The most robust mean of defining the uniform charge distribution is that of the upper end member of regularization. This definition of the uniform charge proves to be far more robust because the regularization process removes the effect of noise. Further examination of field data shall confirm the success of the method.

Effect of position on total magnetic charge

Defining the center of a target for EMI modeling is not straightforward because ordnance have complex shapes and include different material. In SMC modeling, ordnance are represented by a spheroid, the center of which does not necessarily coincide with that chosen for test stand measurements. This leads to positional uncertainties for inversion of test stand data. Addressing that issue and others regarding definitions of orientation, we conducted a simple sensitivity analysis and found that the total magnetic charge obtained by NSMC showed negligible sensitivity to horizontal positioning error within 15 cm and to any amount of error in azimuthal direction. The misfit, however, greatly increased when such errors occurred and therefore provided a good tool for estimating the correct parameters.

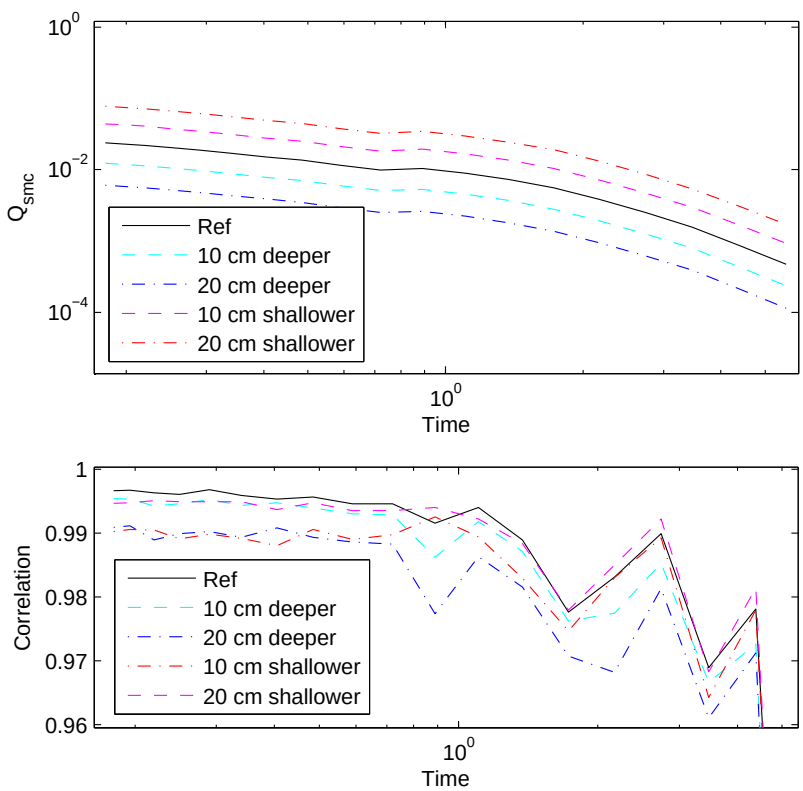

Figure 3.42: Effect of depth on the total magnetic charge. Upper panel: charge vs. time; lower panel: correlation between observation and prediction.

Depth is a more complex issue that requires particular attention. Figure 3.42 shows the effect of modeling the wrong depth on the total magnetic charge of a 40 mm UXO. The upper panel shows the charge, the lower panel the correlation between the data and forward model predictions. The total charge is found to vary in a predictable manner by a factor two for a 10 cm increment in vertical direction, expectedly increasing upward and

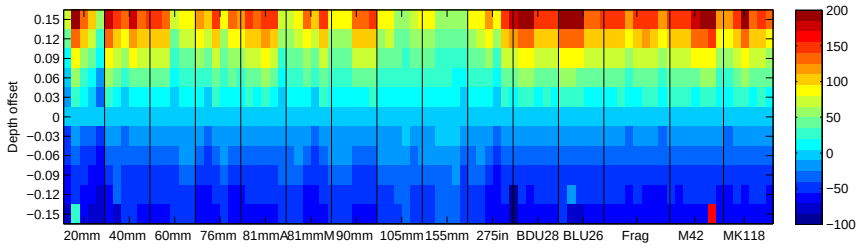

Figure 3.43: Percent change of the total magnetic charge when the model depth is offset from the true depth.

decreasing downward with respect to the correct location. Moreover, the charge presents exactly the same time decay at all modeled depths. Given the large separation between the total charge and the distinct decay rates of each UXO, this result suggests that 10–20 cm errors in depth would be no impediment for identifying the buried item. From there, recognizing the buried item can add a constraint on the inversion to recover the correct burial depth. The lower panel shows that the correlation coefficient, which reflects the data misfit, is only moderately but consistently affected by the depth error.

Figure 3.43 shows a first attempt to generalize that study. EM-63 test stand data are inverted adding an offset to the true depth (vertical axis), different settings of depth and orientation for each targets are indicated on the horizontal axis, only the first time channel is presented. The total charge varies by 50-100% within 10 cm of the true position, which confirms results for the 40 mm ordnance. Detailed examination through formal sensitivity analysis is warranted to reinforce that preliminary result. Confirmation of that effect would make the NSMC method a potent tool for UXO identification and discrimination.

3.8 Conclusion

In this chapter we conducted a detailed examination of the normalized surface magnetic charge model to apply it to electromagnetic data. With the goal of using the total magnetic charge, the integral of surface magnetic charges, as a criterion to identify and discriminate buried ordnance against clutter, we particularly focused on the stability of TMC for multiple orientations, depths, times and sensor types. Because the inverse problem is ill-posed, direct inversion is unstable and requires regularization. We looked for a physical basis to carry on that regularization and investigated the properties of the normalized surface charge distribution at the surface of a spheroid enclosing an ordnance. We found that the distribution varied under different directions and positions of excitation. When data are collected in real life, targets are illuminated under several directions, therefore some sort of averaging of the charge distribution occurs. This theoretical consideration, coupled with extensive empirical analysis of synthetic and test stand data taken at multiple depths and angles, leads to the conclusion that the most stable feature of the surface charge distribution and its total charge is the uniform charge distribution obtained by averaging. This result forms the basis of a regularization procedure that identifies a forward model that simultaneously (1) produces a high correlation coefficient between observation and prediction, (2) balances the misfit (not fitting noise) and the complexity of the charge distribution, and (3) produces a total magnetic charge close to that of a uniform charge distribution.

The method was tested on data collected with the Geonics EM-63 and Geophex GEM-3 sensors over 15 standard ordnance, 6 types of cylinders and clutter at multiple depths and orientations with the help of USACE at the ERDC test stand in Vicksburg, MS. We proved that the total magnetic charge derived from this regularized inversion protocol was a robust and stable feature for each type of target with both time-domain and frequency-domain types of data. We also found that the amplitude and time decay of TMC differs for each class of ordnance and cylinders and reflects the size and electromagnetic properties of their material. A simple canonical analysis confirmed the clear separation between the TMC features of all ordnance.

Preliminary tests were also done to assess the robustness of the method with noisy field data and the sen-

sitivity of target positioning error. Inversion of field data taken at the Sky Research test plot was successful at identifying buried items despite the high noise generated by the magnetic soil. Sensitivity analysis when the target position and orientation were altered showed that large errors in horizontal position and azimuthal direction do not affect determination of TMC. In contrast, the amplitude of TMC scales with depth error while time decay remains unaffected, thus allowing possible identification of the target despite depth error. Further work to systematically investigate these effects and others is warranted and detailed in the following Conclusion chapter.

Chapter 4

Discussion and Conclusions

4.1 Objectives

Initially, the objective of this research project was to apply the Method of Auxiliary Sources as a modeling tool for inversion of UXO sensor data. Through comparisons between measured data, analytical solutions, and data predicted by MAS, we found that MAS was able to accurately model the EMI response of compact metallic objects such as UXO over a large frequency range extending to the static case (Beran, 2005, Chapter 2). The ability to model over such a wide range made the MAS an attractive modeling technique for joint inversion of multiple data sets. Practical considerations such as the computational time required by MAS to calculate sensor data prevented us from applying MAS for inversion purposes. However, its quality as a physical model lead us to revise the objective of this study to evaluate the potential of two modeling techniques derived from the MAS framework: the Standardized Excitation Approach and the Surface Magnetic Charge model. We tested the methods for their performance as forward modeling technique, assessed as their ability to predict the data, provide stable feature vectors that are unique to the target and be fast in the perspective of field application. Although both SEA and SMC are based on magnetic charge distributions, they represent two fundamentally different approaches to UXO discrimination. We envision the SEA as part of a library or hypothesis testing technique, whereas SMC would be used in a parameter estimation/statistical classification scheme.

4.2 The Standardized Excitation Approach

In the SEA, the fundamental step is to build up an RSS that represent target attributes (size, shape, and EM parameters). We employ the MAS to generate the RSS for a candidate UXO whose geometry and physical quantities are the inputs for the process. The geometrical parameters are obtained by either digitizing or approximating equivalent cylindrical sections for a composite object. The conductivity and magnetic permeability of each section are estimated using measured data. The MAS code is then used to determine the source distribution for different spheroidal modes. There is significant computational effort required to generate the RSS and therefore it cannot be used in a parameter estimation sense, i.e., it is not reasonable to invert sensor data for an RSS (which would subsequently be part of a feature vector to be input to a classification algorithm). However, once the RSS is generated, the computational times are relatively quick. The SEA/RSS approach lends itself to a library or hypothesis testing technique for discrimination. Discrimination is thus achieved by determining which target within the library has the greatest likelihood in producing the anomaly.

For this study we developed an RSS library for 9 UXO. Testing was completed to determine the number of spheroidal modes sufficient for modeling transmitter fields generated by loop sensors. The ability to model both

frequency and time domain data was confirmed by comparing modeling results to Geophex GEM3 and Geonics EM63 data collected on a test stand. A simple library based discrimination technique was tested on GEM3 test stand data. An inversion algorithm for determining optimal location and orientation for a given UXO is in development.

Some SEA issues were identified during our investigation:

- **Improving the method of estimating conductivity and permeability for a composite UXO**

  When developing the RSS, the conductivity and permeability were calculated from a single sounding of GEM3 data collected over a horizontal target. A trial and error procedure was used to determine permeability and conductivity. Data collected on a line along the length of the target were used for evaluating the suitability of the permeability and conductivity estimates. Firstly, the material properties for an heterogeneous target should not be determined from only a single sounding when additional spatial data is available, or could be collected. Secondly, this process should be reformulated as an inverse problem to determine the material properties in an optimal way.

- **Further testing is required to determine the optimal number of charge rings**

  We chose 12 rings for the RSS based on limited measurements. Now that we have access to data acquired on the USACE-ERDC test stand, we can determine the number of rings required by the method.

- **Optimizing code for reducing forward modeling times**

  The non-optimized, research code used in this report required close to 7 seconds to model a RSS for a single sounding of 13 frequencies. These computations were carried out on a Pentium 4 3.2 GHz processor. Preliminary code improvements have reduced the time to just under three seconds. Further inefficiencies in the code are yet to be fixed. Eventually, The real high-speed SEA computation might be implemented via parallelization.

- **Developing algorithms for inverting location and orientation**

  The method tested in this report determined location and orientation by simply trying numerous depths and orientations. Although code was developed for inverting location and orientation for a given RSS, it was not mature enough by the end of the study to evaluate its accuracy and feasibility for real data.

4.3 The Surface Magnetic Charge Model

The SMC approach is used to predict the EMI response of a metallic object by assuming that the scattered field measured by sensors at the surface originates from a magnetic charge distribution on a fictitious spheroid that encloses the target. Once the surface is determined, the modeled data is a linear function of the charge distribution on the surface. The forward modeling is very fast and, therefore, sensor data can be inverted for the charge distribution. The sum of the charge distribution, i.e., the total surface magnetic charge, can be used for discrimination. Difficulties arise, however, because determining the surface magnetic charge distribution is an ill-posed, under-determined problem. The SMC inversion problem requires significant regularization in order to produce stable results for the total surface magnetic charge. Great effort was invested in the reported study to gain better understanding of the magnetic charge distribution and accordingly device a stable regularization procedure.

Some SMC specific issues were identified during our investigation:

- **The Normalized Magnetic Charge distribution is dependent on the angle of excitation**

  We showed that the normalized charge distribution changes as the angle of the primary field changes. Consequently, the total normalized magnetic charge, suggested by Shubitidze et al. (2005a) as a discriminant, will also vary. In order for the total normalized magnetic charge to be a more stable discriminant, data

should be taken such that there are numerous excitation angles. Data collected in this manner would produce a total normalized magnetic charge that represents an ”averaging” of the normalized charges over all excitation directions. This type of data could be collected by a single transmitter loop in low noise conditions collecting multiple soundings (such as a test stand), or by ”steering” the transmit field by using combinations of transmitter loops, or by changing the orientation of a single loop.

- **Regularized inversion for a stable Total Magnetic charge is possible with high quality data**

  We proposed a regularization method for SMC inversion such that the TMC is stable for high quality data collected over a test stand, and for measurements taken at mid-height above a magnetic soil. As mentioned above, the SMC method is data dependent. Therefore, simulations such as Monte Carlo and inversion of lesser-quality field data would be useful for covering a wider range of conditions and determining the data fidelity required for this method to succeed.

- **Time decay of Total Magnetic Charge is ordnance specific**

  Every type of ordnance and cylinder that we have tested so far shows a different signature. This is confirmed by preliminary canonical analysis and suggests the high potential for discrimination of UXO through their TMC. In-depth review of available statistical classification methods and development of procedures to deal with incomplete recovery of the TMC curve are warranted.

- **Sensitivity to location–orientation parameters**

  Preliminary tests suggest that the correct TMC can be inferred even when the modeling spheroid has an inaccurate horizontal position (≤ 10 cm) or with large errors in azimuthal direction. Depth error appears to affect the TMC in a predictable and consistent manner at all time channels, thus helping with the identification of buried ordnance despite modeling positional error. Detailed sensitivity analysis is warranted to systematically explore this effect and that of data positional error.

- **If target depth is known, a sphere or a plane can be used to determine the total magnetic charge**

  There is a tremendous amount of flexibility in the SMC model. As such, we have found that the shape of the magnetic charge surface does not need to conform closely to the target, i.e., multiple spheroids smaller or larger than the target can be used to model charges. Results not presented here also show that if we choose a sphere or a simple horizontal plane to model the charge distribution and determine the TMC, we can (1) still fit the data well, and (2) eliminate the need to determine the target orientation.

- **Inversion Algorithms for Location and orientation needs further development**

  In this study the location and orientation of the target was given, although simple algorithms were tested to optimize the horizontal position to correct for the discrepancy between the center of a ordnance as defined in the field and the center of the modeling spheroid that minimizes data misfit. A procedure to deal with the non-linear part of data inversion, i.e., identification of position and orientation, remains to be developed and tested. At this point it also remains unclear whether data are needed at two elevation to accurately determine all UXO parameters, as in Shubitidze et al. (2005), or whether full non-linear inversion of data at a single elevation would be possible.

4.4 Outlook

The work presented here has demonstrated that both the SEA/RSS and SMC approaches have potential to improve UXO discrimination. However, a substantial research and development effort must be undertaken before these techniques can be applied to the real world UXO problem. We presented some of the concerns specific to the performance and suitability of each method. Addressing these concerns, the next logical steps would include:

- **Comparison to Dipole Models**

  The dipole model is the most commonly used technique for UXO discrimination problems. In this study, we did not investigate if the SMC and SEA methods would represent a significant improvement to dipole

based methods. The SMC and SEA can model the non-dipolar components of the secondary field. This suggests that the spread of feature parameters for a SMC/SEA model would be relatively smaller than for dipole parameters. We would expect that for a library based discrimination approach the RSS would be more suitable than the dipole model due to the ability to more accurately model the data. The SMC model, however, is very flexible and, since a significant amount of regularization needs to be injected into the problem, the inversion for a charge distribution is much less straightforward than a dipole inversion. Now that a method for recovering the charge distribution has been established, comparisons to the dipole models discrimination ability can be carried out.

- **Sensitivity analysis**

  For both the SEA and SMC techniques it is critical to determine the data fidelity required for application to practical discrimination purposes. For the SEA, we need to determine a threshold for the misfit (or correlation) to the measured data below (or above) which we classify anomalies as not coming from targets within our library. For the SMC, analysis has to be completed that determines the quality of the total magnetic charge estimates as a function of signal to noise ratio as well as data coverage, positional error, and other survey/instrument characteristics.

- **Multiple Targets**

  The data considered in this study were from single, isolated targets. Provided that the response of two UXO targets are linear, the RSS can easily model the total response, and interpretation techniques based on the RSS can be developed. Nevertheless, the overlapping scenario of UXO plus clutter would be challenging to the SEA techniques. The ability for the SMC to be effective in a multiple target scenario is an open question.

- **Geologic background**

  A geologic background signal prevented us from processing data collected at the Sky Research UXO Test Site. Since the data were collected in a cued interrogation style (i.e., a small 2 m x 2 m area), we need to incorporate a soil background signal into our analysis.

We believe that if the above research can be carried out, then the full potential of the SEA and SMC techniques can be realized in UXO discrimination surveys.

Bibliography

Anderson, W. L.: 1982, Fast hankel transforms using related and lagged convolutions, *ACM Trans. Math. Softw.* **8**(4), 344–368.

Andreasen, M. A.: 1965, Scattering from bodies of revolution, *IEEE Transactions on Antennas and Propagation* **13**(2), 303–310.

Ao, C. O., Braunisch, H., O'Neill, K. and Kong, J.: 2002, Quasi-magnetostatic solution for a conducting and permeable spheroid object to arbitrary excitation, *IEEE Transactions Geoscience & Remote Sensing* **40**, 887–897.

Arfken, G. B.: 1995, *Mathematical Methods for Physicists*, fourth edn, Academic Press, San Diego, CA.

Barrows, B. E., O'Neill, K., Grzegorczyk, T., Chen, X. and Kong, J. A.: 2004, Broadband analytical magneto-quasi-static electromagnetic induction solution for a conducting and permeable spheroid, *IEEE Transactions on Geoscience and Remote Sensing* **42**(11), 2479–2489.

Beran, L.: 2005, *Classification of unexploded ordnance*, Master's thesis, University of British Columbia.

Braunisch, H., Ao, C., O'Neil, K. and Kong, J.: 2001, Magneto-quasistatic response of conducting and permeable prolate spheroid under axial excitation, *IEEE Transactions on Geoscience and Remote Sensing* **39**, 1352–1361.

Carin, L., Yu, H., Dalichaouch, Y., Perry, A. R., Czipott, P. V. and Baum, C. E.: 2001, On the wideband emi response of a rotationally symmetric permeable and conducting target, *IEEE Transactions on Geoscience and Remote Sensing* **39**(6), 1206–1213.

Chen, X., O'Neill, K., Barrowes, B., Grzegorczyk, T. and Kong, J.: 2004, Application of a spheroidal mode approach with differential evolution in inversion of magneto-quasistatic data for uxo discrimination, *Inverse Problems* **20**(6), 27–40.

Farquharson, C. G. and Oldenburg, D. W.: 2004, A comparison of automatic techniques for estimating the regularization parameter in nonlinear inverse problems, *Geophysical Journal International* **156**, 411–425.

Gao, P., Collins, L., Garber, P., Geng, N. and Carin, L.: 2000, Classification of landmine-like metal targets using wideband electromagnetic induction, *IEEE Transactions Geoscience and Remote Sensing* **38**(3), 1352–1361.

Geng, N., Baum, K. and Carin, L.: 1999, On the low frequency natural responses of conducting and permeable target, *IEEE Transactions Geoscience and Remote Sensing* **37**, 347–359.

Hansen, P. C.: 1997, *Rank-deficient and discrete ill-posed problems: numerical aspects of linear inversion*, SIAM, Philadelphia.

Kaufman, A. A. and Keller, G. V.: 1985, *Inductive Mining Prospecting*, Elsevier.

Menke, W.: 1989, *Geophysical Data Analysis: Discrete Inverse Theory, Revised Edition*, Academic Press, Inc., New York.

Miller, J., Bell, T., Soukup, J. and Keiswetter, D.: 2001, Simple phenomenological models for wideband frequency-domain electromagnetic induction, *IEEE Transactions Geoscience and Remote Sensing* **39**(6), 1294–1298.

Newman, G. A., Hohmann, G. W. and Anderson, W. L.: 1986, Transient electromagnetic response of a three-dimensional body in a layered earth, *Geophysics* **51**(8), 1608–1627.

Parker, R. L.: 1994, *Geophysical Inverse Theory*, Princeton Univ. Press.

Pasion, L. R., Billings, S. D., Oldenburg, D. W. and Walker, S. E.: 2006, Applicaition of library based method to time domain electromagnetic data for the identification of unexploded ordnance, *Journal of Applied Geophysics* . Accepted for publication.

Pasion, L. R. and Oldenburg, D. W.: 2001, A discrimination algorithm for uxo using time domain electromagnetics, *Journal of Engineering and Environmental Geophysics* **6**(2), 91–102.

Riggs, L., Mooney, J. and Lawrence, D.: 2001, Identification of metallic mine-like objects using low frequency magnetic fields, *IEEE Transactions on Geoscience and Remote Sensing* **39**(1).

Scales, J. A. and Tenorio, L.: 2001, Prior information and uncertainty in inverse problems, *Geophysics* **66**(2), 389–397.

Sebak, A., Shafai, L. and Das, Y.: 1991, Near-zone fields scattered by three-dimensinal highly conducting permeable objects in the field of an arbitrary loop, *IEEE Transactions Geoscience and Remote Sensing* **29**, 9–15.

Shubitidze, F., ONeill, K., Haider, S. A., Sun, K. and Paulsen, K. D.: 2002, Application of the method of auxiliary sources for electromagnetic induction problem, *IEEE Trans. Geoscience & Remote Sensing* **40**(4), 928–942.

Shubitidze, F., O'Neill, K., Shamatava, I., Sun, K. and Paulsen, K.: 2003, Analysis of emi scattering to support uxo discrimination: Heterogeneous and multi objects, *SPIE Conference on Detection and Remediation Technologies for Mines and Minelike Targets*, The International Society for Optical Engineering, pp. 928–939.

Shubitidze, F., O'Neill, K., Shamatava, I., Sun, K. and Paulsen, K.: 2004, Use of standardized source sets for enhanced emi classification of buried heterogeneous objects, *SPIE Conference on Detection and Remediation Technologies for Mines and Minelike Targets*, The International Society for Optical Engineering, pp. 263–274.

Shubitidze, F., ONeill, K., Shamatava, I., Sun, K. and Paulsen, K.: 2005a, A simple magnetic charge model for classification of multiple buried metallic objects in cases with overlapping signals, *Proceedings from SAGEEP 03*.

Shubitidze, F., ONeill, K., Shamatava, I., Sun, K. and Paulsen, K. D.: 2005b, Fast and accurate calculation of physically complete emi response by a heterogeneous metallic object, *IEEE Trans. Geoscience & Remote Sensing* **43**(8), 1736–1750.

Shubitidze, F., O'Neill, K., Sun, K. and Paulsen, K.: 2004, Investigation of broadband electromagnetic induction scattering by highly conducting, permeable, arbitrarily shaped 3-d objects, *IEEE Transactions Geoscience and Remote Sensing* **42**(3), 928–942.

Shubitidze, F., O'Neill, K., Sun, K. and Shamatava, I.: 2004, Coupling between highly conducting and permeable metallic objects in the emi frequency range, *Applied Computational Electromagnetic Society Journal, Special issue on ACES 2003 conference*, Vol. 19, pp. 139–148.

Shubitidze, F., O'Neill, K., Sun, K., Shamatava, I. and Paulsen, K.: 2004, A hybrid full MAS and combined MAS/TSA algorithm for electromagnetic induction problems sensing, *Applied Computational Electromagnetic Society Journal, Special issue on ACES 2003 conference*, Vol. 19, pp. 112–127.

Sun, K., O'Neill, K., Shubitidze, F., Haider, S. A. and Paulsen., K. D.: 2002, Simulation of electromagnetic induction scattering from targets with negligible to moderate penetration by primary fields, *IEEE transactions on geoscience and remote sensing* **40**, 910–927.

Sun, K., O'Neill, K., Shubitidze, F., Shamatava, I. and Paulsen., K. D.: 2004, Theoretical analyses of TSA formulation and its domain of validity, *IEEE transactions on geoscience and remote sensing* **42**(9), 1871–1881.

Sun, K., O'Neill, K., Shubitidze, F., Shamatava, I. and Paulsen., K. D.: 2005, Fast data-derived fundamental spheroidal excitation models with application to uxo identification, *IEEE transactions on geoscience and remote sensing* **43**(11), 2573–2583.

Tarantola, A.: 1987, *Inverse Problem Theory: Methods for Data Fitting and Model Parameter Estimation*, Elsevier.

Zhang, Y., Collins, L., Yu, H., Baum, C. E. and Carin, L.: 2003, Sensing of unexploded ordnance with magnetometer and induction data: Theory and signal processing, *IEEE Transactions on Geoscience and Remote Sensing* **41**(5), 1005–1015.